Pontifícia Universidade Católica do Rio de Janeiro

Leonardo Carvalho Mesquita

Probabilistic method for uncertainties consideration in geomechanical problems based on Green's function approach and first-order second-moment method

Tese de Doutorado

Thesis presented to the Programa de Pós-graduação em Engenharia Civil of PUC-Rio in partial fulfillment of the requirements for the degree of Doutor em Ciências - Engenharia Civil

Advisor: Prof. Elisa Dominguez Sotelino

Rio de Janeiro
March 2023

Pontifícia Universidade Católica do Rio de Janeiro

Leonardo Carvalho Mesquita

Probabilistic method for uncertainties consideration in geomechanical problems based on Green's function approach and first-order second-moment method

Thesis presented to the Programa de Pós-graduação em Engenharia Civil of PUC-Rio in partial fulfillment of the requirements for the degree of Doutor em Ciências - Engenharia Civil. Approved by the Examination Committee.

Prof. Elisa Dominguez Sotelino
Advisor
Department of Civil and Environmental Engineering – PUC-Rio

Prof. Ney Augusto Dumont
Department of Civil and Environmental Engineering – PUC-Rio

Prof. Raquel Quadros Velloso
Department of Civil and Environmental Engineering – PUC-Rio

Prof. Kátia Vanessa Bicalho
UFES

Prof. Leonardo José do Nascimento Guimarães
UFPE

Rio de Janeiro, March 10, 2023.

Leonardo Carvalho Mesquita

Electromechanical technical degree at CEFET-MG in 2008. Undergrad in Civil Engineering at Federal University of Viçosa (UFV) in 2013. M.Sc. Degree in Civil Engineering also at Federal University of Viçosa (UFV) in 2016. Adjunct professor of the Civil Engineering course at Federal University of Viçosa campus Rio Paranaiba (UFV-CRP) since 2015.

Bibliographic data

Mesquita, Leonardo Carvalho

Probabilistic method for uncertainties consideration in geomechanical problems based on Green's function approach and first-order second-moment method / Leonardo Carvalho Mesquita; advisor: Elisa Dominguez Sotelino. – 2023.
169 f.: il. color.; 30 cm

Tese (doutorado) – Pontifícia Universidade Católica do Rio de Janeiro, Departamento de Engenharia Civil e Ambiental, 2023.
Inclui bibliografia

1. Engenharia Civil e Ambiental - Teses. 2. Consideração de incertezas. 3. Método das funções de Green. 4. Problemas geomecânicos. 5. Método FOSM. 6. Teorema da reciprocidade. I. Sotelino, Elisa Dominguez. II. Pontifícia Universidade Católica do Rio de Janeiro. Departamento de Engenharia Civil e Ambiental. III. Título.

CDD: 624

I dedicate this thesis to all education professionals who over the past 30 years have contributed to my academic development.

Acknowledgments

During the last four years several people and institutions contributed directly or indirectly to the development of this work, I would like to record my thanks here.

Initially, I would like to thank Professor Dr. Elisa Sotelino for accepting to supervise my doctoral work, for all the advice during this period, and for the opportunity to discover a new area through the project “Modelagem Geomecânica do Pré-sal”. I will carry her example of professionalism and dedication until the last day of my academic career.

I would like to thank my family for all the emotional support and moments of relaxation during this period, especially during the months of lockdown generated by the COVID-19 pandemic.

I would like to thank my wife Amanda Guimarães for being my confidant during the happy and frustrating moments provided by the doctoral period.

I would like to thank my doctoral colleague Matheus Peres for all the precious moments of discussion and teachings of computational mechanics, Green's functions approach, artificial intelligence, and so many other subjects.

I would like to thank Dr. Yves Leroy from TotalEnergies for discussions on the method of Green's functions, which is the basis of the developments proposed in this work.

I would like to thank my postgraduate colleague Thiago Ayres for the fun times in the city of Rio de Janeiro.

I would like to thank the Federal University of Viçosa (UFV) for the period of full leave to carry out this doctorate.

I would like to thank all the professors and staff at the Pontifical Catholic University of Rio de Janeiro (PUC-Rio) for contributing to my academic development.

I would like to thank TotalEnergies for funding part of this study through the “Modelagem Geomecânica do Pré-sal” project.

I would like to thank Petrobras engineers Diogo Rossi, Vitor Mello, and Ricardo Amaral for the discussions on practical issues associated with geomechanical modeling of reservoirs.

I would like to thank the teachers Daniel Linhares and Melanie Tavares for the English classes, which allowed me to write this thesis document.

I would like to thank Prof. Dr. Flávio Silva (PUC-Rio) and Prof. Dr. Viktor Mechtcherine (TU Dresden) for the opportunity to carry out a sandwich internship at Technische Universität Dresden (Germany).

I would like to thank professors Dr. Ney Augusto Dumont, Dr. Raquel Quadros Velloso, Dr. Kátia Vanessa Bicalho and Dr. Leonardo José do Nascimento Guimarães for agreeing to read and evaluate this work.

Finally, I would like to thank God for the opportunity to develop this work.

This study was financed in part by the Coordenação de Aperfeiçoamento de Pessoal de Nível Superior - Brasil (CAPES) - Finance Code 001.

Abstract

Mesquita, Leonardo Carvalho; Sotelino, Elisa Dominguez (Advisor). **Probabilistic method for uncertainties consideration in geomechanical problems based on Green's function approach and first-order second-moment method**. Rio de Janeiro, 2023. 169 p. Doctoral thesis - Department do Civil and Environmental Engineering, Pontifical Catholic University of Rio de Janeiro.

The present work proposes a computationally efficient stochastic statistical method (called Green-FOSM) that considers uncertainties in geomechanical problems, with the objective of improving the decision-making process related to problems associated with the process of fluid injection or depletion. The novelty of the method lies in the use of the Green's function approach (GFA), which, together with the first-order second-moment statistical method (FOSM), is used to propagate uncertainties associated with the mechanical properties of material to the displacement field of the geological formation. Furthermore, using the concepts of stochastic grid and autocorrelation function, the proposed method allows the consideration of the spatial variability of random variables that represent these mechanical properties. The GFA uses the fundamental solutions of classical mechanics (Kelvin fundamental solution, Melan fundamental solution, among others) and the reciprocity theorem to calculate the displacement field of a geological formation with irregular geometry, and different types of materials. The great advantage of this method compared to the classical finite element method (FEM) is that it does not require the imposition of boundary conditions and the analysis of the problem can be performed considering only the reservoir or other regions of interest. This modeling strategy decreases the degrees of freedom of the model and the CPU time of the deterministic analysis. In this way, as the GFA requires less computational effort, this approach becomes ideal for propagating the uncertainties in geomechanical problems. Initially, an iterative version of the Green-FOSM method was proposed, which presents statistical results similar to those found through the classic Monte Carlo simulation (MCS). In this initial version, the displacement field is calculated using an iterative numerical scheme, which decreases the computational performance of the method and can generate convergence problems. Such limitations would restrict the application of the original GFA and the iterative Green-FOSM method in real problems. Thus, the present work also developed a new version of the GFA, which uses a non-iterative numerical scheme. For the proposed validation problems, the non-iterative method proved to be up to 17.5 times faster than the original version. This version is able to expand the applicability of the GFA, since the convergence problems were eliminated and the results obtained by this method, when analyzing a representative geological profile of the Brazilian pre-salt, are similar to those found via FEM. Finally, based on the non-iterative GFA, a non-iterative version of the Green-FOSM method was proposed. This non-iterative version is capable of probabilistically analyzing complex geological formations, such as the Brazilian pre-salt geological formations. Using the same computational resources, the non-iterative Green-FOSM method is at least 200 times faster than the iterative Green-FOSM method. In general, the results found in the investigated analyzes (deterministic and probabilistic) are close to the results obtained by the reference method (FEM and MCS, respectively).

Keywords

Uncertainties consideration; Green's function approach; First-order second-moment (FOSM); Geomechanical problems; Probabilistic method; Reciprocity theorem.

Resumo

Mesquita, Leonardo Carvalho; Sotelino, Elisa Dominguez (Orientador). **Método probabilístico para consideração de incertezas baseado no método das funções de Green e no método estatístico first-order second-moment**. Rio de Janeiro, 2023. 169 p. Tese de Doutorado – Departamento de Engenharia Civil e Ambiental, Pontifícia Universidade Católica do Rio de Janeiro.

O presente trabalho propõe um método estatístico computacionalmente eficiente (chamado Green-FOSM) para consideração de incertezas em problemas geomecânicos, com o objetivo de melhorar o processo de tomada de decisão ao analisar problemas associados com o processo de injeção ou depleção de fluídos. A novidade do método proposto está associada com a utilização do método das funções de Green (GFA), que, com o auxílio do método estatístico first-order second-moment (FOSM), é utilizado para propagar as inerentes incertezas associadas às propriedades mecânicas do material para o campo de deslocamento da formação geológica. Além disso, através dos conceitos de grid estocástico e função de autocorrelação, o método proposto permite a consideração da variabilidade espacial de variáveis aleatórias de entrada que representam essas propriedades mecânicas. O GFA utiliza as soluções fundamentais da mecânica clássica (solução fundamental de Kelvin, solução fundamental de Melan, entre outras) e o teorema da reciprocidade para determinar o campo de deslocamento de uma formação geológica com geometria irregular e diferentes tipos de materiais. A grande vantagem deste método em relação ao clássico método dos elementos finitos (MEF) é que ele não requer a imposição de condições de contorno e a análise do problema pode ser realizada considerando apenas o domínio do reservatório ou outras regiões de interesse. Esta estratégia de modelagem diminui os graus de liberdade do modelo e o tempo de processamento da análise. Desta forma, como o GFA requer menos esforço computacional, este método torna-se ideal para ser utilizado na propagação de incertezas em problemas geomecânicos. Inicialmente, baseado no método das funções de Green original proposto por Peres et al. (2021), foi proposto uma versão iterativa do método Green-FOSM, que apresenta resultados estatísticos semelhantes aos encontrados através da clássica simulação de Monte Carlo (SMC). Nesta versão original, o campo de deslocamento é

calculado usando um esquema numérico iterativo que diminui o desempenho computacional do método e pode gerar problemas de convergência. Tais limitações tem dificultado a aplicação do GFA original e do método Green-FOSM iterativo em problemas reais. Assim, o presente trabalho desenvolveu uma nova versão do GFA que utiliza um esquema numérico não-iterativo. Para os problemas de validação analisados, o método não-iterativo demonstra ser até 17.5 vezes mais rápido do que a versão original. Além disso, esta versão demonstra ser capaz de expandir a aplicabilidade do GFA, pois os problemas de convergência foram eliminados e os resultados obtidos por este método, ao analisar um perfil geológico representativo do pré-sal brasileiro, são semelhantes aos encontrados via MEF. Por fim, a partir do GFA não-iterativo foi proposta uma versão não-iterativa do método Green-FOSM. Esta versão não-iterativa é capaz de analisar probabilisticamente formações geológicas complexas, como é o caso das formações geológicas do pré-sal brasileiro. Utilizando os mesmos recursos computacionais, o método Green-FOSM não-iterativo é no mínimo 200 vezes mais rápido que o método iterativo. De forma geral, os resultados encontrados nas análises realizadas (determinísticas e probabilísticas) são próximos dos resultados obtidos pelo método de referência (MEF e SMC, respectivamente).

Palavras-chave

Consideração de incertezas; Método das funções de Green; First-order second-moment (FOSM); Problemas geomecânicos; Método probabilístico; Teorema da reciprocidade.

Summary

List of figures

List of tables

List of abbreviations and symbols

p.d.f.	probability density function
p.m.f.	probability mass function
c.d.f.	cumulative distribution function
MCS	Monte Carlo simulation
LHS	Latin hypercube sampling
FOSM	first-order second-moment method
GFA	Green's function approach
FEM	finite element method
SNX	autocorrelation function of type single exponential
SQX	autocorrelation function of type squared exponential
SMK	autocorrelation function of type second-order Markov
CSX	autocorrelation function of type cosine exponential
BIN	autocorrelation function of type binary noise
CV	coefficient of variation
flop	floating point operations

$\tilde{X}$	random variable
S	sample space
$f_{\tilde{X}}$	probability functions of the random variable $\tilde{X}$
$F_{\tilde{X}}$	cumulative distribution function of the random variable $\tilde{X}$
$P[\tilde{X} \leq x]$	probability of occurrence of the random variable $\tilde{X}$
g	function that correlates the random variables $\tilde{X}$ and $\tilde{Y}$
h	inverse function of g
T	region in $\boldsymbol{Y}$ space
J	Jacobian of the transformation
$\mathrm{E}[\tilde{Y}^n]$	nth statistical moment of the random variable $\tilde{Y}$
$\mathrm{E}[\tilde{Y}]$	mean value of the random variable $\tilde{Y}$ (first statistical moment)
$\mathrm{Var}[\tilde{Y}]$	variance of the random variable $\tilde{Y}$ (second statistical moment)
$\boldsymbol{\mu}$	vector of mean values
$\mathrm{Cov}[\tilde{X}_i, \tilde{X}_j]$	covariance between the random variables $\tilde{X}_i$ and $\tilde{X}_j$
$\sigma_{\tilde{X}_i}$	standard deviation of the random variable $\tilde{X}_i$
$\mu_{\tilde{X}_n}$	mean value of the random variable $\tilde{X}_n$
$\sigma^2_{\tilde{X}_n}$	variance of the random variable $\tilde{X}_n$
θ	fluctuation scale
$\rho_{\tilde{X}_i\tilde{X}_j}$	autocorrelation function
τ	relative distance between points t' and t^*
Ω_R	reservoir subdomain
Ω_t	problem domain

$\Delta\sigma_{ij}$	variation of the stress state
Δp	change in pore pressure
f_i	external field generated by body or surface forces
ε_{ij}	second-order strain tensor
u_i	displacement vector
$\mathbb{C}^{e}_{ijkl}$	fourth-order stiffness tensor
A_{ij}	second-order Biot tensor
$\Delta\bar{\sigma}_{ij}$	additional second-order stress tensor
$\hat{u}_i$	virtual displacement vector
$\hat{\varepsilon}_{ij}$	virtual strain tensor
ΔT_i	variation of surfaces forces
$u_k(X_i)$	horizontal or vertical displacement in the position X_i
α	Biot coefficient
δ_{ij}	Kronecker delta
ε^{*}_{mnk}	strains in the x_i position obtained from the fundamental solution
N_{Ω_R}	number of triangular regions in Ω_R subdomain
N_{Ω_t}	number of triangular regions in Ω_t domain
n	step of the iterative Green's function approach (Chapter 4) or number of nodes in the mesh of triangular elements (Chapter 5 and Chapter 6)
δu_k	error parameter used in iterative Green's function approach
$\mathbb{D}$	vector of the partial derivatives of the displacements
$\mathbb{C}$	matrix with the spatial variability of the input random variables
$[\Delta\sigma]$	variation of the stress state
$[\varepsilon]$	second-order strain tensor
$\mathbb{C}^{\mathrm{e}}$	fourth-order stiffness tensor
$[A]$	second-order Biot tensor
Δp_{f}	pore-pressure variation
$[\Delta\sigma_c(\underline{x})]$	Complementary stress tensor
$\mathbb{C}(\underline{x})$	fourth-order constitutive tensor
$\{\hat{u}\}$	virtual displacement vector
$[\hat{\varepsilon}]$	virtual strain tensor
$\{\Delta T\}$	vector with the variation of surface forces
$\{f\}$	body forces vector
$[\mathbb{I}]$	identity tensor
$\{u(\underline{X})\}$	displacement vector at position $\underline{X}$
$\{e_\beta\}$	direction vector of the unit point load
Θ_β	volumetric strain variation
$\{\varepsilon_\beta(\underline{x},\underline{X})\}$	strain vector at position $\underline{x}$ obtained from the auxiliary problem
$\{\varepsilon(\underline{x})\}$	strain vector calculated at position $\underline{x}$ of the real problem
$[\mathcal{B}^j(\underline{x})]$	matrix of the derivatives of the shape functions

$\{E_\Theta\}$	energy generated by the volumetric strain
$\{E_c\}$	complementary elastic energy
$\{U\}$	global vector of nodal displacements
R	internal radius (reservoir)
K_R	reservoir bulk modulus (core)
G_R	reservoir shear modulus (core)
C	external radius (cap rock)
K_C	cap rock bulk modulus
G_C	cap rock shear modulus
K_∞	bulk modulus of the infinite space
G_∞	shear modulus of the infinite space
E	Young's modulus
ν	Poisson's ratio
V_{LC}	volume of the layered cylinder
$\tilde{\alpha}$	random variable representing the Biot coefficient
$\tilde{E}_{\text{inf}}$	random variable representing the Young's modulus of the infinite medium
$\tilde{\nu}_{\text{inf}}$	random variable representing the Poisson's ratio of the infinite medium
$\tilde{E}$	random variable representing the Young's modulus
$\tilde{\nu}$	random variable representing the Poisson's ratio
$\{\tilde{U}\}$	random variables representing global vector of nodal displacements
$\left\{\mathbb{D}_\kappa^{(n)}\right\}$	vector of dimension that contain the partial derivatives
$\mathbb{S}$	matrix that considers the spatial variability of input random variables
l_h	horizontal correlation lengths
l_v	vertical correlation lengths

"As far as the laws of mathematics refer to reality, they are not certain, and as far as they are certain, they do not refer to reality."

Albert Einstein

1 Introduction

The oil industry is one of the most important worldwide industries, since oil and natural gas are the main commodities traded in the international market (BAFFES; NAGLE, 2022). In Brazil, in recent decades, oil production has been boosted by the discovery of pre-salt reservoirs. According to Petrobras[1], the average daily production of oil in the pre-salt layer increased from 41 thousand barrels in 2010 to 2.0 million barrels in 2020. Data from the bp Statistical Review of World Energy 2022[2] reveal that Brazil produced around 3.0 million barrels of oil and natural gas in 2022, being that more than 2/3 of Brazilian production comes from pre-salt reservoirs. Oil extraction in pre-salt reservoirs, whose depth varies between 5 and 7 km, is a complex task that contains several uncertain factors. The present work seeks to consider the influence of some of these factors on the geomechanical response of a geological formation subjected to the process of fluid injection or depletion.

1.1. Motivation

The physical phenomena associated with the process of fluid injection or depletion present different degrees of complexity and uncertainties. Historically, most engineering problems have been analyzed using deterministic approaches. Such approaches can generate low precision results, which do not represent all possible answers to the problem (APOSTOLOPOULOU et al., 2019; PEREIRA et al., 2014a; PEREIRA, 2015; WANG et al., 2016).

In its natural state, rocks are among the most variable engineering materials (FENTON; GRIFFITHS, 2008). As shown in Figure 1.1, this natural variability is

[1] https://petrobras.com.br/pt/nossas-atividades/areas-de-atuacao/exploracao-e-producao-de-petroleo-e-gas/pre-sal/

[2] https://www.bp.com/content/dam/bp/business-sites/en/global/corporate/pdfs/energy-economics/statistical-review/bp-stats-review-2022-full-report.pdf

illustrated by the ranges of variation of mechanical properties (Young's modulus, Figure 1.1.a, and Poisson's coefficient, Figure 1.1.b) of different rock types.

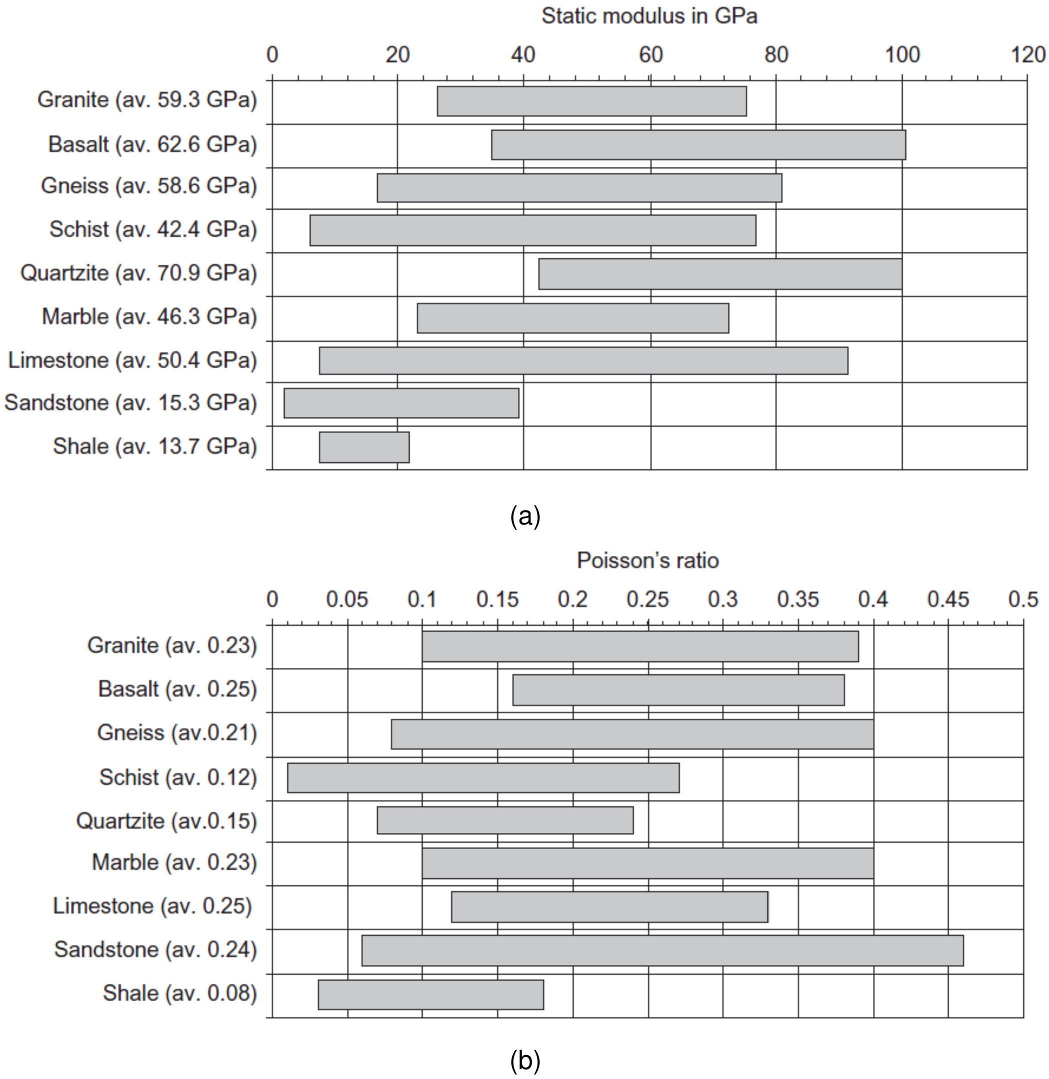

Figure 1.1. Range of variation of the mechanical properties of rock (in (a) static Young's modulus and in (b) Poisson's ratio) (JOHNSON; DEGRAFF, 1988).

These and other uncertainties can be incorporated into the geomechanical response using a probabilistic approach. For this, the input parameters and the results obtained through the geomechanical analysis are admitted as random variables (LI; SARMA; ZHANG, 2011). In this way, the process of interpreting the results is not carried out based on the evaluation of a deterministic point result, but on the statistical parameters (mean value, variance, probability density function and others) of the random variable that represents the answer to the geomechanical problem.

The present work aims to incorporate the uncertainties associated with the spatial variability of the mechanical properties of rocks (Young's modulus, Poisson's ratio, and Biot coefficient) to the geomechanical results generated by the fluid injection and/or extraction process. Through these results, it is possible to probabilistically analyze different types of phenomena associated with pore pressure variation, for example, swelling or compaction of the reservoir rock, the subsidence of the free surface, and fault reactivation. From an environmental point of view, these results can help reservoir engineers in the decision-making process in terms of CO_2 storage in underground formations.

In this process, the uncertainties associated with the input random variables (mechanical properties of materials) are propagated to the random variables that represent the answer to the problem (displacement, strain, and stress fields) using exact or approximate statistical methods. Exact methods use the concept of functions of random variables, in which the probability density functions (p.d.f.) of the output random variables are analytically calculated using a function $\tilde{Y}_i = \mathrm{g}(\tilde{X}_i)$ and the p.d.f. of the input $(\tilde{X}_i)$ random variables (FENTON; GRIFFITHS, 2008). For complex $\mathrm{g}(\tilde{X}_i)$ functions, such as the functions that govern geomechanical problems, the use of exact methods becomes unfeasible. In these situations, the propagation of uncertainties can be performed through approximate statistical methods such as the Monte Carlo simulation (MCS), Latin hypercube sampling (LHS), and the first-order second-moment (FOSM) method.

Due to its simplicity and ease of implementation, the MCS has been the most used statistical method in problems related to the propagation of uncertainties (LIU, 2004). However, this method requires a huge number of realizations (repetitions) which, in general, requires a large computational effort. This makes it unfeasible for the treatment of complex problems, as is the case of the problems treated in this work. In this scenario, the FOSM method appears as an appropriate statistical method, since it is computationally efficient and applicable to the variability range of the input random variables.

Given this context, the present work proposes a new method for considering uncertainties in geomechanical problems, which aims to improve the decision-making process regarding the problems associated with the processes of recovery and storage of fluids (water, oil, natural gas, or CO_2) in underground reservoirs. The novelty of the proposed method lies in the use of Green's function approach (GFA), which uses the fundamental solutions of classical mechanics (Kelvin, Melan, Mindlin, or others) to propagate the uncertainties related to the mechanical properties of materials to the displacement, strain, and stress fields of the geological formation.

1.2. Objectives

The main objective of this research is to develop a mathematical method for considering the uncertainties associated with the mechanical properties of materials (rocks) in geomechanical problems submitted to the process of fluid injection and/or depletion in underground reservoirs.

The specific objectives are: (1) to extend the deterministic and iterative GFA, originally proposed by Peres et al. (2021) [3], to the statistical case in order to consider the uncertainties associated with the heterogeneity and variability of the mechanical properties of the rocks in the geomechanical response of the problem; (2) to eliminate the iterative calculation process from the original deterministic GFA in order to improve its computational performance and, at the same time, eliminate the convergence problems observed in the original version; (3) to extend the non-iterative GFA formulation to the statistical case; and (4) study the effect of the spatial variability of the mechanical properties of rocks on the displacement, strain and stress fields of a geological section based on the Brazilian pre-salt layer.

1.3. Organization

The organizational structure of this thesis follows the manuscript format, in which the standard thesis chapters are replaced by manuscripts that have been either published or submitted for publication in peer-reviewed international journals. To orient the reader, Chapter 2 provides a literature review on the consideration of uncertainties in geotechnical and geomechanical problems. Chapter 3 presents the fundamental statistical concepts related to the theoretical developments shown in the other chapters of the document. Chapter 4 is the manuscript titled "Uncertainties consideration in elastically heterogeneous fluid-saturated media using first-order second moment stochastic method and Green's function approach" that was

[3] Original Green's function approach proposed by Matheus L. Peres, Leonardo C. Mesquita, Yves M. Leroy and Elisa D. Sotelino within the scope of the project "Modelagem Geomecânica do Pré-Sal" developed by PUC-Rio in partnership with TotalEnergies.

published in Applied Mathematical Modeling Journal. This chapter deals with the extension of the original GFA (deterministic and iterative) to the statistical approach. Chapter 5 consists of the manuscript entitled “Non-iterative Green’s function approach for unbounded heterogeneous fluid-saturated media” which was submitted to the International Journal for Numerical and Analytical Methods in Geomechanics. This chapter proposes a new formulation to the original GFA, which expands the applicability of the deterministic method and simultaneously eliminates the original iterative calculation process, which greatly improved the computational performance. Chapter 6 presents the manuscript “Evaluation of the spatial variability of the mechanical properties of rocks in heterogeneous fluid-saturated media using non-iterative Green's function approach and first-order second moment stochastic method” which was submitted to Applied Mathematical Modeling Journal. In this chapter, the non-iterative GFA is extended statistically and the effect of spatial variability of the mechanical properties of rocks that make up a geological formation of the Brazilian pre-salt is analyzed. Lastly, Chapter 7 summarizes the findings of this research and discusses directions for future work. An extensive list of references is provided after Chapter 7. The computational methods developed within the scope of this work were implemented using the Python language.

2
State-of-art-review of uncertainties in geomechanics

Consideration of uncertainties associated with a given process is an essential part of any engineering project. An analysis that aims to provide data about the behavior of a given problem must be able to offer an assessment of the uncertainties associated with these data. Without this assessment, the actions taken based on this data are questionable (PEREIRA, 2015).

Nowadays, works related to the quantification of uncertainties can be found in several areas of knowledge, such as medical sciences (KOMPA; SNOEK; BEAM, 2021; SHAN et al., 2020), environmental sciences (BESSAR; ANCTIL; MATTE, 2021; MIRDAR HARIJANI; MANSOUR, 2022), economics (MEGLIN; KYTZIA; HABERT, 2022), urban planning (PANDEY; DONGRE; GUPTA, 2020; TEBYANIAN et al., 2022), applied mathematics (WANG et al., 2021), and nuclear engineering (FEDON et al., 2021). Most of these works are based on concepts of classical probability theory (LOÈVE, 1977). However, in the literature there are other methodologies for the quantification of uncertainties, for example, the theory of imprecise probabilities (ASLETT; COOLEN, 2020), the theory of possibility (DUBOIS; PRADE, 1998a, 1998b; GEORGESCU, 2012), and the theory of evidence (KOHLAS; MONNEY, 1994; SHAFER, 1976). The statistical developments presented in the next sections are based on classical probability theory.

2.1.
Uncertainties consideration in geotechnical applications

Soils and rocks in their natural state are among the most variable of all engineering materials (FENTON; GRIFFITHS, 2008). A thorough literature review on the subject revealed that, over the last few decades, several studies that deal with the consideration of uncertainties in geotechnical applications have been developed. Table 2.1 summarizes some of the most prominent research on the consideration of uncertainties in geomechanical applications found in the literature.

Table 2.1. Scientific studies on the consideration of uncertainties in geomechanical problems

Author(s)	*Application(s)*
Brzakala and Pula (1996)	consider the randomness related to the location of the interface between the layers, the properties of materials, and the acting load in the calculation of the settlement of shallow foundations
Griffiths and Fenton (1997)	deal with the steady seepage through a three-dimensional soil domain in which the permeability is randomly distributed in space
Cai (2011)	presents a study that quantifies uncertainties associated with the in-situ stress field, rock mass strength parameters, and deformation modulus in tunnel and cavern design
Bungenstab and Bicalho (2016)	perform probabilistic evaluation to assess the variability of footing settlements on sandy soil
Yu et al. (2020)	propose a mathematical method to consider the uncertainties related to soil parameters in pile designs for landslide stabilization
Ahamed et al. (2021)	consider uncertainties associated with geotechnical properties in the design of bridge foundations
Franke and Olson (2021)	incorporates uncertainties in predicting soil liquefaction risk
Pang et al. (2021)	considers uncertainties associated with soil properties in dynamic slop analysis
Blondeel et al. (2022)	analyze cohesion as a random field in the calculation of slope stability
Mazraehli et al. (2022)	introduce uncertainties in the analysis of underground excavations
Zarrin et al. (2022)	consider the uncertainties associated with the mechanical properties of the soil in the modeling of jacket offshore platforms

As can be seen, in these works the main geomechanical problems (foundation settlement, seepage, stress and deformation in soils and rocks, slope stability, and soil liquefaction risk) are analyzed probabilistically assuming some degree of uncertainty. These works demonstrate that a probabilistic approach must be employed when analyzing a geotechnical problem. Bungenstab and Bicalho (2016) affirm that geotechnical analysis based on conventional deterministic approaches, using safety factors, is highly dependent on available mathematical models and information obtained in the field, which most often do not accurately describe the characteristics of materials. According to Cai (2011), the variability of soil and rock properties is intrinsic and subjective and has a considerable influence on decision-making in geotechnical problems. In this study, the influence of variability is highlighted when analyzing the radial displacements of a tunnel, which, due to uncertainties, can be up to 65% greater or less than the value found using a deterministic approach. Even greater variation is found by Mazraehli et al. (2022) when analyzing the stress field of an underground excavation, which can assume values up to 80% higher than the values obtained deterministically. Pang et al. (2021) say that traditional analysis methods, with a single factor of safety, cannot consider the variations of the various facts involved in geotechnical problems and, therefore, methods based on statistical concepts can provide a solid basis for the decision-making. According to Yu et al. (2020), the mechanical properties of the in-situ soil are highly variable, which makes it difficult to determine a single set of optimal parameters to be used in deterministic analyses. As a result, statistical methods that consider the uncertainties associated with these problems have been widely used.

In addition to the aforementioned studies, there are several geotechnical applications in the literature that deal with the spatial variability of the mechanical properties of materials. The scientific studies in Table 2.2 are used as a reference for the construction of the stochastic random field that defines the spatial variability of the mechanical properties of rocks adopted in Chapters 4 and 6. This table presents a brief description of these studies and the main conclusions found by the authors.

Table 2.2. Scientific studies on the spatial variability of the mechanical properties of materials in geotechnical applications

Author(s)	***Description(s) and main conclusion(s)***
Srivastava and Babu (2009)	consider the effect of the spatial variability of the mechanical properties of the soil in the bearing capacity analysis of a shallow foundation resting on a clayey soil and in the analysis of stability and deformation pattern of a cohesive-frictional soil slope; the results obtained demonstrate that the spatial variability of the mechanical properties of the soil considerably influences the performance of the evaluated geotechnical applications

Table 2.2. Scientific studies on the spatial variability of the mechanical properties of materials in geotechnical applications (continuation)

Author(s)	***Description(s) and main conclusion(s)***
Suchomel and Masín (2010)	consider the spatial variability of cohesion and friction angle in slope stability analyses using three statistical methods (classic FOSM; modified FOSM; and probabilistic reference method based on FEM); the spatial variability of the mechanical properties under analysis are introduced using a modified FOSM method; the results demonstrate that the probability of failure is satisfactorily calculated by the modified FOSM when the standard deviation of the input random variables decreases or when their correlation lengths increase; these authors conclude that the modified FOSM method may provide a good estimate of the probability of slope failure
Cho (2012)	performs a probabilistic analysis of seepage through an embankment on soil foundation to study the effects of uncertainty due to spatial heterogeneity of hydraulic conductivity on the seepage flow; the spatial variability of the hydraulic conductivity is considered through a Gaussian random field described by an exponential autocorrelation function (this function is presented in Section 3.2.1 of this document); the results demonstrated that the correlation distances of the autocorrelation function have a significant influence on the seepage flow
Li et al. (2015)	propose a multiple-response surface method for slope reliability analysis considering spatially varying soil properties; differences between results obtained using five theoretical 2-D autocorrelation functions are systematically compared (these functions are presented in Section 3.2.1); these results demonstrate that the SQX (squared exponential) and SMK (second-order Markov) type autocorrelation functions can characterize the spatial correlation of soil properties more realistically
Wang et al. (2020)	propose an effective method for identification of representative slip surfaces of slopes with spatially varied soils within the framework of limit equilibrium method, which utilizes an adaptive K-means clustering approach; the spatial variability of soil mechanical properties is incorporated into the problem using an exponential autocorrelation function; the results obtained by the proposed method are compatible with the results obtained via Monte Carlo Simulation

In general, all the works presented in this section exemplify the importance of considering the different types of uncertainties in the analysis of geotechnical problems. Furthermore, due to the heterogeneity and inherent spatial variability of rock formations found in geomechanical problems, it is understood that these types of problems must take into account the different sources of uncertainties, as is done in geotechnical applications.

2.2. Uncertainties consideration in geomechanical applications

As demonstrated in the previous item, several studies have been done on the consideration of uncertainties in geotechnical applications over the last few decades. However, in the geomechanical field, especially in the area of reservoirs, the literature review revealed that this type of approach has been used scarcely. The few studies encountered are described next.

Muller et al. (2009a) and Muller et al. (2009b) consider the influence of the spatial variability of hydraulic and mechanical properties on the elastoplastic behavior of the rock mass when analyzing the stability of oil producing wells. In both works, statistical analyzes are performed using a finite element program developed by these authors. To analyze this same type of problem, Batalha et al. (2020) present a 2D stochastic geomechanical model based on the MCS, in which a spatially correlated random field is used to consider the variability of the Young's modulus of the rocks that make up the geological formation.

Pereira et al. (2014b) quantify the uncertainties associated with the reactivation of geological faults using the non-probabilistic method of evidence theory. Seithel et al. (2019) use MCS to consider geological uncertainties in fault reactivation problems in the Bavarian Molasse Basin (Germany). Rossi et al. (2020) present a study that quantifies uncertainties related to the effects of local fault surface orientation, pore pressure fluctuations, and friction coefficient variability in a fault reactivation problem in the Val d'Agri oil field (Italy). Using data obtained from the reactivation of geological faults, Zoccarato et al. (2019) propose a mathematical model to quantify and reduce the uncertainties associated with seismic event modeling, which are generated by the injection or extraction process of fluids in underground reservoirs. For this, these authors use the finite element method (FEM) together with the MCS and the Polynomial Chaos expansion method. Bourne et al. (2015) also use MCS to probabilistically analyze the seismic risk induced by the production of natural gas in a reservoir in the Groningen field (Netherlands).

In the specific area of reservoir engineering there are few applications. Pereira et al. (2016) use a non-probabilistic method based on the theory of evidence to introduce the uncertainties associated with the mechanical properties of rocks in subsidence and compaction problems. Bottazzi and Della Rossa (2017) use the MCS to quantify the uncertainties associated with the geomechanical analysis of underground reservoirs. Mahdi Rajabi et al. (2022) developed a study that aims to minimize the risks associated with geological uncertainties in CO_2 storage problems through an application that combines a multiphase numerical model, artificial neural networks and MCS.

All these works highlight the importance of considering uncertainties in different types of geomechanical problems. In the case of well problems, Muller et al. (2009a) and Muller et al. (2009b) emphasize that the results obtained deterministically can lead to evaluations that do not represent the real situation. These studies demonstrate that the variability of the mechanical parameters of the rocks has a great influence on the results obtained from three-dimensional analyzes of wells. In addition, they also affirm that the variability of response variables (stresses, strains, and displacements) increases as the variability of rock properties increases. The examples analyzed by Batalha et al. (2020) demonstrate that, due to the uncertainties associated with the Young's modulus, the mud pressure considered safe for drilling a well calculated deterministically can be up to twice as high as the pressure calculated statistically. Thus, this uncertainty has a great influence on the stability of wells. Pereira et al. (2014b) point out that a reliable geomechanical analysis (in this case, a fault reactivation analysis) must take into account the inherent uncertainties associated with the rocks that make up the geological formation. Using a hypothetical example, these authors demonstrate that the pore-pressure variation that causes fault reactivation, obtained through a probabilistic analysis, can be up to 27% smaller than the deterministic calculated variation.

As in the previous section, the works presented in this section demonstrate the need to incorporate the uncertainties associated with the process of fluid injection or depletion in the analysis of geomechanical problems. As can be seen, in most of the studies found in the literature, the MCS is used to propagate the uncertainties of interest. However, in general, this method is computationally expensive, which limits its application in complex geomechanical problems. Therefore, the present work seeks to propose a computationally efficient methodology that, at the same time, allows for the consideration of uncertainties associated with the mechanical properties of rocks.

3
Theoretical background

This chapter provides a review of the theoretical concepts related to the developments that are presented in the next chapters of this document.

3.1.
Function of random variables

As previously mentioned, the developments presented in the next chapters are formulated using the concepts of probability theory (LOÈVE, 1977). Applying these concepts, the mechanical properties of the rocks that form the geological profile and the responses (displacement, strain, and stress fields) obtained through geomechanical analysis can be treated as random variables.

Conceptually, random variables are used to represent a set of possible events. According to Fenton and Griffiths (2008), $\tilde{X}$ will be a random variable if it is defined by a function that assigns a real number $\tilde{X}(s)$ to each result $s \in S$, where S is the sample space formed by the set of results $\{s_1, s_2, \ldots\}$.

Random variables can be discrete or continuous. Discrete random variables are those that assume only discrete values $\{x_1, x_2, \ldots\}$ and they are described by a probability mass function (p.m.f.). Continuous random variables can assume an infinite number of possible outcomes (i.e., usually $\tilde{X}$ takes values from the real line $\mathbb{R}$) and they are defined by a probability density function (p.d.f.). In both cases, the probability functions of the random variable $\tilde{X}$ are mathematically represented by $f_{\tilde{X}}(x)$. An additional description of the random variable is done through the cumulative distribution function (c.d.f.), $F_{\tilde{X}}(x)$, defined by

$$F_{\tilde{X}}(x) = P[\tilde{X} \leq x] = \sum_{t \leq x} f_{\tilde{X}}(t) \tag{3.1}$$

or

$$F_{\tilde{X}}(x) = P[\tilde{X} \leq x] = \int_{-\infty}^{x} f_{\tilde{X}}(t)\, dt \,, \tag{3.2}$$

where $f_{\tilde{X}}(t)$ is a discrete or continuous random variable, respectively.

As cited by Fenton and Griffiths (2008), one of the main reasons for using random variables is the possibility of performing mathematical calculations that implicitly consider the set of possible events. As shown in the following section, the random variables resulting from these mathematical calculations can be obtained exactly or approximately.

3.1.1. Functions of a single variable

Problems containing a single random variable can be solved in an exactly using the following methodology. Consider that the random variable $\tilde{Y}$ (whose p.d.f. is unknown) can be calculated in terms of the random variable $\tilde{X}$ (whose p.d.f. is known) using the function

$$\tilde{Y} = \mathrm{g}(\tilde{X}). \tag{3.3}$$

When $\tilde{X}$ takes a specific value, that is, when $\tilde{X} = x$, we can compute $\tilde{Y} = y = \mathrm{g}(x)$.

If we assume that $\mathrm{g}(x)$ is defined by the one-to-one function illustrated in Figure 3.1, then the probability of $\tilde{Y} = y$ will be exactly equal to the probability of $\tilde{X} = x$. Since the two probabilities are equal, we can calculate the height of p.d.f. of $\tilde{Y}$ in the neighborhood of y_1. Analyzing the same situation in the neighborhood of x_2, it can be seen that the height of p.d.f. of $\tilde{Y}$ close to y_2 depends not only on the area A_2 (which is the probability that $\tilde{X}$ is in the neighborhood of x_2), but also on the slope of $\mathrm{g}(x)$ at point x_2. In this way, as the slope decreases, the height of $f_{\tilde{Y}}(y)$ increases.

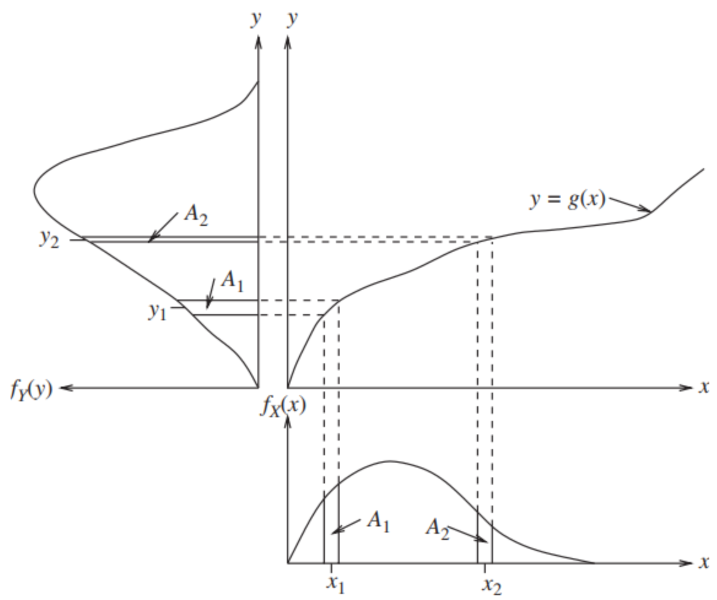

Figure 3.1. Relation between the Random variables $\tilde{X}$ and $\tilde{Y}$ (FENTON; GRIFFITHS, 2008).

Applying the concept of c.d.f. to two regions (such as the A_2 regions shown in Figure 3.1) that have the same probabilities of occurrences results in the following

$$F_{\tilde{Y}}(y) = F_{\tilde{X}}(x) = F_{\tilde{X}}\left(\mathrm{g}^{-1}(y)\right) = \int_{-\infty}^{x} f_{\tilde{X}}(x)\mathrm{d}x = \int_{-\infty}^{\mathrm{g}^{-1}(y)} f_{\tilde{X}}(x)\mathrm{d}x$$
$$= \int_{-\infty}^{y} f_{\tilde{X}}\left(\mathrm{g}^{-1}(y)\right)\left[\frac{\mathrm{d}}{\mathrm{d}y}\mathrm{g}^{-1}(y)\right]\mathrm{d}y\,, \tag{3.4}$$

where $x = \mathrm{g}^{-1}(y)$. The p.d.f. can be calculated by differentiating the c.d.f. with respect to y, which results in

$$f_{\tilde{Y}}(y) = \frac{\mathrm{d}}{\mathrm{d}y}F_{\tilde{Y}}(y) = f_{\tilde{X}}\left(\mathrm{g}^{-1}(y)\right)\left|\frac{\mathrm{d}}{\mathrm{d}y}\mathrm{g}^{-1}(y)\right| = f_{\tilde{X}}(x)\left|\frac{\mathrm{d}x}{\mathrm{d}y}\right|. \tag{3.5}$$

Eq. (3.4) is obtained assuming that y always increases when x increases. However, if y decreases when x increases, the probability of $\tilde{Y} \leq y$ will be determined from the probability of $\tilde{X} > x$. To consider these two cases (and since the probability values are always positive), the absolute value of the term $\mathrm{d}[\mathrm{g}^{-1}(y)]/\mathrm{d}y$ is used in Eq. (3.5). Furthermore, this equation demonstrates that $f_{\tilde{Y}}(y)$ increases when the inverse of the slope ($|\mathrm{d}x/\mathrm{d}y|$) increases.

When $\mathrm{g}(x)$ is not a one-to-one function, the probabilities of all the $\tilde{X} = x$ values which lead to each y are added into the probability that $\tilde{Y} = y$. That is if the values $\mathrm{g}(x_1)$, $\mathrm{g}(x_2)$, ..., $\mathrm{g}(x_n)$ lead to the same value of y, the result is the following

$$f_{\tilde{Y}}(y) = f_{\tilde{X}}(x_1)\left|\frac{\mathrm{d}x_1}{\mathrm{d}y}\right| + f_{\tilde{X}}(x_2)\left|\frac{\mathrm{d}x_2}{\mathrm{d}y}\right| + \cdots + f_{\tilde{X}}(x_n)\left|\frac{\mathrm{d}x_n}{\mathrm{d}y}\right|. \tag{3.6}$$

The number of terms n usually depends on y, so this computation over all y can be quite difficult (FENTON; GRIFFITHS, 2008).

3.1.2. Functions of two or more random variables

The joint probability distribution of random variables $\tilde{Y}_1, \tilde{Y}_2, \dots, \tilde{Y}_n$ in terms of the joint distribution of $\tilde{X}_1, \tilde{X}_2, \dots, \tilde{X}_n$ can also be calculated exactly using the following methodology. Consider the functions

$$\left.\begin{array}{c}\tilde{Y}_1 = \mathrm{g}_1(\tilde{X}_1, \tilde{X}_2, \dots, \tilde{X}_n) \\ \tilde{Y}_2 = \mathrm{g}_2(\tilde{X}_1, \tilde{X}_2, \dots, \tilde{X}_n) \\ \vdots \\ \tilde{Y}_n = \mathrm{g}_n(\tilde{X}_1, \tilde{X}_2, \dots, \tilde{X}_n)\end{array}\right\} \Leftrightarrow \left\{\begin{array}{c}\tilde{X}_1 = \mathrm{h}_1(\tilde{Y}_1, \tilde{Y}_2, \dots, \tilde{Y}_n) \\ \tilde{X}_2 = \mathrm{h}_2(\tilde{Y}_1, \tilde{Y}_2, \dots, \tilde{Y}_n) \\ \vdots \\ \tilde{X}_n = \mathrm{h}_n(\tilde{Y}_1, \tilde{Y}_2, \dots, \tilde{Y}_n)\end{array}\right. , \tag{3.7}$$

where the h_n functions are obtained by inverting the (given) g_n functions.

As shown in Eq. (3.5), the distribution of $\tilde{Y}$ in terms of $\tilde{X}$ is obtained by the product of $f_{\tilde{X}}(x)$ and the derivative $\mathrm{d}[\mathrm{g}^{-1}(y)]/\mathrm{d}y$. This methodology can be generalized to the case of several random variables. In this case, the joint probability distribution of $\tilde{Y}_1, \tilde{Y}_2, \dots, \tilde{Y}_n$ is given by

$$f_{\tilde{Y}_1\tilde{Y}_2\dots\tilde{Y}_n}(y_1, y_2, \dots, y_n) = \begin{cases} f_{\tilde{X}_1\tilde{X}_2\dots\tilde{X}_n}(\mathrm{h}_1, \mathrm{h}_2, \dots, \mathrm{h}_n)|J| & \text{for } (y_1, y_2, \dots, y_n) \in T \\ 0 & \text{otherwise} \end{cases} , \tag{3.8}$$

where T is the region in $\boldsymbol{Y}$ space which corresponds to the possible values of x, specifically

$$T = \{\mathrm{g}_1, \mathrm{g}_2, \dots, \mathrm{g}_n : (x_1, x_2, \dots, x_n) \in S\} , \tag{3.9}$$

and J is the Jacobian of the transformation

$$J = \det \begin{bmatrix} \dfrac{\partial \mathrm{h}_1}{\partial y_1} & \dfrac{\partial \mathrm{h}_1}{\partial y_2} & \cdots & \dfrac{\partial \mathrm{h}_1}{\partial y_n} \\ \dfrac{\partial \mathrm{h}_2}{\partial y_1} & \dfrac{\partial \mathrm{h}_2}{\partial y_2} & & \dfrac{\partial \mathrm{h}_2}{\partial y_n} \\ \vdots & & \ddots & \vdots \\ \dfrac{\partial \mathrm{h}_n}{\partial y_1} & \dfrac{\partial \mathrm{h}_n}{\partial y_2} & \cdots & \dfrac{\partial \mathrm{h}_n}{\partial y_n} \end{bmatrix} . \tag{3.10}$$

3.1.3. Statistical moments of functions

In many cases, the complete probability distribution calculated from a function of random variables is difficult to be determined. In these situations, it may be interesting to approximately obtain at least the mean value and the variance of the output random variables resulting from these functions. According to Fenton and Griffiths (2008), calculating only these statistical parameters is usually easier than calculating the complete probability distribution. Furthermore, the central limit theorem can often be invoked to suggest that the final distribution is normal or lognormal.

3.1.3.1. Statistical parameters of functions of a single variable

If g is a function of random variables that allows calculating $\tilde{Y}$ in terms of $\tilde{X}$, the nth statistical moment of $\tilde{Y}$ will be given by

$$\mathrm{E}[\tilde{Y}^n] = \int_{-\infty}^{\infty} \mathrm{g}^n(x) f_{\tilde{X}}(x)\, dx\,. \tag{3.11}$$

Depending on how it is formulated, there are different levels of approximation for the calculation of these moments. To show this, consider the expansion of the function g in terms of Taylor's series centered on the mean value ($\mu_{\tilde{X}}$) of the random variable $\tilde{X}$

$$\tilde{Y} = \mathrm{g}(\tilde{X}) = \mathrm{g}(\mu_{\tilde{X}}) + (\tilde{X} - \mu_{\tilde{X}}) \left.\frac{d\mathrm{g}}{dx}\right|_{\mu_{\tilde{X}}} + \frac{1}{2}(\tilde{X} - \mu_{\tilde{X}})^2 \left.\frac{d^2\mathrm{g}}{dx^2}\right|_{\mu_{\tilde{X}}} + \cdots. \tag{3.12}$$

A first-order approximation is obtained by truncating Eq. (3.12) after the first two terms, which results in

$$\mathrm{E}[\tilde{Y}] \cong \mathrm{E}\left[\mathrm{g}(\mu_{\tilde{X}}) + (\tilde{X} - \mu_{\tilde{X}}) \left.\frac{d\mathrm{g}}{dx}\right|_{\mu_{\tilde{X}}}\right] = \mathrm{g}(\mu_{\tilde{X}}) \text{ and} \tag{3.13}$$

$$\mathrm{Var}[\tilde{Y}] \cong \mathrm{Var}\left[\mathrm{g}(\mu_{\tilde{X}}) + (\tilde{X} - \mu_{\tilde{X}}) \left.\frac{d\mathrm{g}}{dx}\right|_{\mu_{\tilde{X}}}\right] = \mathrm{Var}[\tilde{X}] \left(\left.\frac{d\mathrm{g}}{dx}\right|_{\mu_{\tilde{X}}}\right)^2, \tag{3.14}$$

where $\mathrm{E}[\tilde{Y}]$ and $\mathrm{Var}[\tilde{Y}]$ represent the mean value (first moment) and the variance (second moment) of the random variable $\tilde{Y}$, respectively. The second-order approximation uses the first three terms of Taylor's series expansion

$$\mathrm{E}[\tilde{Y}] \cong \mathrm{g}(\mu_{\tilde{X}}) + \frac{1}{2}\mathrm{Var}[\tilde{X}] \left(\left.\frac{d^2\mathrm{g}}{dx^2}\right|_{\mu_{\tilde{X}}}\right) \text{ and} \tag{3.15}$$

$$\begin{aligned} \mathrm{Var}[\tilde{Y}] \cong\ & \mathrm{Var}[\tilde{X}] \left(\left.\frac{d\mathrm{g}}{dx}\right|_{\mu_{\tilde{X}}}\right)^2 - \left(\frac{1}{2}\mathrm{Var}[\tilde{X}] \left.\frac{d^2\mathrm{g}}{dx^2}\right|_{\mu_{\tilde{X}}}\right)^2 \\ & + \mathrm{E}\left[(\tilde{X} - \mu_{\tilde{X}})^3\right] \left(\left.\frac{d\mathrm{g}}{dx}\frac{d^2\mathrm{g}}{dx^2}\right|_{\mu_{\tilde{X}}}\right) \\ & + \frac{1}{4}\mathrm{E}\left[(\tilde{X} - \mu_{\tilde{X}})^4\right] \left(\left.\frac{d^2\mathrm{g}}{dx^2}\right|_{\mu_{\tilde{X}}}\right)^2. \end{aligned} \tag{3.16}$$

The second-order approximation is more accurate. However, it requires knowledge of the third and fourth statistical moments of $\tilde{X}$, which are difficult to estimate.

3.1.3.2. Statistical parameters of functions of two or more random variables

If $\tilde{Y}$ is a function of the n random variables $\tilde{X}_1, \tilde{X}_2, \dots, \tilde{X}_n$, then the corresponding Taylor's series expansion is defined by

$$\tilde{Y} = \mathrm{g}(\mu_{\tilde{X}_1}, \mu_{\tilde{X}_2}, \dots, \mu_{\tilde{X}_n}) + \sum_{i=1}^{n} (\tilde{X}_i - \mu_{\tilde{X}_i}) \left.\frac{\partial \mathrm{g}}{\partial x_i}\right|_{\boldsymbol{\mu}} + \frac{1}{2} \sum_{i=1}^{n} \sum_{j=1}^{n} (\tilde{X}_i - \mu_{\tilde{X}_i}) \left(\tilde{X}_j - \mu_{\tilde{X}_j}\right) \left.\frac{\partial^2 \mathrm{g}}{\partial x_i \partial x_j}\right|_{\boldsymbol{\mu}} + \cdots, \tag{3.17}$$

where $\boldsymbol{\mu}$ is the vector of mean values. The first-order approximations of the mean value and variance of $\tilde{Y}$ are

$$\mathrm{E}[\tilde{Y}] \cong \mathrm{g}(\boldsymbol{\mu}) \text{ and} \tag{3.18}$$

$$\mathrm{Var}[\tilde{Y}] \cong \sum_{i=1}^{n} \sum_{j=1}^{n} \mathrm{Cov}[\tilde{X}_i, \tilde{X}_j] \left[\left.\frac{\partial \mathrm{g}}{\partial x_i} \cdot \frac{\partial \mathrm{g}}{\partial x_j}\right|_{\mu} \right]. \tag{3.19}$$

The mean value of the second-order approximation is defined by

$$\mathrm{E}[\tilde{Y}] \cong \mathrm{g}(\boldsymbol{\mu}) + \frac{1}{2} \sum_{i=1}^{n} \sum_{j=1}^{n} \mathrm{Cov}[\tilde{X}_i, \tilde{X}_j] \left[\left.\frac{\partial^2 \mathrm{g}}{\partial x_i \partial x_j}\right|_{\boldsymbol{\mu}} \right]. \tag{3.20}$$

The variance obtained from the second-order approximation is difficult to express mathematically because it involves quadruple summations and fourth-order moments.

3.1.3.3. Central limit theorem

According to the central limit theorem, the sum or product of a large number of random variables, regardless of the type of distribution, tends to result in random variables that follow a normal (Gaussian) or log-normal p.d.f., respectively (BECK, 2019). This theorem is often used to justify the choice of a particular type of distribution, especially in cases where the p.d.f. cannot be defined exactly.

3.1.4.
First-order second-moment method

The first-order second-moment (FOSM) method is based on the expansion of the function g in terms of Taylor's series centered on the mean values $\left(\mu_{\tilde{X}_1}, \mu_{\tilde{X}_2}, \ldots, \mu_{\tilde{X}_n}\right)$ of the random variables $\tilde{X}_1, \tilde{X}_2, \ldots, \tilde{X}_n$. In this method, Eq. (3.17) is truncated after the linear term, hence the name "first-order". The truncated equation is then used to determine the first two statistical moments of the output random variables, hence the name "second-moment". According to Benaroya and Han (2005), the FOSM method is basically a formalized methodology based on a first-order Taylor's series expansion as defined by Eq. (3.13) and Eq. (3.14), for functions with only one random variable, or Eq. (3.18) and Eq. (3.19), for functions with two or more random variables.

In Eq. (3.19) and Eq. (3.20) the term $\mathrm{Cov}\left[\tilde{X}_i, \tilde{X}_j\right]$ refers to the covariance between the random variables $\tilde{X}_i$ and $\tilde{X}_j$, which is defined by

$$\begin{aligned}\mathrm{Cov}\left[\tilde{X}_i, \tilde{Y}_j\right] &= E\left[\left(\tilde{X}_i - \mu_{\tilde{X}_i}\right)\left(\tilde{X}_j - \mu_{\tilde{X}_j}\right)\right] \\ &= \int_{-\infty}^{\infty}\int_{-\infty}^{\infty}\left(x_i - \mu_{\tilde{X}_i}\right)\left(x_j - \mu_{\tilde{X}_j}\right) f_{\tilde{X}_i\tilde{X}_j}(x_i, x_j)\,dx_i dx_j\,.\end{aligned} \tag{3.21}$$

$\mathrm{Cov}\left[\tilde{X}_i, \tilde{X}_j\right]$ can also be written as a function of the correlation coefficient $\left(\rho_{\tilde{X}_i\tilde{X}_j}\right)$

$$\mathrm{Cov}\left[\tilde{X}_i, \tilde{Y}_j\right] = \rho_{\tilde{X}_i\tilde{X}_j}\sigma_{\tilde{X}_i}\sigma_{\tilde{X}_j}\,, \tag{3.22}$$

where $\sigma_{\tilde{X}_i}$ and $\sigma_{\tilde{X}_j}$ are the standard deviations of the variables $\tilde{X}_i$ and $\tilde{X}_j$, respectively.

3.1.5.
Monte Carlo simulation

Monte Carlo simulation (MCS) is an approximate statistical method used to solve problems involving randomness. In this method, the p.d.f. of the output random variables are defined from the equations that govern the deterministic problem. These equations are then solved several times using different input parameters, which are randomly extracted from a given sample space.

In general, this method provides an answer that approaches the "exact solution" when the number of realizations tends to infinity (BENAROYA et al., 2005). However, these methods are computationally expensive, and their use is indicated for validation and/or complementation of other statistical methods (LÖFMAN; KORKIALA-TANTTU, 2021; QI et al., 2022; WU et al., 2021).

3.2. Spatial variability of the mechanical properties of materials

The mechanical properties of soils and rocks can be analyzed as random variables due to their inherent spatial variability (VANMARCKE, 2010). This spatial variability can be understood considering the following situation: during the characterization of the geological formation, samples are extracted at two different points located within the same geological layer. If these two points are close, the mechanical properties are expected to be similar and close to the mean value (small fluctuation). If these points are distant, it is expected that these properties are more dispersed in relation to the mean value (great fluctuation), due to the presence of impurities, inhomogeneities generated during the formation process of the rock layer, fragmentation, or other causes. This fluctuation is measured using a scale, which describes the variability of these properties in space.

In this work, the spatial variability of the mechanical properties of the rocks is incorporated into the geomechanical problems through Gaussian and stationary stochastic random fields. Gaussian random fields are fully characterized by the mean value and variance of the input random variables. In stationary random fields, the marginal p.d.f. are constant at any point located in the problem domain, however the joint p.d.f. vary and depend only on the relative positions between these points. These considerations (Gaussian and stationary) make the mean value, variance, and higher-order moments constant within the problem domain. Fenton and Griffiths (2008) mention that the use of non-stationary correlation structures is uncommon in geotechnical and geomechanical problems due to the prohibitive amounts of data needed to estimate their parameters.

Gaussian and stationary random fields are characterized by three parameters: the mean value $\mu_{\tilde{X}_n}$, the variance $\sigma^2_{\tilde{X}_n}$, and the fluctuation scale θ, which defines how the random variables vary spatially. According to Vanmarcke (2010), this last parameter is characterized by the second moment of the joint p.d.f. of the random field variables, which can be considered by the covariance function, by the spectral density function, or by the variance function. The first method is used in the applications presented in this work.

3.2.1. Covariance function and correlation length

The second moments of a Gaussian random field can be considered using the definition of covariance from Eq. (3.21). However, this approach does not provide information about the degree of linear dependence between random variables $\tilde{X}_i(t')$ and $\tilde{X}_j(t^*)$. In this situation, a more meaningful measure can be obtained using the autocorrelation function

$$\rho_{\tilde{X}_i\tilde{X}_j}(\tau_x,\tau_y) = \frac{\mathrm{Cov}[\tilde{X}_i,\tilde{X}_j]}{\sigma_{\tilde{X}_i}\sigma_{\tilde{X}_j}}, \tag{3.23}$$

where the parameters τ_x and τ_y represent the relative horizontal and vertical distances between points t' and t^*, and the parameters $\sigma_{\tilde{X}_i}$ and $\sigma_{\tilde{X}_j}$ are the standard deviations of the random variables $\tilde{X}_i$ and $\tilde{X}_j$, respectively.

This linear dependence can also be interpreted using the concept of correlation length θ, also called fluctuation scale. In general, this parameter represents the distance at which the random variables $\tilde{X}_i(t')$ and $\tilde{X}_j(t^*)$ are significantly correlated (VANMARCKE, 2010). When the autocorrelation function assumes values close to zero, the mechanical properties of the materials vary considerably around the mean value and, in this case, the random variables that represent these properties are weakly correlated. On the other hand, when this function assumes values close to one, the mechanical properties present low variability, and they are strongly correlated. According to Li et al. (2015), it is important to estimate the fluctuation scale accurately because it plays a key role in characterizing the spatial variability of the mechanical properties of soils and rocks. Although there are methods that propose ways to quantify this scale in the field (LLORET-CABOT; FENTON; HICKS, 2014; UZIELLI; VANNUCCHI; PHOON, 2005), they are difficult to use because they require large amounts of data. As a result, theoretical functions have been used to characterize the spatial correlation of random variables in geotechnical problems. Table 3.1 and Figure 3.2 present some of these theoretical functions.

Table 3.1. Common autocorrelation function for geostatistical analysis (LI et al., 2015).

Type	***Function 2D***
Single exponential (SNX)	$\rho(\tau_x, \tau_y) = \exp\left[-2\left(\frac{\tau_x}{\theta_h} + \frac{\tau_x}{\theta_v}\right)\right]$
Squared exponential (SQX)	$\rho(\tau_x, \tau_y) = \exp\left[-\pi\left(\frac{\tau_x^2}{\theta_h^2} + \frac{\tau_x^2}{\theta_v^2}\right)\right]$
Second-order Markov (SMK)	$\rho(\tau_x, \tau_y) = \exp\left[-4\left(\frac{\tau_x}{\theta_h} + \frac{\tau_x}{\theta_v}\right)\right]\left(1 + \frac{4\tau_x}{\theta_h}\right)\left(1 + \frac{4\tau_y}{\theta_v}\right)$
Cosine exponential (CSX)	$\rho(\tau_x, \tau_y) = \exp\left[-\left(\frac{\tau_x}{\theta_h} + \frac{\tau_x}{\theta_v}\right)\right]\cos\left(\frac{\tau_x}{\theta_h}\right)\cos\left(\frac{\tau_y}{\theta_v}\right)$
Binary noise (BIN)	$\rho(\tau_x, \tau_y) = \begin{cases} \left(1 - \frac{\tau_x}{\theta_h}\right)\left(1 - \frac{\tau_y}{\theta_v}\right) & \text{for } \tau_x \leq \theta_h \text{ and } \tau_y \leq \theta_v \\ 0 & \text{otherwise} \end{cases}$

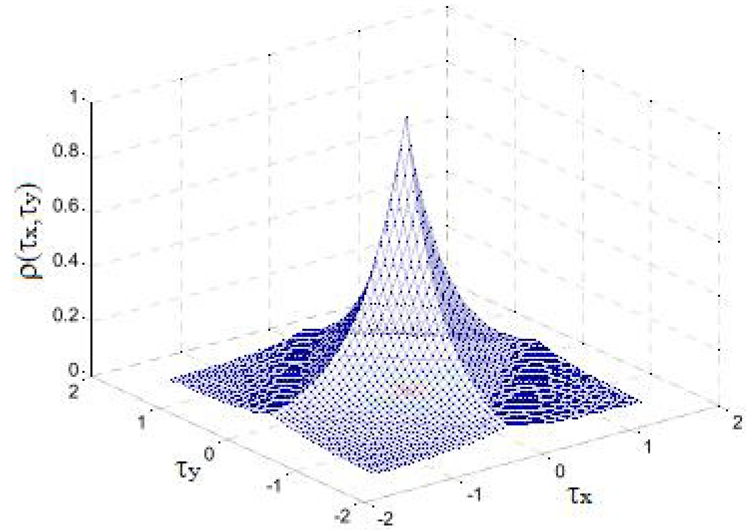

(a) SNX

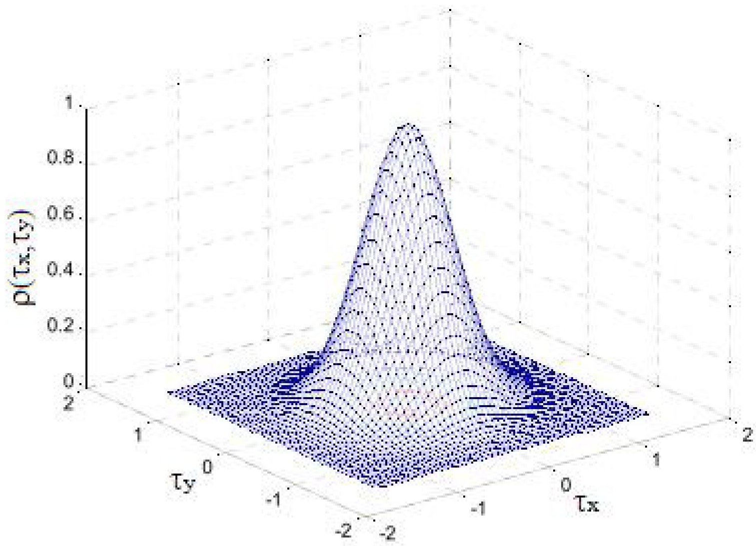

(b) SQX

Figure 3.2. Common 2D autocorrelation functions for geostatistical analysis (normalized to unit scales of fluctuation) (LI et al., 2015).

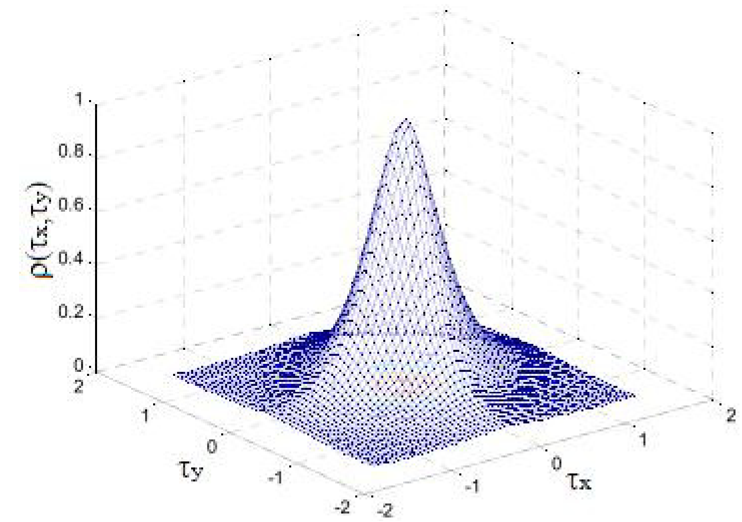

(c) SMK

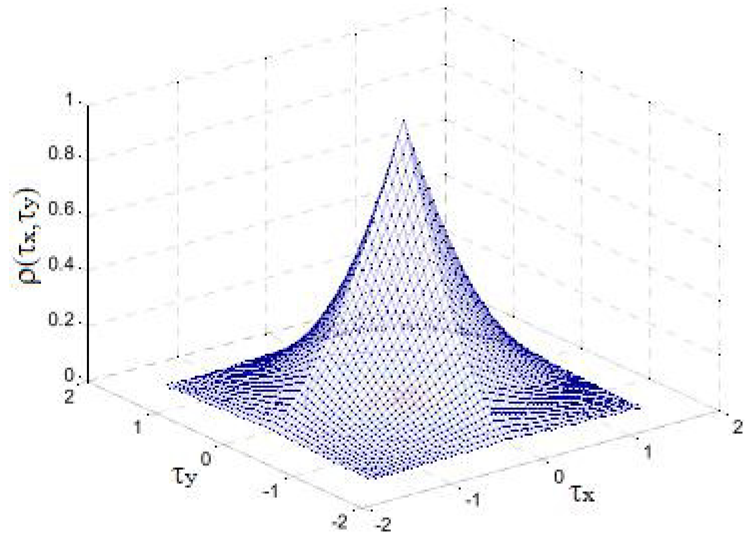

(d) CSX

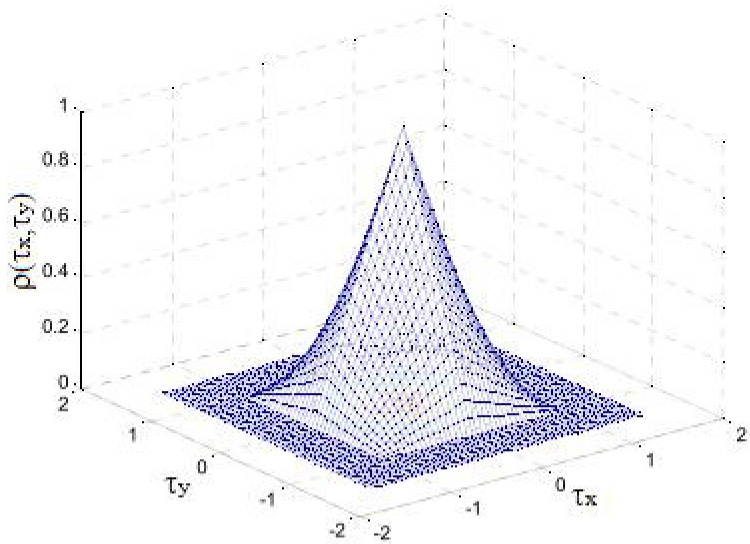

(e) BIN

Figure 3.2. Common 2D autocorrelation functions for geostatistical analysis (normalized to unit scales of fluctuation) (LI et al., 2015) (continuation).

3.3. Green's function approach

The Green's function approach (GFA) was originally proposed by Matheus L. Peres, Leonardo C. Mesquita, Yves M. Leroy, and Elisa D. Sotelino within the scope of the project "Modelagem Geomecânica do Pré-Sal", which was developed by PUC-Rio in partnership with TotalEnergies. The initial version of this method was published in 2021 by the International Journal for Numerical and Analytical Methods in Geomechanics in the paper entitled "Stress evolution in elastically heterogeneous and non-linear fluid-saturated media with a Green's function approach" (PERES et al., 2021)[4].

This method uses the classic Green functions (Kelvin's fundamental solution, Melan's fundamental solution, Mindlin's fundamental solution, or others) as an auxiliary solution that together with the reciprocity theorem calculate the variation of the displacement field of a geological formation subjected to fluid injection and/or extraction processes. This approach has no limitations in terms of geometry, number of layers, and heterogeneity of the geological profile and can be applied to materials with linear or non-linear behavior. Compared to the classic finite element method (FEM), the great advantage of the GFA is that it does not require the imposition of boundary conditions, and the analysis of the problem can be performed considering only the reservoir or other regions of interest.

In general, when analyzing a geomechanical model using FEM it is necessary to discretize a large region around the domain of interest (here called the semi-infinite medium) in order to represent the continuity of the geological profile and reduce the effect of boundary conditions on this region of interest. This increases the number of degrees of freedom of the problem and, consequently, the CPU time of the analysis. Thus, to obtain the deterministic response of complex 3D models, it may need a CPU time of the order of hours or days. In these situations, it is certainly not computationally feasible to obtain the statistical answer to the problem. When using the GFA, it is not necessary to perform the discretization of the semi-infinite medium, which reduces the CPU time of the analysis. At the same time, this makes the GFA a computationally viable method to consider the inherent uncertainties contained in geomechanical problems. The GFA can also be classified

[4] DOI: 10.1002/nag.3204

as an analysis method for unbounded problems because the domain around reservoir regions is treated as infinite or semi-infinite. The GFA formulation and its extension to consider the uncertainties associated with the mechanical properties of materials in geomechanical problems are detailed in the next chapters.

4
“Uncertainties consideration in elastically heterogeneous fluid-saturated media using the first-order second-moment stochastic method and Green’s function approach”

Paper published by Leonardo C. Mesquita, Elisa D. Sotelino, and Matheus L. Peres in the Applied Mathematical Modelling[5].

Abstract

The present work proposes a stochastic statistical method, called Green-FOSM, to consider the uncertainties associated with the mechanical properties of rocks that form geological profile. This method intended to help improve the decision-making process associated with the production of oil and gas, the extraction of water, and the storage of CO_2 or natural gas. The novelty of the method lies in the use of Green’s function approach, which, together with the FOSM method (first-order second-moment method), is used to propagate uncertainties associated with the material to the displacement field of the geological formation. Furthermore, using the concepts of stochastic grid and autocorrelation function, the proposed method allows the consideration of the spatial variability of the random variables that represent these mechanical properties. This method is applied to a 2D model subject to two processes of pore pressure changes (depletion only and depletion combined with injection) with different levels of correlation and variability. The statistical results obtained by the proposed method agree well with the results obtained using Monte Carlo simulation. In problems with more than 1500 random variables, the relationship between the CPU times demonstrates that the proposed method is up to 30 times faster than the Monte Carlo simulation.

[5] DOI: 10.1016/j.apm.2022.11.012

4.1. Introduction

Human activities related to the process of fluid injection or depletion in underground reservoirs, such as the production of oil and gas (MINKOFF; KRIDLER, 2006; MORGAN; LEWIS; WHITE, 1980), the extraction of water (TEATINI et al., 2006), and the storage of CO_2 or natural gas (FERRONATO et al., 2010; NAGELHOUT; ROEST, 1997; TEATINI et al., 2011), generate changes in the displacement, strain, and stress fields in the geological formation. As a direct consequence of these changes, there is the swelling or compaction of the reservoir rock and, consequently, the subsidence of the free surface (BAÙ et al., 2015). These changes can also generate secondary effects as, for example, wellbore collapse and offshore platform failure (MINKOFF; KRIDLER, 2006), decreased production due to reduced porosity and permeability of the geological formation (FERRONATO et al., 2006), fault reactivation, and seismic events (BOURNE et al., 2014; PAULLO MUÑOZ; ROEHL, 2017; VERDON et al., 2016). In the last decades, several examples of subsidence due to fluid depletion have been reported in various places such as Wilmington field in the USA (COLAZAS; STREHLE, 1995), Boscan field in Venezuela (FINOL; SANCEVIC, 1995), Ekofisk field in Norway (HERMANSEN et al., 2000; KRISTIANSEN; PLISCHKE, 2010), Dan field in Denmark (HATCHELL et al., 2007), Groningen field in Netherlands (VAN THIENEN-VISSER; FOKKER, 2017), Lower Loathe Plain in China (SUN et al., 2017). From an environmental point of view, changes in the displacement, strain, and stress fields can modify the transport of solutes in underground aquifers. According to Bonazzi et al. (2021), the water-level decline associated with subsidence modifies hydrological fluxes and can lead to deterioration of water quality, due to a greater probability of seawater or wastewater infiltration in the aquifer. In addition, the fault reactivation process can increase the likelihood of aquifer contamination. These events have motivated the development of analytical and numerical methods to predict changes in the displacement, strain, and stress fields.

Among the analytical methods proposed to date, one of the most renowned is the method proposed by Geertsma (GEERTSMA, 1957, 1973a, 1973b), which is based on the theory of poroelasticity and nucleus-of-strain concept (LEWIS;

MORGAN; WHITE, 1983; MINDLIN; CHENG, 1950). Using this method, it is possible to calculate the displacements and stresses in a homogeneous geological formation assuming that the reservoir has a cylindrical shape and is subjected to a uniform depletion. In order to make this method more comprehensive, over the last few years, several researchers have expanded the equations originally proposed by Geertsma (DU; OLSON, 2001; FOKKER; ORLIC, 2006; MEHRABIAN; ABOUSLEIMAN, 2015; PAULLO MUÑOZ; ROEHL, 2017; SEGALL, 1992; TEMPONE; FJÆR; LANDRØ, 2010; VAN OPSTAL, 1975). In general, analytical methods have the advantage of being simple, however, they are limited in relation to geometry, heterogeneity of the geological profile, and mechanical behavior of materials. To overcome these limitations, numerical methods are used. These methods, usually based on the finite element method (FEM) (BELAYNEH; GEIGER; MATTHÄI, 2006; HADDAD; EICHHUBL, 2020; LELE et al., 2016; SETTARI; WALTERS, 2001; WATANABE et al., 2010), are able to consider the particularities of each geological formation, however, in most situations, they demand a high computational effort for the construction and processing of models. Green's function approach, proposed by Peres et al. (2021), is a hybrid method in which analytical equations are numerically solved. As in the analytical methods, this method is simple and computationally efficient, however, it does not have limitations in relation to geometry, number of layers, and heterogeneity of the geological profile and can be applied to linear and non-linear material behavior. The great advantage of this method compared to the classic FEM is that it does not require the imposition of boundary conditions and the analysis can be performed considering only the reservoir or other regions of interest.

All methods discussed above deal with the effects of human activities related to the fluid injection or depletion processes in a deterministic way, that is, they do not consider the uncertainties associated with this process. However, uncertainties can greatly affect the results obtained by these methods (BAÙ et al., 2016) and lead to responses that do not faithfully represent in-situ observations (MULLER et al., 2009a, 2009b). In geotechnical and geomechanical problems, the main source of uncertainties is associated with the inherent spatial variability of the mechanical properties of materials (DENG et al., 2017; GEDDES, 1977; SUCHOMEL; MAŠÍN, 2010).

The aforementioned uncertainties have been included in the analytical or numerical models through statistical simulation-based methods (YANG; CHING, 2019), among which Monte Carlo simulation (MCS) is the most commonly adopted. In the geotechnical field, this statistical method has been used in slope stability problems (DENG et al., 2017; EL-RAMLY; MORGENSTERN; CRUDEN, 2002; SUCHOMEL; MAŠÍN, 2010) and foundation settlement (BRZĄKAŁA; PUŁA, 1996; BUNGENSTAB; BICALHO, 2016). In the hydrogeological field, applications are found in problems related to solute transport in aquifers (FIORI et al., 2015), and groundwater flow (SOHN; SMALL; PANTAZIDOU, 2000). In the geomechanical case, it has been used in wellbore stability problems (BATALHA et al., 2020; MULLER et al., 2009b, 2009a; UDEGBUNAM; AADNØY; FJELDE, 2014), in inverse analyzes, to calibrate the parameters of reservoir models using in-situ subsidence data (AICHI, 2020; BAÙ et al., 2015, 2016; BOTTAZZI; DELLA ROSSA, 2017; GAZZOLA et al., 2020; ZOCCARATO et al., 2020), and in problems with uncertainties related to the hydraulic conductivity of materials (FRIAS; MURAD; PEREIRA, 2004). In MCS, the statistical response is calculated through the deterministic equations of the problem, which are solved repeatedly using several sets of parameters generated randomly from the probability density function of the input variables (HWANG; LANSEY; JUNG, 2018; MALLOR et al., 2020). Subsequently, the set of deterministic results is analyzed in statistical terms in order to obtain the mean value, the variance, and the probability density function of the output variables. As MCS uses the deterministic equations of the problem, it can be performed with any analytical or numerical method without the need for complex computational implementations.

The MCS often demands great computational effort, as it may require thousands or millions of repetitions before reaching satisfactory results, which limits its application in complex problems, such as the problems related to the fluid injection or depletion (WU et al., 2018). In these problems, statistical methods approximated by Taylor series expansion can be used as an alternative to MCS, since they are computationally more efficient (WENXIN; ZHENZHOU, 2018; YANG; CHING, 2020). Among these approximate methods, the first-order second moment (FOSM) method stands out. In this statistical method, the first and second statistical moments (hence “second moment”) are approximated using the first terms of the Taylor series expansion (hence “first-order”) about the mean value (FENTON; GRIFFITHS, 2008). In the literature, there are applications of this method for the treatment of different types of problems, such as uncertainties quantification of creep in concrete (CRIEL et al., 2017) and seismic hazard assessment (WANG; YUN; WU, 2013). In the geotechnical field, this method has been applied in studies of tunnel stability (CHENG et al., 2019), slope stability (DUNCAN, 2000; SUCHOMEL; MAŠÍN, 2010), and foundation settlement (BUNGENSTAB; BICALHO, 2016). In geomechanical problems, its applications are limited to estimating reserves and forecasting production (MISHRA, 1998).

In view of this scenario, it is identified a gap in knowledge between the deterministic methods used to predict the changes generated by the fluid injection or depletion and the uncertainties related to the mechanical properties of rocks that make up the geological formation. Thus, this paper aims to contribute to address this gap. More specifically, it presents a computationally efficient stochastic statistical method, based on Green’s function approach and the FOSM method, which allows the prediction of changes in the displacement field generated by variations in pore pressure and, at the same time, considers the spatial variability of the mechanical properties of the rocks that form the geological profile.

4.2. Green’s function approach

4.2.1 Stress, fluid pressure change, and mechanical equilibrium

During the fluid injection or depletion process, changes in the pore pressure occur within the reservoir (subdomain Ω_R). Such changes will modify the displacement, strain, and stress fields of the entire problem domain (Ω_t). Defining $\Delta\sigma_{ij}$ as the variation of the stress state $\Delta\sigma_{ij}$ generated by a Δp change in pore pressure, the mechanical equilibrium for the total stress (initial + change) is enforced by

$$\left(\sigma_{ij,j} + \Delta\sigma_{ij,j}\right) + f_i = 0 \quad \forall\, x_i \in \Omega_t, \tag{4.1}$$

at any material point indicated by the vector x_i within the domain Ω_t. The term f_i represents an external field initially generated by body or surface forces.

In general, in geomechanical analyses, the displacements generated by a change in pore pressure (Δp) are small when compared to the characteristic dimensions of the problem. Thus, it is assumed that the problem can be analyzed considering small deformations and displacements. The first consequence is that the linearized strain tensor can be used and is given by

$$\varepsilon_{ij} = \frac{1}{2}\left(u_{i,j} + u_{j,i}\right). \tag{4.2}$$

The second consequence is that in the absence of geometrical effects in Eq. (4.1), the local equilibrium conditions for the stress changes are

$$\Delta\sigma_{ij,j} + f_i = 0 \quad \forall\, x_i \in \Omega_t, \tag{4.3}$$

where f_i represents any field of interest, except for the fields considered initially, since Eq. (4.1) is satisfied by the initial stress before any stress change. Therefore, the problem to be solved is one in which the displacement and strain fields are initially set to zero, and the changes in pore pressure (Δp) over the subdomain (Ω_R) results in a displacement field (u_i), a strain field according to Eq. (4.2), and a stress change ($\Delta\sigma_{ij}$) that satisfies the equilibrium condition of Eq. (4.3).

4.2.2
Linear poroelasticity for heterogeneous problems

According to the theory of linear poroelasticity proposed by Biot (1941), the variation of the stress state $\Delta\sigma_{ij}$ generated by a Δp change in pore pressure can be calculated as follows:

$$\Delta\sigma_{ij} = \mathbb{C}^{e}_{ijkl}\,\varepsilon_{kl} - A_{ij}\,\Delta p, \tag{4.4}$$

where $\mathbb{C}^{e}_{ijkl}$, ε_{kl}, and A_{ij} are the fourth-order stiffness tensor, the second-order strain tensor, and the second-order Biot tensor, respectively. Eq. (4.4) is only applicable to homogeneous problems. In the case of heterogeneous problems (heterogeneity generated by the difference among the elastic properties of the rocks that make up the geological formation), Peres et al. (2021) propose the inclusion of additional tensor $\Delta\bar{\sigma}_{ij}(x)$ given by:

$$\Delta\bar{\sigma}_{ij}(x) = \left[\mathbb{C}^{e}_{ijkl} - \mathbb{C}_{ijkl}(x)\right]\varepsilon_{kl}, \tag{4.5}$$

which represents the difference between the elastic properties of the homogeneous and heterogeneous problems. In this equation, Eq. (4.5), $\mathbb{C}_{ijkl}(x)$ is the fourth-order stiffness tensor obtained from the mechanical properties of materials found in an x position contained in the problem domain (Ω_t). Thus, the equation for linear poroelasticity applied to heterogeneous problems can be rewritten as:

$$\Delta\sigma_{ij} = \mathbb{C}^{e}_{ijkl}\, \varepsilon_{kl} - A_{ij}\, \Delta p - \Delta\bar{\sigma}_{ij}(x). \tag{4.6}$$

4.2.3
Reciprocity theorem extended to linear, heterogeneous porous media

During the fluid injection or depletion process, changes in the pore pressure occur within the reservoir (subdomain Ω_R). Such changes will modify the displacement, strain, and stress fields of the entire problem domain (Ω_t). Using the principle of virtual work, it is possible to establish the following relationship between the displacement field and the strain and stress fields:

$$\int_{\Omega_t} \Delta\sigma_{ij}\, \hat{\varepsilon}_{ij}\, \mathrm{d}V = \int_{\partial\Omega_t} \Delta T_i\, \hat{u}_i\, \mathrm{d}S + \int_{\Omega_t} f_i\, \hat{u}_i\, \mathrm{d}V, \tag{4.7}$$

where $\hat{u}_i$ is any virtual displacement vector associated with the virtual strain tensor $\hat{\varepsilon}_{ij}$, ΔT_i represents the variation of surfaces forces caused by the fluid injection or depletion processes and f_i is the force vector that does not consider the surface forces.

The reciprocity theorem is the basis of Green's function approach (PERES et al., 2021). Using this theorem, the displacement field of the geomechanical problem (real problem) can be calculated with the aid of a fundamental solution (auxiliary problem), whose analytical answers are known (Kelvin fundamental solution, Melan fundamental solution, among others). For this, consider that the real problem (index 1) and the auxiliary problem (index 2) have the same domain (Ω_t) and the same boundary conditions. Applying Eq. (4.7) to the real problem with the virtual field corresponding to the auxiliary problem and vice versa, we have:

$$\int_{\Omega_t} \Delta\sigma^{(1)}_{ij}\, \hat{\varepsilon}^{(2)}_{ij}\, \mathrm{d}V = \int_{\partial\Omega_t} \Delta T^{(1)}_i\, \hat{u}^{(2)}_i\, \mathrm{d}S + \int_{\Omega_t} f^{(1)}_i\, \hat{u}^{(2)}_i\, \mathrm{d}V, \tag{4.8}$$

$$\int_{\Omega_t} \Delta\sigma^{(2)}_{ij}\, \hat{\varepsilon}^{(1)}_{ij}\, \mathrm{d}V = \int_{\partial\Omega_t} \Delta T^{(2)}_i\, \hat{u}^{(1)}_i\, \mathrm{d}S + \int_{\Omega_t} f^{(2)}_i\, \hat{u}^{(1)}_i\, \mathrm{d}V. \tag{4.9}$$

Using Eq. (4.6), the left sides of Eq. (4.8) and Eq. (4.9) can be rewritten as follows:

$$\int_{\Omega_t} \Delta\sigma_{ij}^{(1)}\,\hat{\varepsilon}_{ij}^{(2)}\,\mathrm{d}V = \int_{\Omega_t} \hat{\varepsilon}_{ij}^{(2)}\,\mathbb{C}_{ijkl}^{e}\,\varepsilon_{kl}^{(1)}\,\mathrm{d}V - \int_{\Omega_R} A_{ij}\,\Delta p^{(1)}\,\hat{\varepsilon}_{ij}^{(2)}\,\mathrm{d}V - \int_{\Omega_t} \Delta\bar{\sigma}_{ij}^{(1)}(x)\,\hat{\varepsilon}_{ij}^{(2)}\,\mathrm{d}V, \tag{4.10}$$

$$\int_{\Omega_t} \Delta\sigma_{ij}^{(2)}\,\hat{\varepsilon}_{ij}^{(1)}\,\mathrm{d}V = \int_{\Omega_t} \hat{\varepsilon}_{ij}^{(1)}\,\mathbb{C}_{ijkl}^{e}\,\varepsilon_{kl}^{(2)}\,\mathrm{d}V - \int_{\Omega_R} A_{ij}\,\Delta p^{(2)}\,\hat{\varepsilon}_{ij}^{(1)}\,\mathrm{d}V - \int_{\Omega_t} \Delta\bar{\sigma}_{ij}^{(2)}(x)\,\hat{\varepsilon}_{ij}^{(1)}\,\mathrm{d}V. \tag{4.11}$$

As the constitutive tensor $\mathbb{C}_{ijkl}^{e}$ is symmetric, the first integrals on the right side of the Eq. (4.10) and Eq. (4.11) are equal, resulting in:

$$\begin{aligned} &\int_{\partial\Omega_t} \Delta T_i^{(1)}\,\hat{u}_i^{(2)}\,\mathrm{d}S + \int_{\Omega_t} f_i^{(1)}\,\hat{u}_i^{(2)}\,\mathrm{d}V + \int_{\Omega_R} A_{ij}\,\Delta p^{(1)}\,\hat{\varepsilon}_{ij}^{(2)}\,\mathrm{d}V \\ &\qquad + \int_{\Omega_t} \Delta\bar{\sigma}_{ij}^{(1)}(x)\,\hat{\varepsilon}_{ij}^{(2)}\,\mathrm{d}V = \\ &\int_{\partial\Omega_t} \Delta T_i^{(2)}\,\hat{u}_i^{(1)}\,\mathrm{d}S + \int_{\Omega_t} f_i^{(2)}\,\hat{u}_i^{(1)}\,\mathrm{d}V + \int_{\Omega_R} A_{ij}\,\Delta p^{(2)}\,\hat{\varepsilon}_{ij}^{(1)}\,\mathrm{d}V \\ &\qquad + \int_{\Omega_t} \Delta\bar{\sigma}_{ij}^{(2)}(x)\,\hat{\varepsilon}_{ij}^{(1)}\,\mathrm{d}V. \end{aligned} \tag{4.12}$$

In the real problem (superscript 1), the unknown displacements are generated only by the change in pore pressure Δp, therefore, the vectors $\Delta T_i^{(1)}$ and $f_i^{(1)}$ can be suppressed. In the auxiliary problem (superscript 2), the unknown displacements come from a unit point load applied in a position X of the domain (Ω_t) and, therefore, the vector $\Delta T_i^{(2)}$ and the pore pressure $\Delta p^{(2)}$ can be disregarded

(LEHNER; KNOGLINGER; D, 2005). Furthermore, as the fundamental solution used to solve the auxiliary problem consider homogeneous materials, the tensor $\Delta\bar{\sigma}_{ij}^{(2)}(x)$ is null. Removing the superscripts (1) and (2), Eq. (4.12) can be rewritten as:

$$u_k(X_i) = \int_{\Omega_R} \alpha(x_i)\,\Delta p(x_i)\,\delta_{mn}\,\varepsilon_{mnk}^*(X_i, x_i)\,\mathrm{d}V + \int_{\Omega_t} \Delta\bar{\sigma}_{mn}(x_i)\,\varepsilon_{mnk}^*(X_i, x_i)\,\mathrm{d}V, \quad (4.13)$$

where u_k is the horizontal ($k = 1$) or vertical ($k = 2$) displacement in the position X_i, α is the Biot coefficient, Δp is the pore pressure variation, δ_{ij} is the Kronecker delta, ε_{mnk}^* are the strains in the x_i position obtained from the fundamental solution considering a unit point load (horizontal for the calculation of the horizontal displacement or vertical, otherwise) applied in the X_i position, and $\Delta\bar{\sigma}_{mn}$ is the tensor that corresponds to the stress variation generated by the differences between the mechanical properties of the real problem and the auxiliary problem.

In Eq. (4.13) the first integral is applied to the subdomain (Ω_R), which represent the reservoir region, that is, the region where the pore pressure change will occur, and the second integral is applied to the domain (Ω_t), which is the real problem domain. The numerical examples presented in this work use as a Green's function (auxiliary problem) the 2D Melan's solution (MELAN, 1932), which considers a point load applied in a semi-infinite domain (plane strain state). The equations for calculating the ε_{mnk}^* strains were taken from Telles and Brebbia (1981) and are presented in Appendix A. The Green's function approach can be extended to three-dimensional applications using a suitable Green's function, for example, the 3D Kelvin solution (infinite domain) or Mindlin's solution (semi-infinite domain).

4.2.4 Numerical scheme

There are two ways to solve Eq. (4.13), which is implicit in terms of the displacement field. The first method consists of determining the strains ε_{kl}, Eq. (4.5), by directly calculating the strain gradient $\partial u_k / \partial x_i$ from the differentiation of

Eq. (4.13). The second method, which is simpler, consists of discretizing the Ω_t domain in N_t triangular regions, generating a mesh similar to those in the finite element method. Using this mesh, the displacements are calculated at each node through Eq. (4.13). In this work, linear interpolation is used to construct the displacement field. As a result, the stress $\Delta\bar{\sigma}_{mn}$ is uniform in each element and the displacement $u_k(X_i)$ can be calculated by:

$$
\begin{aligned}
u_k(X_i) = &\sum_{b=1}^{N_{\Omega_R}} \alpha(x_i)^{(b)}\, \Delta p(x_i)^{(b)} \int_{\Omega_R^{(b)}} \delta_{mn}\, \varepsilon^*_{mnk}(X_i, x_i)\, \mathrm{d}V \\
&+ \sum_{b=1}^{N_{\Omega_t}} \Delta\bar{\sigma}_{mn}(x_i)^{(b)} \int_{\Omega_t^{(b)}} \varepsilon^*_{mnk}(X_i, x_i)\, \mathrm{d}V\,,
\end{aligned}
\tag{4.14}
$$

where N_{Ω_R} is the number of elements in the reservoir region (subdomain Ω_R) and N_{Ω_t} is the number of elements in the entire model (domain Ω_t). The additional term $\Delta\bar{\sigma}_{mn}$ and the deformations ε_{jk} are calculated from the displacements $u_k(X_i)$ and, thus, Eq. (4.14) must be solved interactively. For this, Peres et al. (2021) propose an iterative method, in which the displacement field of the step n is used to calculate the strains ε_{jk} and the stresses $\Delta\bar{\sigma}_{mn}$ in step $n+1$. The initial displacement $u_k(X_i)$ is calculated considering only the first summation of Eq. (4.14) and the convergence of the method is based on the error measure δu_k calculated using the nodal displacements in steps $n+1$ and n, given by:

$$
\delta u_k = \frac{1}{N}\sum_{i=1}^{N}\left|\frac{u_k(X_i)^{(n+1)} - u_k(X_i)^{(n)}}{u_k(X_i)^{(n)}}\right| \le t_k\,,
\tag{4.15}
$$

where $u_k(X_i)^{(n+1)}$ is the displacement at position X_i calculated in step $n+1$, $u_k(X_i)^{(n)}$ is the displacement at position X_i calculated in step n, N is the number of nodes in the problem, and t_k is the tolerance used as a stopping criterion. The convergence of this iterative method is widely discussed by Peres et al. (2021).

The two integrals of the right side of Eq. (4.14) are solved numerically using the Gaussian quadrature, when the auxiliary problem is not singular, or the Bartholomew quadrature (BARTHOLOMEW, 1959) associated with the Duffy transformation (BONNET, 2017; MOUSAVI; SUKUMAR, 2010), when the auxiliary problem is singular. As can be seen in Appendix A, the equations of the 2D Melan's solution are proportional to the terms $1/r$ (2D Kelvin's solution part) and $1/R$ (complementary part) which are singular when the position X_i of the unit point load applied approaches the evaluation point x_i. Additional information on the treatment of singularity points using Bartholomew quadrature and Duffy's transformation is presented in Appendix B.

4.3. Uncertainties consideration using Green's function approach

4.3.1. FOSM based on Green's function approach

Using Eq. (4.14), it is possible to calculate deterministically the changes in the displacement field generated by the fluid injection or depletion process. To consider the uncertainties inherent in the properties of materials, Green's function approach can be extended using statistical methods. In these methods, the mechanical properties of materials are considered as random variables defined by their statistical moments and probability density function $f_{\tilde{Y}}(\tau)$. This extension is done using statistical methods that can propagate uncertainties from random input variables to random variables that represent the answer to the problem, which can be exact or approximate.

According to Fenton e Griffiths (2008), exact methods use the concept of random variables functions, in which the probability density functions of input ($\tilde{X}_i$) and output ($\tilde{Y}_i$) random variables are calculated analytically through a function $\tilde{Y}_i = \mathrm{g}(\tilde{X}_i)$. For complex $\mathrm{g}(\tilde{X}_i)$ functions, as in the case of Eq. (4.14), the use of exact methods become impracticable. In these situations, the propagation of uncertainties can be performed using approximate methods, such as the MCS and the FOSM method.

In MCS, Eq. (4.14) is solved K times and, in each of these times, the input variables assume random values defined from their probability density functions $f_{\tilde{X}_i}(\tau)$. After the K realizations, the statistical moments and the probability density functions $f_{\tilde{Y}_i}(\tau)$ that represent the output random variables (in this case, the nodal displacements) are obtained. In the FOSM method, the statistical moments of the output random variables are determined through the first terms of the Taylor series expansion about the mean values ($\mu_{\tilde{X}_N}$) of the N random variables (ANG; TANG, 2015) as shown in Eq. (4.16) and Eq. (4.17):

$$\mathrm{E}\left[\tilde{Y}\left(\tilde{X}_1, \tilde{X}_2, \dots, \tilde{X}_N\right)\right] \approx \mathrm{g}\left(\mu_{\tilde{X}_1}, \mu_{\tilde{X}_2}, \dots, \mu_{\tilde{X}_N}\right), \qquad \text{and} \tag{4.16}$$

$$\mathrm{Var}\left[\tilde{Y}\left(\tilde{X}_1, \tilde{X}_2, \dots, \tilde{X}_N\right)\right] \approx \sum_{m=1}^{N} \sum_{n=1}^{N} \left(\frac{\partial \mathrm{g}\left(\mu_{\tilde{X}_1}, \mu_{\tilde{X}_2}, \dots, \mu_{\tilde{X}_N}\right)}{\partial \tilde{X}_m}\right)\left(\frac{\partial \mathrm{g}\left(\mu_{\tilde{X}_1}, \dots, \mu_{\tilde{X}_N}\right)}{\partial \tilde{X}_n}\right) \rho_{mn} \sigma_m \sigma_n. \tag{4.17}$$

In these equations, μ_m and σ_m are the mean value and standard deviation of the random variable m, and ρ_{mn} is the linear correlation coefficient between the random variables m and n. Differently of MCS, in the FOSM method is not necessary to know the probability density function $f_{\tilde{X}_m}(\tau)$ of the input random variables, because in this method the uncertainties are propagated using only the first two statistical moments (mean value and variance) and the linear correlation coefficient ρ_{mn} (CRIEL et al., 2017). As mentioned before, the great advantage of this method is related to CPU time, which is usually lower than the CPU time consumed via MCS.

Associating the Green's function approach, Eq. (4.14), with the FOSM method, Eq. (4.16) and Eq. (4.17), the mean values and variances of the nodal displacements (represented by the output random variable $\widetilde{U}_k$) at X_i position are given by:

$$\mathbb{E}\left[\widetilde{U}_k\left(X_i, \tilde{X}_1, \tilde{X}_2, \dots, \tilde{X}_N\right)\right] \approx u_k\left(X_i, \mu_{\tilde{X}_1}, \mu_{\tilde{X}_2}, \dots, \mu_{\tilde{X}_N}\right), \qquad \text{and} \tag{4.18}$$

$$\mathrm{Var}\left[\widetilde{U}_k\left(X_i, \tilde{X}_1, \dots, \tilde{X}_N\right)\right] = \left(\sum_{b}^{N_{\Omega_R}} \mathbb{D}_p^{(\Omega_R)(b)} + \sum_{b}^{N_{\Omega_t}} \mathbb{D}_p^{(\Omega_t)(b)}\right)\left(\sum_{b}^{N_{\Omega_R}} \mathbb{D}_q^{(\Omega_R)(b)} + \sum_{b}^{N_{\Omega_t}} \mathbb{D}_q^{(\Omega_t)(b)}\right) \mathbb{C}\left(\rho_{\tilde{X}_{pq}}, \sigma_{\tilde{X}_p}, \sigma_{\tilde{X}_q}\right), \tag{4.19}$$

where $\mathbb{D}_p^{(\Omega_R)(b)}$ is the vector of the partial derivatives of the displacements generated by each triangular region of the subdomain Ω_R in relation to the N input random variables, $\mathbb{D}_p^{(\Omega_t)(b)}$ is the vector of the partial derivatives of the displacements generated by each triangular region of the domain Ω_t in relation to the N input random variables, defined by:

$$\mathbb{D}_p^{(\Omega_R)(b)} = \begin{Bmatrix} \dfrac{\partial u_k^{(\Omega_R)(b)}\left(X_i, \mu_{\tilde{X}_1}, \mu_{\tilde{X}_2}, \dots, \mu_{\tilde{X}_N}\right)}{\partial \tilde{X}_1} \\ \vdots \\ \dfrac{\partial u_k^{(\Omega_R)(b)}\left(X_i, \mu_{\tilde{X}_1}, \mu_{\tilde{X}_2}, \dots, \mu_{\tilde{X}_N}\right)}{\partial \tilde{X}_p} \end{Bmatrix}$$

$$= \begin{Bmatrix} \dfrac{\partial}{\partial \tilde{X}_1}\left(\alpha(x_i)^{(b)} \Delta p(x_i)^{(b)} \int\limits_{\Omega_R^{(b)}} \delta_{mn}\, \varepsilon_{mnk}^{*}(X_i, x_i)\, \mathrm{d}V \right) \\ \vdots \\ \dfrac{\partial}{\partial \tilde{X}_p}\left(\alpha(x_i)^{(b)} \Delta p(x_i)^{(b)} \int\limits_{\Omega_R^{(b)}} \delta_{mn}\, \varepsilon_{mnk}^{*}(X_i, x_i)\, \mathrm{d}V \right) \end{Bmatrix}, \quad \text{and} \tag{4.20}$$

$$\mathbb{D}_p^{(\Omega_t)(b)} = \begin{Bmatrix} \dfrac{\partial u_k^{(\Omega_t)(b)}\left(X_i, \mu_{\tilde{X}_1}, \mu_{\tilde{X}_2}, \dots, \mu_{\tilde{X}_N}\right)}{\partial \tilde{X}_1} \\ \vdots \\ \dfrac{\partial u_k^{(\Omega_t)(b)}\left(X_i, \mu_{\tilde{X}_1}, \mu_{\tilde{X}_2}, \dots, \mu_{\tilde{X}_N}\right)}{\partial \tilde{X}_p} \end{Bmatrix}$$

$$= \begin{Bmatrix} \dfrac{\partial}{\partial \tilde{X}_1}\left(\Delta\bar{\sigma}_{mn}(x_i)^{(b)} \int\limits_{\Omega_t^{(b)}} \varepsilon_{mnk}^{*}(X_i, x_i)\, \mathrm{d}V \right) \\ \vdots \\ \dfrac{\partial}{\partial \tilde{X}_p}\left(\Delta\bar{\sigma}_{mn}(x_i)^{(b)} \int\limits_{\Omega_t^{(b)}} \varepsilon_{mnk}^{*}(X_i, x_i)\, \mathrm{d}V \right) \end{Bmatrix}. \tag{4.21}$$

The $\mathbb{C}\left(\rho_{\tilde{X}_{pq}}, \sigma_{\tilde{X}_p}, \sigma_{\tilde{X}_q}\right)$ matrix considers the spatial variability of input random variables that represent the mechanical properties of materials, as further discussed in the next section.

4.3.2. Random variables, stochastic grid, and spatial variability of properties

The mechanical properties of soils and rocks can be considered random variables due to their inherent spatial variability (VANMARCKE, 2010). This spatial variability is exemplified considering two distinct points located within the same geological layer. If these points are close, the mechanical properties are similar and close to the mean value. Otherwise, these properties show a greater fluctuation in relation to the mean value, due to the presence of impurities, inhomogeneities generated during the formation of the rock layer, fragmentation, or other causes. This fluctuation is measured though a scale, which describes the spatial variability of these properties, forming a random field. From a statistical point of view, this spatial variability is introduced into the geomechanical problem through a stochastic random field, here represented by the domain (Ω_t) of the problem. As proposed by Cho (2012) and Li et al. (2015), the domain Ω_t is then partitioned into several subdomains Ω_i forming a stochastic grid, in which the input random variables are significantly correlated and consequently there is no fluctuation. This fluctuation is considered between two subdomains Ω_i using an autocorrelation parameter, which varies from 0 (properties fluctuates rapidly about the mean values) to 1 (properties are significantly correlated).

According to Li et al. (2015), it is important to estimate the scale of fluctuation accurately because it plays a key role in characterizing the spatial variability of the mechanical properties of soils and rocks. Although there are methods that propose the quantification of this fluctuation scale in the field (LLORET-CABOT; FENTON; HICKS, 2014; UZIELLI; VANNUCCHI; PHOON, 2005), these methods are difficult to apply because large amounts of data are required. As a result, theoretical autocorrelation functions have been used to characterize the spatial correlation of soil mechanical properties. This type of approach has been widely used in geotechnical problems, however, in geomechanical problems no reference was found. Assuming that $\rho\left(\tau_{x_{pq}}, \tau_{y_{pq}}\right)$ is the autocorrelation function between the random variables $\tilde{X}_p$ and $\tilde{X}_q$ that belong to the subdomains Ω_p and Ω_q, respectively, the matrix $\mathbb{C}\left(\rho_{\tilde{X}_{pq}}, \sigma_{\tilde{X}_p}, \sigma_{\tilde{X}_q}\right)$ can be defined by:

$$\mathbb{C}\left(\rho_{\tilde{X}_{pq}}, \sigma_{\tilde{X}_p}, \sigma_{\tilde{X}_q}\right) =$$

$$\begin{bmatrix} \sigma_{\tilde{X}_1}\sigma_{\tilde{X}_1} & \rho\left(\tau_{x_{12}}, \tau_{y_{12}}\right)\sigma_{\tilde{X}_1}\sigma_{\tilde{X}_2} & \cdots & \rho\left(\tau_{x_{1q}}, \tau_{y_{1q}}\right)\sigma_{\tilde{X}_1}\sigma_{\tilde{X}_q} \\ \rho\left(\tau_{x_{21}}, \tau_{y_{21}}\right)\sigma_{\tilde{X}_2}\sigma_{\tilde{X}_1} & \sigma_{\tilde{X}_2}\sigma_{\tilde{X}_2} & \cdots & \rho\left(\tau_{x_{2q}}, \tau_{y_{2q}}\right)\sigma_{\tilde{X}_2}\sigma_{\tilde{X}_q} \\ \vdots & \vdots & \ddots & \vdots \\ \rho\left(\tau_{x_{p1}}, \tau_{y_{p1}}\right)\sigma_{\tilde{X}_p}\sigma_{\tilde{X}_1} & \rho\left(\tau_{x_{p2}}, \tau_{y_{p2}}\right)\sigma_{\tilde{X}_p}\sigma_{\tilde{X}_2} & \cdots & \rho\left(\tau_{x_{pq}}, \tau_{y_{pq}}\right)\sigma_{\tilde{X}_p}\sigma_{\tilde{X}_q} \end{bmatrix}, \quad (4.22)$$

where $\sigma_{\tilde{X}_p}$ and $\sigma_{\tilde{X}_q}$ are the standard deviation of the random variables $\tilde{X}_p$ and $\tilde{X}_q$. When the function $\rho\left(\tau_{x_{pq}}, \tau_{y_{pq}}\right)$ is equal to 1.0 for all random variables $\tilde{X}_p$ and

$\tilde{X}_q$, the mechanical properties (of the same nature) of all subdomains Ω_i that belong to the same region assume equal random values and, therefore, the properties are homogeneous within the geological layer. On the other hand, when the function $\rho\left(\tau_{x_{pq}}, \tau_{y_{pq}}\right)$ is different than 1.0, these properties assume different values in each subdomain Ω_i and, consequently, the properties are heterogeneous.

In this work, the correlation between two subdomains Ω_i from different regions (i.e., different geological layers) and the cross-correlation between random variables of different natures (random variables that represent different properties) are equal to zero. For each subdomain Ω_i^R of the reservoir region, three random variables representing Young's modulus, Poisson's ratio, and the Biot coefficient are considered. In the other subdomains Ω_i^t and in the auxiliary problem, the two random variables considered are Young's modulus and Poisson's ratio. The total number of random variables, which is equal to the number of partial derivatives in Eq. (4.19), is given by $3N_{\Omega_i^R} + 2\left(N_{\Omega_i^t} + 1\right)$.

These partial derivatives can also be calculated numerically by the finite difference method (WANG; YUN; WU, 2013). However, this mathematical approach is computationally unfeasible in problems that have many random variables. For instance, when using the centered approximation method, it is necessary to solve the deterministic problem twice to calculate each partial derivative. Applying the proposed method (called Green-FOSM) this limitation is overcome since all partial derivatives are calculated simultaneously at each interaction of the Green's function approach.

4.3.3. Numerical scheme for Green-FOSM method

The calculation sequence of the Green-FOSM method can be divided into two stages. The first stage is characterized by the geomechanical processing of the problem, in which the mean values of the nodal displacements, Eq. (4.16), and the partial derivatives of these displacements in relation to the random variables $(\tilde{X}_1, \tilde{X}_2, \ldots, \tilde{X}_N)$, Eq. (4.20) and Eq. (4.21), are calculated. In the second stage, a statistical post-processing is performed. In this post-processing, the variances of the nodal displacements, Eq. (4.19), are calculated using the partial derivatives of the first stage and the matrix $\mathbb{C}_{pq}$, Eq. (4.22). The convergence in the first stage is evaluated using Eq. (4.15) and with the mean values of the nodal displacements. In Figure 4.1 a representative scheme of the calculation process used in the Green-FOSM method is presented.

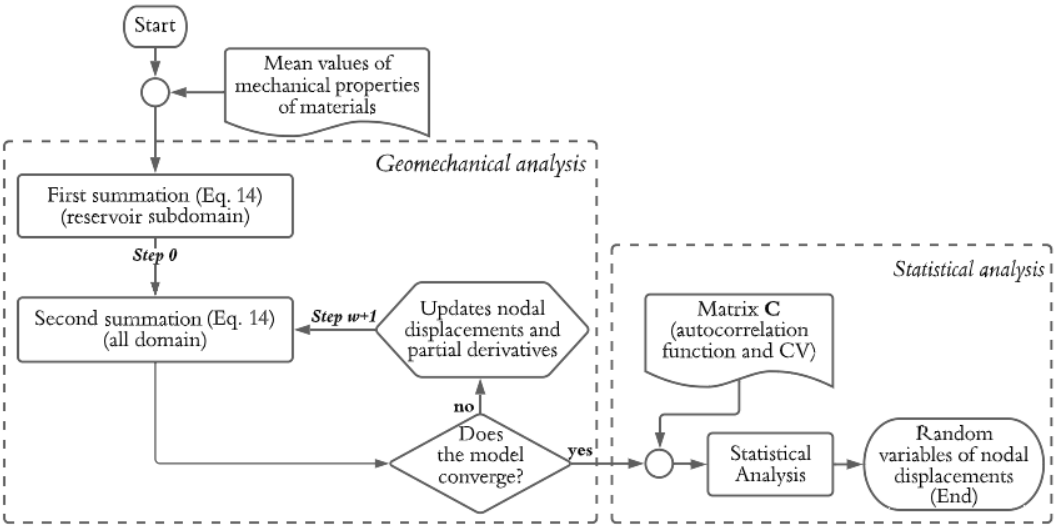

Figure 4.1. Scheme of the calculation process used in the Green-FOSM method.

Another advantage of the Green-FOSM method in relation to MCS is associated with the calculation of the nodal displacement variances. By keeping the input parameters of the geomechanical analysis (stage 1) fixed, the displacement fields of different degrees of correlation and variability can be calculated almost instantaneously, since it is not necessary to recalculate the mean values and partial derivatives.

4.4. Numerical examples

In this Section, two numerical examples are presented to demonstrate the validity of the proposed methodology. These examples use the 2D model (plane strain condition) shown in Figure 4.2, which represents a geological formation composed of four layers of rocks with different mechanical properties. The reservoir is bounded by two straight faults that form a tilted block system. In the first example, the reservoir is subjected to a uniform fluid depletion process, shown in Figure 4.2.b, and in the second example, shown in Figure 4.2.c, the reservoir is subjected to a combined fluid depletion and injection process.

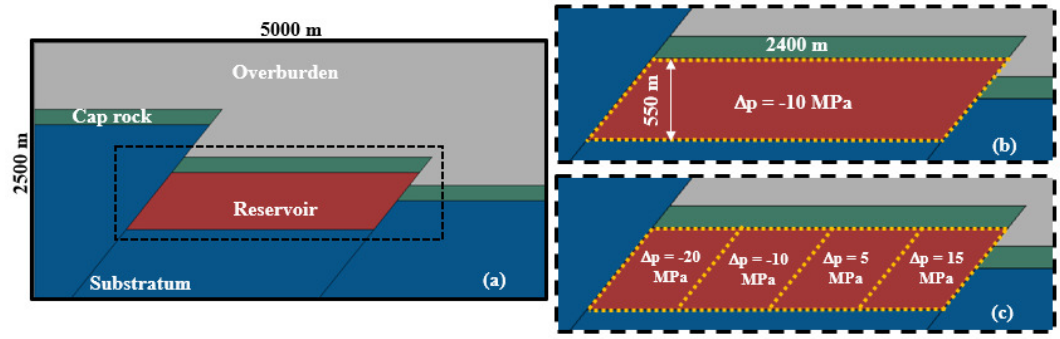

Figure 4.2. (a) 2D model used to simulate geological formation, (b) reservoir under uniform depletion, and (c) reservoir under depletion and injection.

In both examples, the uncertainties related to the mechanical properties of the materials (Young's modulus, Poisson's ratio, and Biot coefficient) are propagated to the nodal displacements using MCS and the Green-FOSM method. Despite being computationally expensive, MCS is adopted to generate the reference solutions used to validate the proposed method. As mentioned in Section 4.3.1, to perform the MCS it is necessary to know the probability density function $f_{\tilde{X}_i}(\tau)$ of the random variables $\tilde{X}_i$ that represent the mechanical properties of materials. Thus, the random variables that represent the Young's modulus and the Poisson's ratio are described using a normal distribution function, as in the works by Plúa et al. (2021a), Plúa et al. (2021b), and Jha et al. (2015). The random variables referring to the Biot coefficient are represented by a uniform distribution function (PLÚA et al., 2021a, 2021b). The set of mechanical and numerical parameters used in this section are presented in Table 4.1.

Table 4.1. Parameters for the tilted block reservoir problem presented in Section 4.4.

Mechanical Parameters						
	Young's modulus [GPa]		Poisson's ratio		Biot coefficient	
Layer	Mean	CV	Mean	CV	Mean	CV
Reservoir	10.0	10% - 20%	0.20	10% - 20%	0.80	10%
Cap rock	8.0	10% - 20%	0.20	10% - 20%	-	-
Overburden	5.0	10% - 20%	0.20	10% - 20%	-	-
Substratum	15.0	10% - 20%	0.20	10% - 20%	-	-
Inf. domain	10.0	10% - 20%	0.20	10% - 20%	-	-
Numerical Parameters						
Definition					Values	
Tolerance in the displacement field					10^{-4}	
Gauss quadrature (non-singular point)					4×4	
Bartholomew level for quadrature (singular point)					3	
Gauss quadrature after Duffy's transformation (singular point)					3×3	

4.4.1. Reservoir under uniform depletion with fully correlated or fully uncorrelated random variables

In this example, the problem domain is divided into 397 sub-regions, which form the triangular element mesh for the geomechanical analysis and the stochastic grid for the statistical analysis (Figure 4.3). This stochastic grid results in 876 random variables. The displacement fields are constructed by evaluating the horizontal and vertical displacements obtained at 254 nodal points.

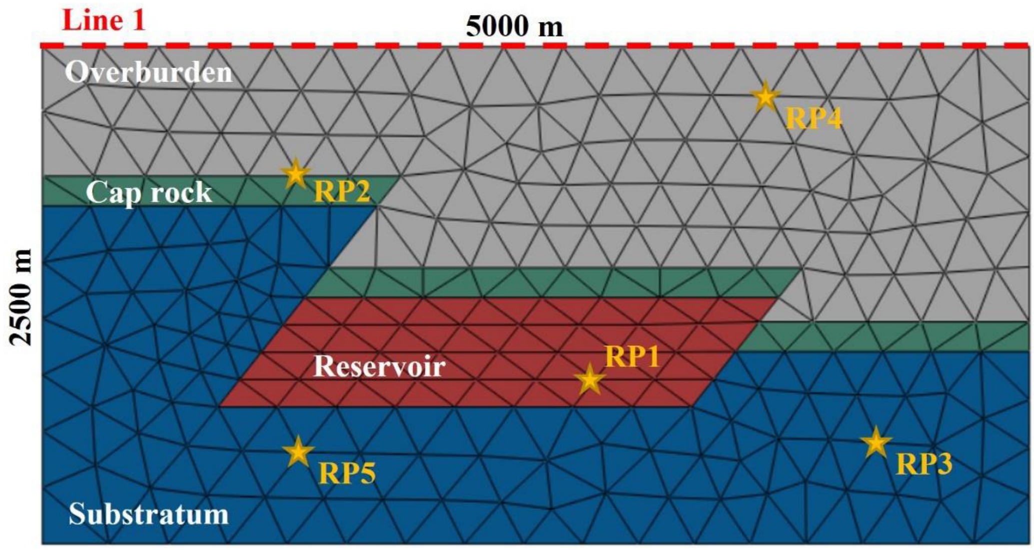

Figure 4.3. Mesh of triangular elements used in geomechanical analysis and stochastic grid of statistical analysis of the example subjected to a uniform fluid depletion process.

In order to evaluate the effectiveness of the Green-FOSM method in relation to the spatial variability of the mechanical properties of materials, the example presented in this section is analyzed assuming two limit cases. In the first case, random variables from different subdomains Ω_i are fully correlated, $\rho\left(\tau_{x_{pq}}, \tau_{y_{pq}}\right)$ equal to 1.0, and in the second, they are fully uncorrelated, $\rho\left(\tau_{x_{pq}}, \tau_{y_{pq}}\right)$ equal to 0.0. As discussed in Section 4.3.2, in the first case the mechanical properties are homogeneous and in the second they are heterogeneous. For the fully correlated and uncorrelated cases, two coefficients of variation (CV) for the Young's modulus and for the Poisson's ratio are considered, 10% and 20%. For the Biot coefficient, the CV is taken as 10% in all analyses, since coefficients of variation above 10% can result in Biot coefficients greater than 1.0, which have no real physical meaning. The results obtained through Green-FOSM method are compared to the results obtained using MCS. In the simulations performed with the MCS, the statistical moments of the displacements are determined after 3000 repetitions of the deterministic Green's function approach. This number was defined after observing that the average difference between the results obtained by two MCS, performed for the same problem, is less than 3%, as can be seen in Figure 4.4.

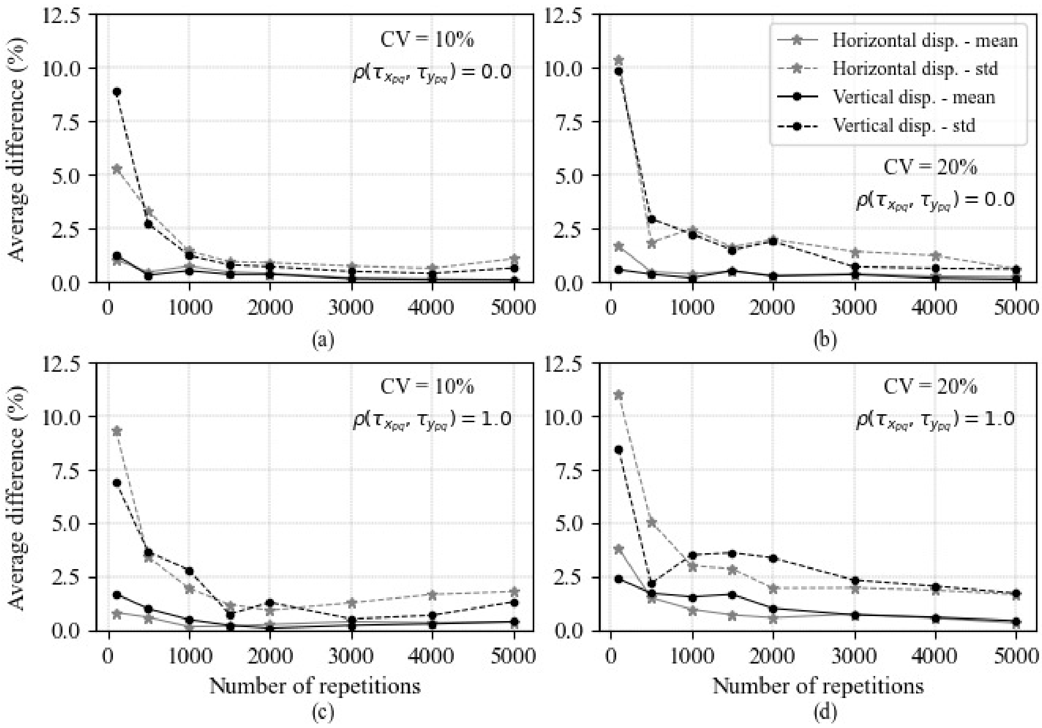

Figure 4.4. Average difference between the results obtained by two MCS.

4.4.1.1. Moments and statistical response

Using the geological profile presented in Figure 4.2, the effect of the uncertainties associated with the mechanical parameters of rocks on the displacement field generated by a uniform depletion process is analyzed. In Figure 4.5 the frequency histograms constructed from the vertical displacements of the reference point 1 (indicated in Figure 4.3) are presented. The curves in black represent normal probability density functions calculated from mean values and variances found via MCS. The curves in red describe the distribution functions fitted using the statistical parameters obtained by the Green-FOSM method.

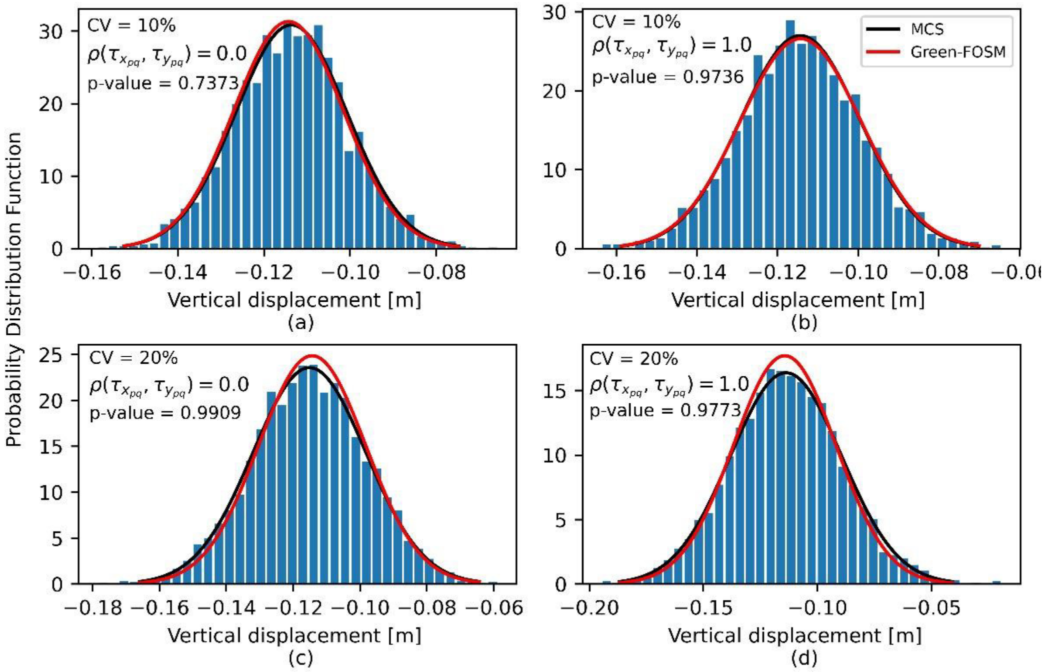

Figure 4.5. Frequency histograms and probability density function of the random variable representing the vertical displacement of the reference point 1.

These histograms show that the vertical displacement random variable follows a bell shape and thus can be adequately represented by a normal distribution function. The Kolmogorov-Smirnov normality test ("Kolmogorov–Smirnov Test", 2008) is used to verify this quantitatively. Applying this test, it is observed that for all evaluated reference points the p-value is not lower than the 5% limit (assuming a confidence interval equal to 95%) and, therefore, the null hypothesis (the probability distribution function follows the format of the normal distribution function) should not be rejected. This format can be justified by the central limit theorem, in which the statistical answer given by the sum of several individual contributions follows a normal probability distribution. As shown in Eq. (4.14), the statistical response of the nodal displacements (output random variables) is obtained from the sum of several random variables that represent the individual displacements calculated in each triangular element of the geomechanical mesh, which justifies the bell shape of the histograms. In all cases, it is observed that the probability distribution curves adjusted from the statistical moments (mean value and variance) calculated using the Green-FOSM method are similar to the curves obtained via the MCS. When analyzing the other nodes and horizontal displacements (see other reference points in Appendix C), it is noted that the other random variables have similar behavior.

An overview of the results obtained through the proposed method and via MCS is shown in Figure 4.6, which presents the relationships between the statistical parameters calculated by the two methods for each node. In the analyses with CV equal to 10%, the statistical parameters calculated by the proposed method are close to the values found via MCS, with the greatest difference being equal to 4.4%. For the CV equal to 20%, the statistical parameters present greater dispersion. In most of the nodes analyzed, the mean values obtained via Green-FOSM are close to those found using MCS. However, for some nodes (located between nodes 1 and 50), it is noted that the average values of vertical displacements found by the proposed method are between 10.6% and 13.7% higher than the values found using MCS. This difference is justified by the magnitude of the vertical displacements in these nodes, which are close to zero, and can be reduced by increasing the number of repetitions in MCS. On the other hand, for the fully correlated situation, the variances obtained by the proposed method are, on average, 6.2% (horizontal displacement) and 7.2% (vertical displacement) smaller than the variances found via MCS. For the totally uncorrelated situation these values are 1.1% (horizontal displacement) and 1.3% (vertical displacement).

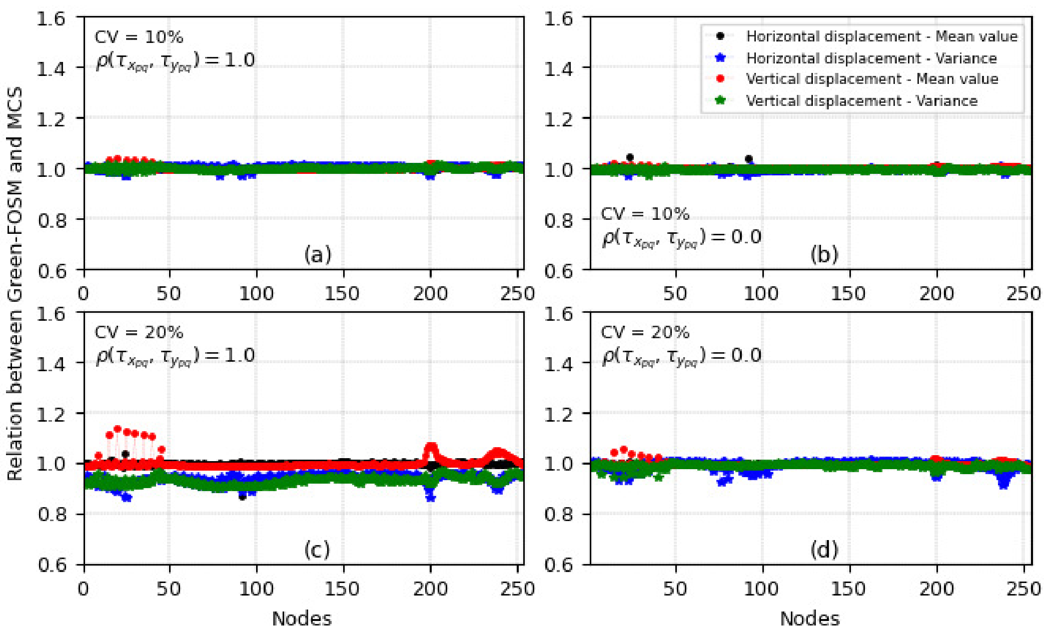

Figure 4.6. Relationship between the statistical moments obtained by Green-FOSM method and by MCS.

As mentioned by Bungenstab and Bicalho (2016), due to the truncation of the Taylor series, the FOSM method tends to underestimate the values of the variances when the CV of the input random variables increases. Despite this limitation, for the situations of variability and CV levels analyzed, the difference between the values obtained by the proposed method and by MCS are small when compared to the dimensions of the geomechanical problems. Therefore, it can be said that for typical geomechanical problems, the Green-FOSM method is able to provide results comparable to those found by MCS.

4.4.1.2. Displacement fields considering the uncertainties

Figure 4.7 shows the vertical displacement fields found after the depletion process for the fully correlated case with CV equal to 10%. These displacement fields are created assuming that the output random variables are described by normal probability density functions. The lower and upper limits are shown in Figure 4.7.a and represent the extreme values of the interval with a confidence level equal to 95%.

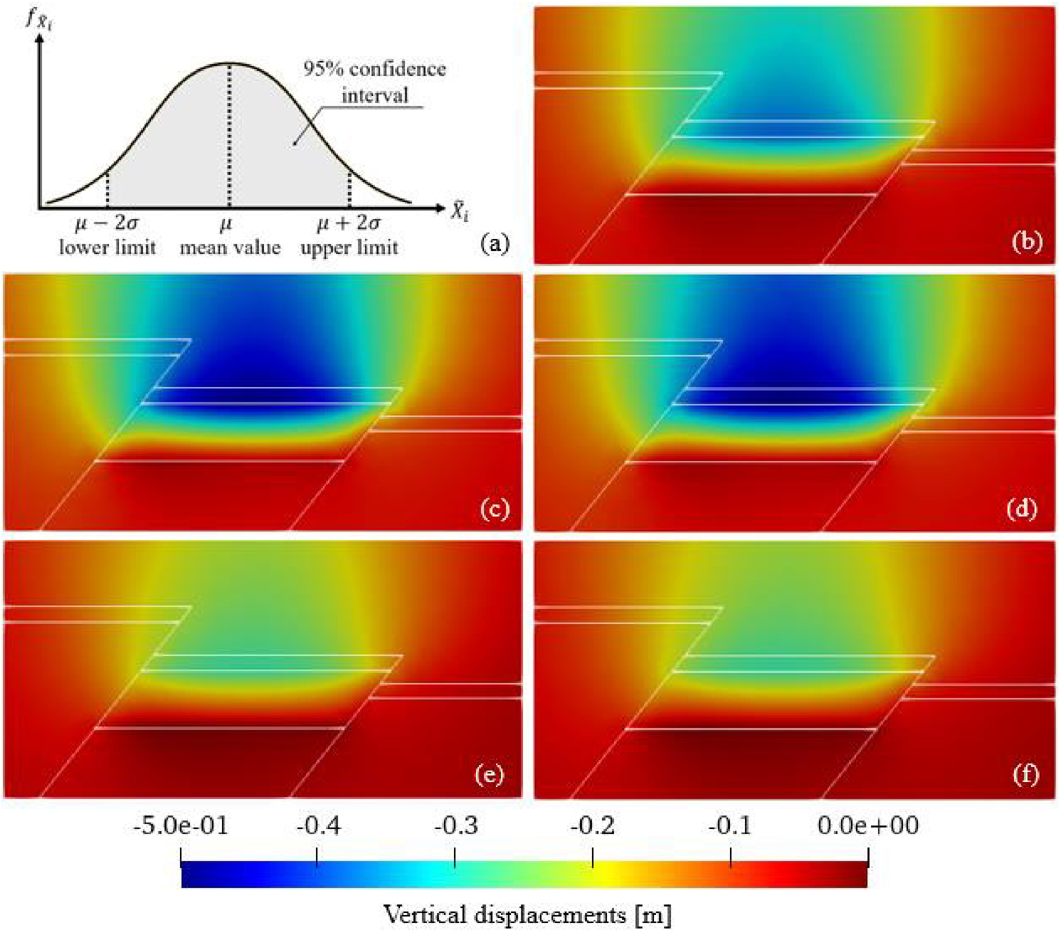

Figure 4.7. Effect of uncertainties associated with the mechanical properties of materials under the displacement field generated by a uniform depletion process. (a) Lower and upper limits for 95% confidence interval, (b) Deterministic results (mean values), (c) Green-

FOSM lower limit results, (d) MCS lower limit results, (e) Green-FOSM upper limit results, and (f) MCS upper limit results.

These results demonstrate the importance of considering the effect of uncertainties associated with the mechanical properties of materials in the calculation of displacement generated by a change in pore pressure. In the deterministic analysis (shown in Figure 4.7.b) the maximum free surface subsidence is approximately 0.3 meters. However, due to uncertainties this displacement can be up to 27% higher (Figure 4.7.c and Figure 4.7.d) or lower (Figure 4.7.e and Figure 4.7.f). Comparing the vertical displacement fields found by the Green-FOSM method and by the MCS, it can be observed that the two methods found similar results.

The horizontal and vertical displacements found along Line 1 (shown in Figure 4.3) considering all analyzed cases are presented in Figure 4.8.a and Figure 4.8.c present the results for the totally correlated case and Figure 4.8.b and Figure 4.8.d for the totally uncorrelated case. Regions between two curves of the same color represent 95% confidence response intervals. The deterministic answer of the problem calculated using the Green's function approach and the FEM are described by black solid and dashed curves, respectively.

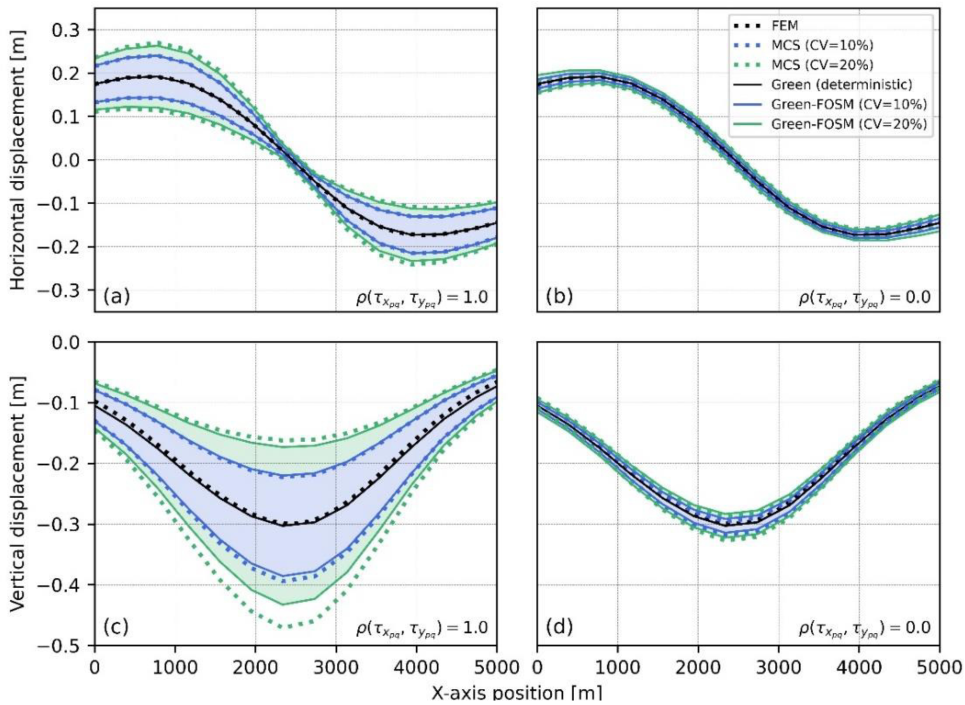

Figure 4.8. Horizontal and vertical displacements along Line 1 obtained after the uniform depletion process. Graphs (a) and (c) present the results for the totally correlated case and graphs (b) and (d) for the totally uncorrelated case.

These results indicate that the effect of spatial variability of mechanical properties is greater when the random variables that represent these properties are totally correlated. On the other hand, when the random variables are totally uncorrelated the statistical answer of the problem approaches the deterministic answer. In this situation, each subdomain Ω_i assumes different random values, which fluctuate around their mean values. These values generate small parcels of displacements, which also vary around the mean values. Thus, when performing the sum of these parcels, the positive variations are canceled out by the negative variations, and the final displacement approaches the mean displacement (deterministic result). In the totally correlated case the subdomain Ω_i assumes equal random values and consequently, this does not occur. The maximum difference among the results with CV=10% is equal to 2.25% and occurs between the curves that represent the lower limit of the vertical displacement (Figure 4.8.c). The results for CV=20% follow the same behavior, however, the difference between these curves is 8.85%. In general, the difference between the results found by the two methods increases when the CV of the mechanical properties increases. This happens because the FOSM method tends to underestimate the values of the variances when the CV of the input random variables increases, due to the truncation of the Taylor series. Despite this, for the levels of correlation and variability analyzed, the Green-FOSM method is able to obtain results close to those achieved by MCS.

4.4.1.3.
CPU time comparison

Figure 4.9 shows the relationship between the CPU time of the MCS (with 3000 repetitions) and the CPU time taken by the Green-FOSM method as a function of the number of random variables considered in the problem. Except for the model that has 836 random variables (Figure 4.3) whose results are discussed in this section, the CPU times of the MCS are estimated using the average time obtained by a set of 50 samples. These CPU times are obtained using a workstation with an Intel Core i9-10850K processor and 64 Gb of RAM.

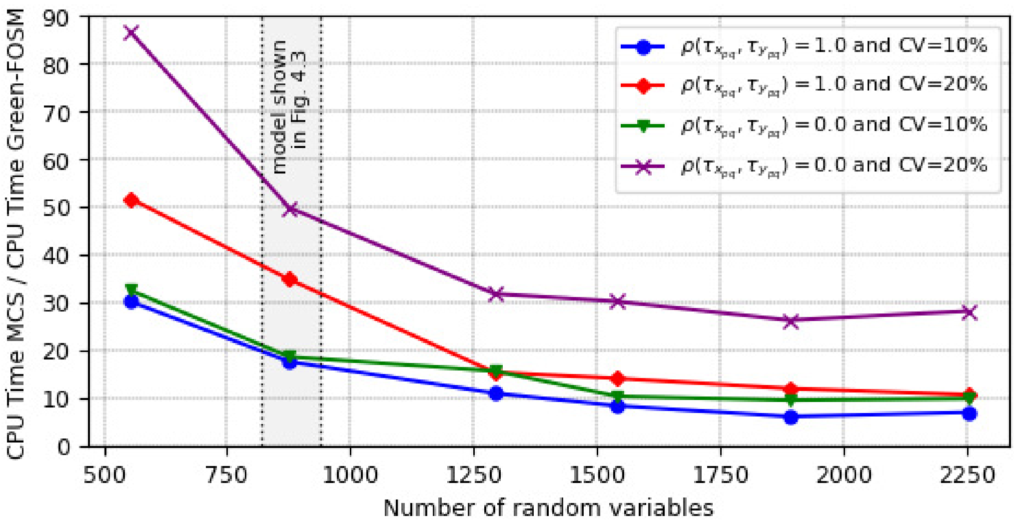

Figure 4.9. Relation between the CPU times needed to perform 3000 repetitions via MCS and the CPU times of the Green-FOSM method.

The relationships between CPU times (Figure 4.9) vary with different degrees of correlation and variability. This occurs because, the greater is the variability of mechanical properties, the greater is the number of iterations necessary for the convergence of the analyses via MCS. In the Green-FOSM method, this variability does not affect the CPU time. As discussed in Section 4.3.3, in this method the partial derivatives are calculated from the mean values in the geomechanical analysis and the uncertainties are introduced after this in the post-processing step, whose processing is almost instantaneous. As can be seen in Figure 4.9, the relationships between CPU times converge to a fixed value when the number of random variables increases. In the most disadvantageous situation, the Green-FOSM method is approximately seven times faster than the MCS.

For the proposed levels of correlation and variability, the results presented in this section demonstrate that the Green-FOSM method can propagate the uncertainties associated with the mechanical properties of materials to the displacement field generated by a uniform fluid depletion process consuming less computational effort than the MCS.

4.4.2.
Reservoir under non-uniform depletion with spatially correlated random variables

In this section, the geological profile used in the previous example is analyzed considering the fluid depletion and injection process presented in Figure

4.2.c. In this example, the geomechanical mesh is decoupled from the stochastic grid. Thus, the geomechanical problem domain (Ω_t) is divided into 1812 sub-regions and 960 nodes, which form the mesh of triangular elements shown in Figure 4.10.a. The stochastic grid is divided into 397 sub-regions (Figure 4.10.b), which result in 876 random variables.

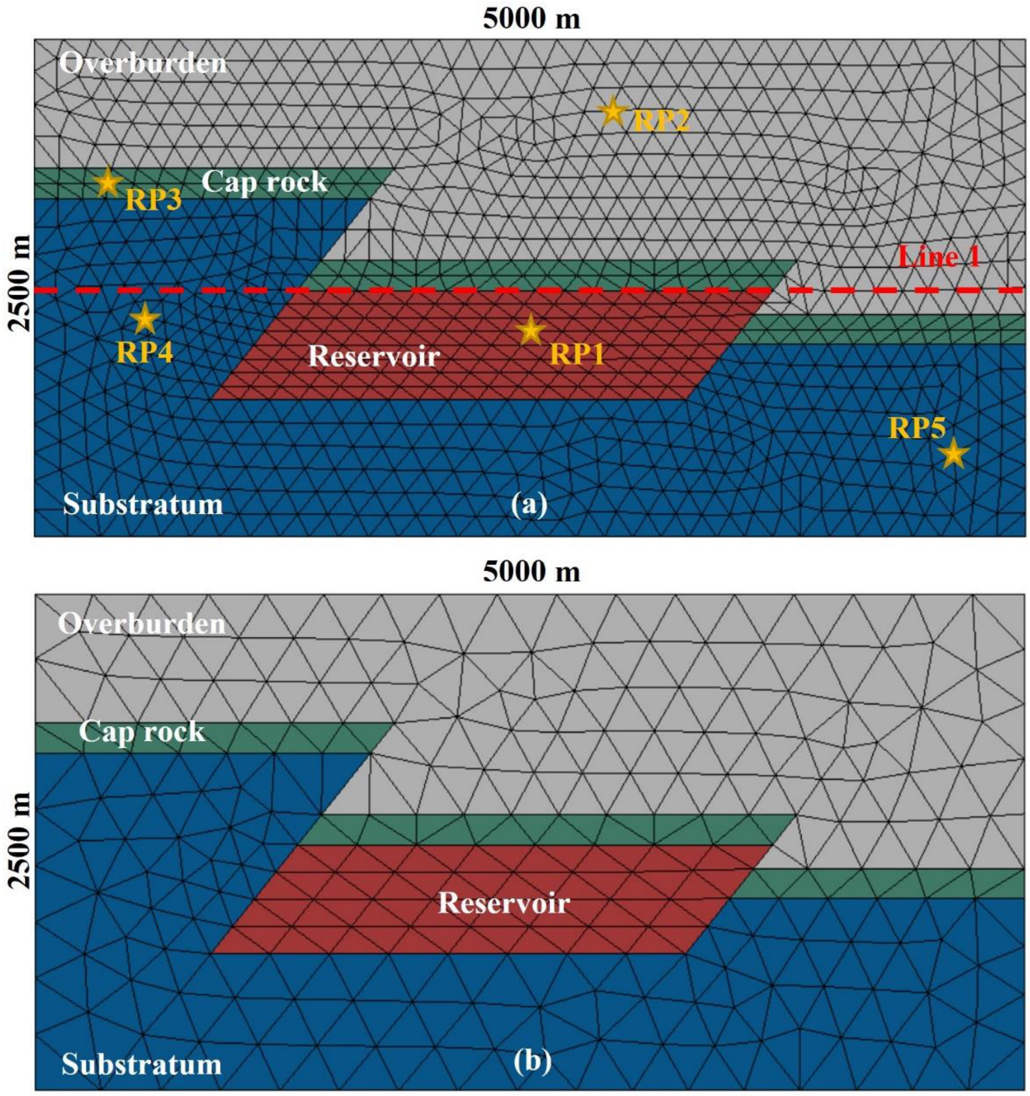

Figure 4.10. (a) Mesh of triangular elements used in geomechanical analysis and (b) stochastic grid of statistical analysis of the example subjected to a non-uniform fluid process.

In order to evaluate the effectiveness of the proposed method relative to the spatial variability of the mechanical properties of materials, this example is analyzed assuming that the spatial variability of these properties is defined by the exponential autocorrelation function (WANG et al., 2020; WU et al., 2021) shown in the following

$$\rho\left(\tau_{x_{pq}}, \tau_{y_{pq}}\right) = \exp\left(-\frac{\tau_{x_{pq}}}{l_h} - \frac{\tau_{y_{pq}}}{l_x}\right), \tag{4.23}$$

where $\tau_{x_{pq}}$ and $\tau_{y_{pq}}$ are the absolute distances between the centroids of the subdomains Ω_p and Ω_q in the horizontal and vertical direction, respectively, and l_h and l_v are the horizontal and vertical autocorrelation distances, respectively. For the horizontal autocorrelation distance (l_h) the value of 1000 meters is admitted and for the vertical autocorrelation distance (l_v) the value of 200 meters is used.

As in the previous section, the results obtained via MCS are used as a reference as the statistical response. Thus, when performing MCS, the random values if the variables that represent the Young's modulus and Poisson's ratio, which are defined by a normal probability distribution function, are generated using the Cholesky decomposition technique, as performed by Li et al. (2015) and Yang et al. (2022). The random values that represent the Biot coefficient, which are defined by a uniform probability distribution function, are assumed to be fully correlated. The CVs of the random variables that represent Young's modulus and Poisson's ratio are simultaneously equal to 10% or 20%. For the Biot coefficient, the CV is taken as 10% in all analyses.

4.4.2.1. Moments and statistical response

In Figure 4.11 the frequency histograms constructed from the vertical displacements of the reference point 1 (RF1 indicated in Figure 4.10.a) are presented. The curves in black represent normal probability density functions calculated from mean values and variances found via MCS. The curves in red describe the distribution functions fitted using the mean value and standard deviation obtained by the Green-FOSM method. As in the previous section, the histograms show that the vertical displacement random variable follows a bell shape curve and, therefore, it can be adequately represented by a normal distribution function. This visual verification is confirmed quantitatively by the Kolmogorov-Smirnov test ("Kolmogorov–Smirnov Test", 2008), assuming a confidence level of 95%. When analyzing the other nodes and horizontal displacements (see other reference points in Appendix C), it is noted that the other random variables present similar behavior.

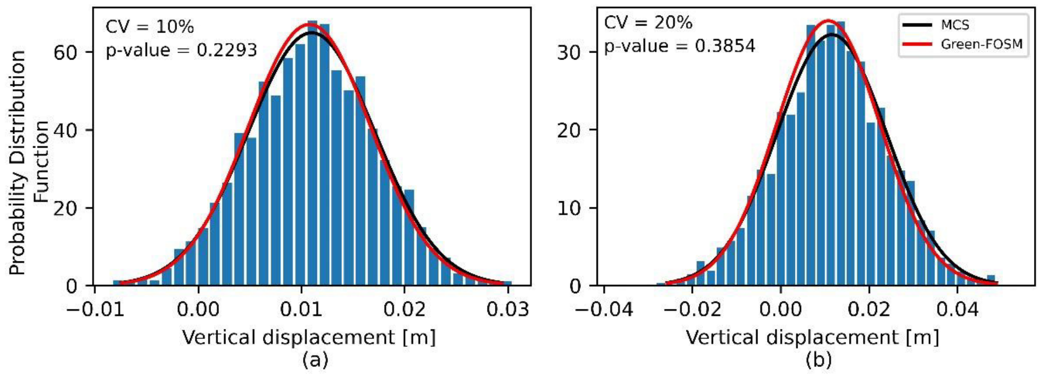

Figure 4.11. Frequency histograms and probability density function of the random variable representing the vertical displacement of the reference point 1.

Figure 4.12 present the relationship between the statistical parameters (mean value and variance) calculated by the Green-FOSM method and by MCS. For the two values of CV analyzed, it is observed that for some nodes the relationships between the mean values of the vertical displacements vary by up to 20%. This difference is justified by the magnitude of the vertical displacements in these nodes, which are close to zero. It can be reduced by increasing the number of repetitions in MCS. In general, the results obtained for CV=20% present a greater dispersion when compared to the results of the analysis with CV=10%. In this case, the average differences between the variances are 5.2% and 7.9% for the horizontal and vertical displacements, respectively. Again, the main limitation of the proposed method is that it tends to underestimate the variances when the CV of the input random variables increases, as can be seen in this example.

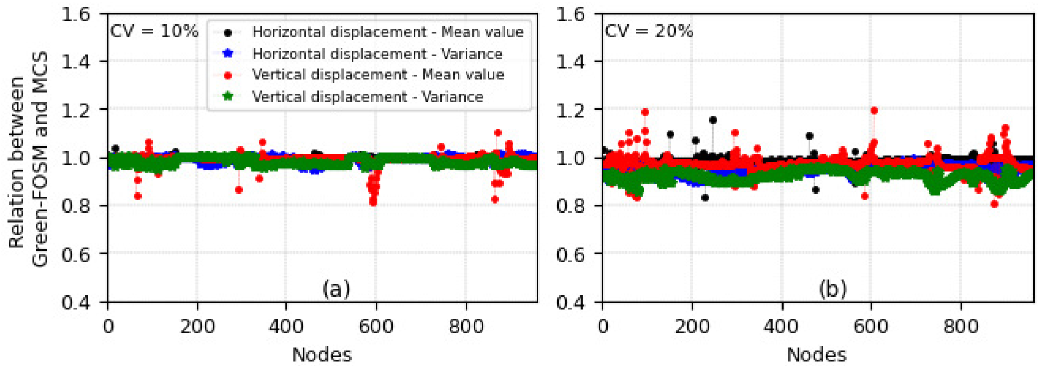

Figure 4.12. Relationship between the statistical moments obtained by Green-FOSM method and by MCS.

4.4.2.2. Displacement fields considering the uncertainties

Figure 4.13 shows the vertical displacement fields found after this process considering CV equal to 10%. These results are obtained considering that the output random variables are described by normal distribution functions. The lower and upper limits shown in Figure 4.13.a represent the extreme values of the interval with a confidence level equal to 95%.

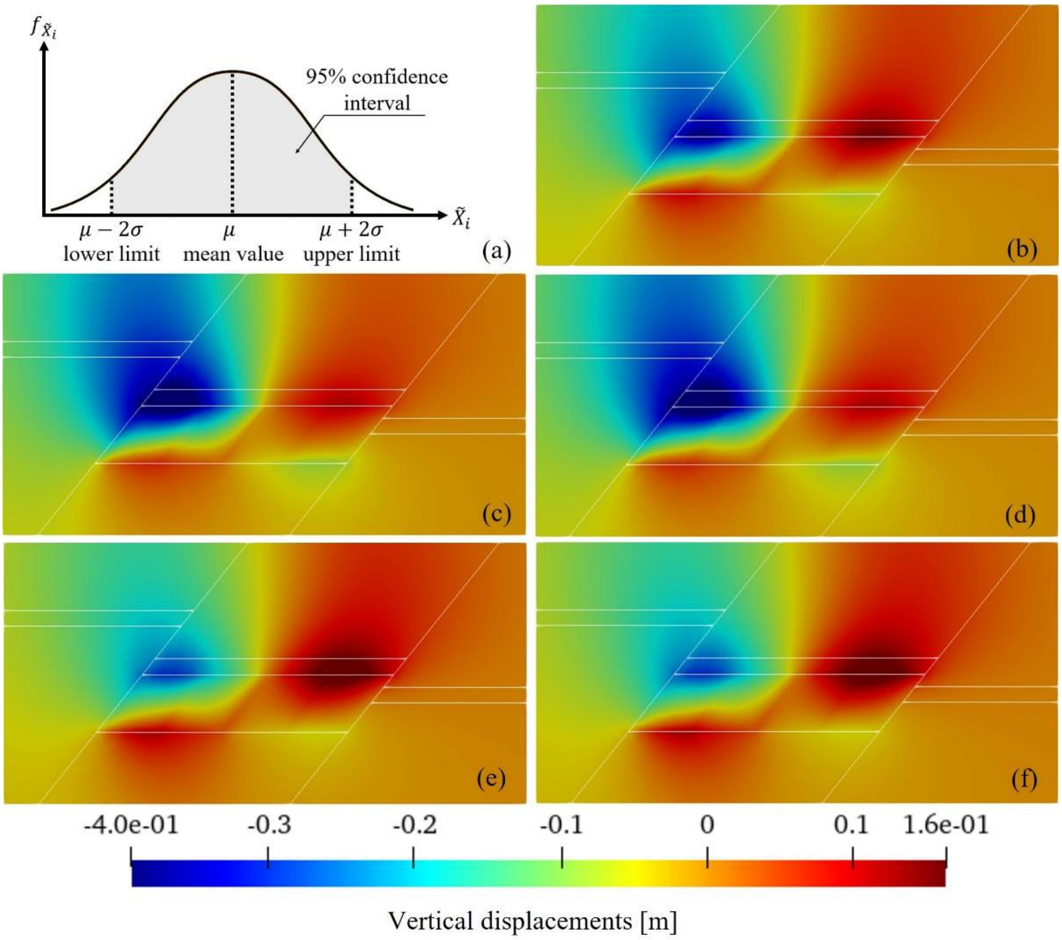

Figure 4.13. Effect of the uncertainties associated with the mechanical properties of materials under the displacement field generated by a fluid depletion and injection process. (a) Lower and upper limits for 95% confidence interval, (b) Deterministic results (mean values), (c) Green-FOSM lower limit results, (d) MCS lower limit results, (e) Green-FOSM upper limit results, and (f) MCS upper limit results.

The obtained displacement fields show that non-uniform pore pressure variations within the reservoir cause both swelling and compaction of the geological formation. As a result, analyzing the lower limit (Figure 4.13.c and Figure 4.13.d) it is observed the growth of the compacted and the decrease of the swollen region. For the upper limit case (Figure 4.13.e and Figure 4.13.f) the inverse behavior is observed. These results reaffirm the importance of considering the effect of uncertainties related to the mechanical properties of materials in the calculation of displacements generated by changes in pore pressure. As in the previous example, the vertical displacement fields obtained by the Green-FOSM method and by the MCS are similar.

Figure 4.14 presents the horizontal and vertical displacements found along the upper edge of the reservoir (Line 1 shown in Figure 4.10.a) considering all analyzed cases. Regions between two curves of the same color represent 95% confidence response intervals. The deterministic answer of the problem calculated using the Green's function approach and the FEM are described by black solid and dashed curves, respectively.

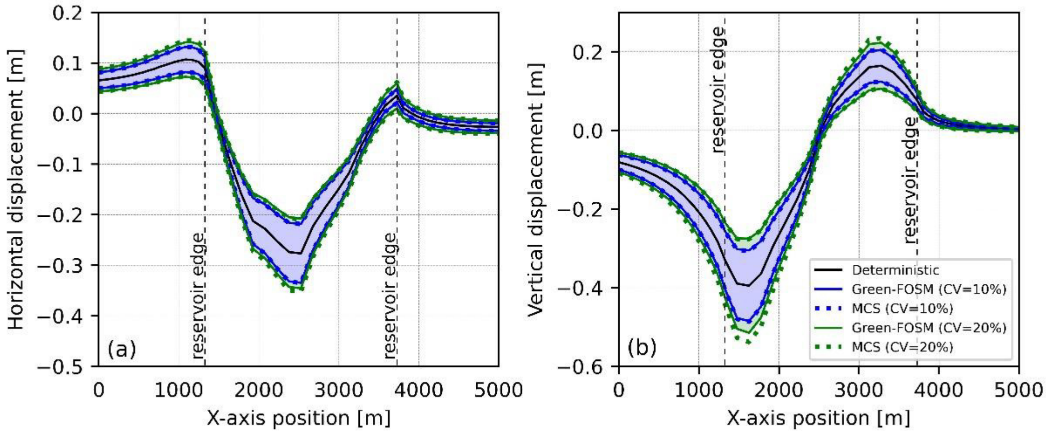

Figure 4.14. Horizontal and vertical displacements along the upper edge of the reservoir (Line 1 shown in Figure 4.10.a) obtained after the fluid depletion and injection process. Graphs (a) and (c) present the results for the totally correlated case and graphs (b) and the totally uncorrelated case.

Again, the results show that the effect of spatial variability of mechanical properties is greater when random variables are totally correlated. For the levels of correlation and variability analyzed, the displacements found through the Green-FOSM method and via MCS have similar behavior. Among these results, the maximum difference found is 2.4%, given by the curves that represent the vertical displacement (Figure 4.14.b). Therefore, for the proposed correlation and variability levels, the results presented in this section demonstrate that the Green-FOSM method can propagate the uncertainties associated with the mechanical properties of materials to the displacement field generated by a combined fluid depletion and injection process.

4.5.
Conclusions and remarks

The present work proposes a computationally efficient stochastic statistical method (Green-FOSM) that considers uncertainties in geomechanical problems, with the objective of improving the decision-making process related to problems associated with production of oil and gas, the extraction of water, and the storage of CO_2 or natural gas, such as swelling or compaction of the reservoir rock, subsidence of the free surface, decreased production, fault reactivation, seismic events, and others. The novelty of the method lies in the use of the Green's function approach (GFA), which, together with the FOSM method, is used to propagate uncertainties associated with the mechanical properties of material to the displacement field of the geological formation. Furthermore, using the concepts of stochastic grid and autocorrelation function, the proposed method allows the consideration of the spatial variability of random variables that represent these mechanical properties.

The GFA uses the fundamental solutions of classical mechanics (Kelvin fundamental solution, Melan fundamental solution, among others) and the reciprocity theorem to calculate the displacement field of a geological formation with irregular geometry, and different types of materials. The great advantage of this method compared to the classical FEM is that it does not require the imposition of boundary conditions and the problem analysis can be performed considering only the reservoir or other regions of interest. In general, when analyzing a geomechanical model using the FEM, it is necessary to discretize a large region around the domain of interest (semi-infinite media) to represent the continuity of the geological profile and, at the same time, reduce the effect of boundary condition in this domain. This modeling strategy increases the degrees of freedom of the model and the CPU time of the deterministic analysis. In GFA, the discretization of the semi-infinite media is not necessary, consequently, the degrees of freedom of the geomechanical model and the CPU time of the deterministic analyzes are smaller.

As GFA demands less computational effort, this approach becomes ideal for propagating the uncertainties associated with production of oil and gas, the extraction of water, and the storage of CO_2 or natural gas. In this work, the GFA is formulated to be used with the FOSM statistical method. This statistical method is adopted because it is applicable to the range of variability of the mechanical properties of the rocks that form geological profiles and because it is capable of quickly obtaining the statistical answer to the problem. In addition, using GFA it is possible to directly calculate the partial derivatives used in FOSM, Eq. (4.17). These partial derivatives can also be calculated numerically by the finite difference method. However, this mathematical approach is computationally unfeasible in problems that have many random variables. For instance, when using the centered approximation method, it is necessary to solve the deterministic problem twice to calculate each random variable.

The validity of the Green-FOSM method is analyzed by comparing the statistical parameters (mean values and variances) obtained by the proposed method with the statistical parameters found via MCS. For this, two numerical examples are presented. In the first example, the mesh of elements of the geomechanical analysis and the stochastic grid are the same, the reservoir region is subjected to a uniform depletion process, and the random variables that represent the mechanical properties are considered fully correlated or fully non-correlated. In the second example, the mesh of the geomechanical problem and the stochastic grid are decoupled, the reservoir region is subjected to a non-uniform depletion process and the random variables that represent the mechanical properties are spatially correlated using an exponential autocorrelation function. In both example, two coefficients of variation (CV) for the Young's modulus and for the Poisson's ratio are considered, 10% and 20%. For the Biot coefficient, the CV is taken as 10% in all examples. The results obtained show that, in both examples, the first two statistical moments obtained using Green-FOSM method and by MCS are similar. The largest differences between the mean values are found when CV is equal to 20%. For the variances, it is observed that, due to the truncation of the Taylor series, the FOSM method tends to underestimate the values of the variances when the CV of the input random variables increases. Despite this limitation, for the situations of variability and CV levels analyzed, the difference between the values obtained by the proposed method and by MCS are small when compared to the dimensions of the geomechanical problems.

In general, the displacement fields found by the Green-FOSM method agree well with the statistical results obtained via Monte Carlo simulation, which confirms the validity of the proposed method. Comparing the displacement fields obtained through statistical analysis with the displacement fields calculated deterministically, it is possible to observe a large difference between them, which highlights the importance of considering the effect of uncertainties associated with the spatial variability of the mechanical properties of rocks in the calculation of displacement generated by variations in the pore pressure of the reservoir rock. The relationships between the CPU times show that the proposed method is computationally significantly more efficient than Monte Carlo simulation (considering 1500 random variables it can be 30 times faster). The different levels of correlation and variability show that the effect of spatial variability of mechanical properties is greater when the random variables that represent these properties are totally correlated. On the other hand, when these variables are totally uncorrelated, the statistical response approaches the deterministic response. Therefore, the Green-FOSM method achieves all the proposed objectives, since because its simplicity and efficiency it is capable of assisting reservoir engineers in decision-making process when evaluating problems related to the injection or depletion of fluids in underground reservoirs.

5
"Non-iterative Green's function approach for unbounded heterogeneous fluid-saturated media"

Paper submitted by Leonardo C. Mesquita, Elisa D. Sotelino, Matheus L. Peres, and Yves M. Leroy in the International Journal for Numerical and Analytical Methods in Geomechanics (under review).

Abstract

The Green's function approach (GFA) developed in previous work uses the classical Green's function for point load (Kelvin's fundamental solution, Melan's fundamental solution, and others) and the reciprocity theorem to capture changes in the displacement, strain, and stress fields of a geological formation subjected to the processes of extraction or injection of fluids. The great advantage of this method compared to the classical FEM is that it does not require the imposition of boundary conditions and the problem analysis can be performed considering only the reservoir or other regions of interest. In the original version of the GFA, the displacement field is calculated using an iterative numerical scheme, which decreases the computational performance of the method and may present convergence problems. Such limitations have made it difficult to use the GFA in real problems. The present work proposes a non-iterative numerical scheme capable of expanding the applicability of GFA and, simultaneously, improving its computational performance. The results presented in this work demonstrate that using this numerical scheme, the GFA consumes up to 17,5 times less CPU time compared to iterative scheme and this relationship can be even greater if the heterogeneity of the material increases. Using a geological profile constructed from seismic images of the Brazilian pre-salt (Tupi field located in the Santos basin), it is shown that the non-iterative GFA allows the analysis of complex geological formations.

5.1. Introduction

The activities associated with the processes of fluid injection or extraction in underground reservoirs, such as the production and storage of oil and gas (YANG et al., 2015), the extraction of water (GALLOWAY; BURBEY, 2011; SHEN; XU, 2011), and the sequestration of CO_2 (BACHU, 2008; KALAM et al., 2020), generate variations in the displacement, strain, and stress fields of the geological profile. As a direct consequence of these activities, the swelling or compaction of the geological formation occurs, which can lead to the subsidence or uplift of the free surface (BAÙ et al., 2015), wellbore collapse (MINKOFF; KRIDLER, 2006), fault reactivation (BUIJZE et al., 2017), seismic events (BOURNE et al., 2014; VERDON et al., 2016), and a decrease in production (XIONG et al., 2018). These problems have motivated the development of analytical and numerical methods that allow predicting the impact of these activities on the rock mass state.

Among the analytical methods, one of the most used for these applications is the method proposed by Geertsma (GEERTSMA, 1957, 1973b, 1973c), which is based on the nucleus-of-strain principle introduced by Mindlin and Cheng (1950). Through this method, it is possible to predict the subsidence generated by the uniform depletion of a cylindrical-shaped reservoir embedded in a semi-infinite homogeneous elastic medium. In order to make this method more comprehensive, over the last few years, several researchers have incorporated new concepts into Geertsma's method. Van Opstal (1975) introduced the concept of the rigid base in the calculation of subsidence. Tampone et al. (2010) improved Van Opstal's method to obtain the displacement and strain fields of the geological profile. Segall (1992) developed a formulation to analyze strains and stresses in axisymmetric reservoirs. In general, the analytical methods have the advantage of being simple, however, they are limited in terms of the geometry and heterogeneity of the geological formation and the mechanical behavior of the materials that they can consider.

Numerical methods are more comprehensive, as they can consider the particularities of each geological formation. In addition, they allow the coupling of flow analysis to geomechanical simulation (DEAN et al., 2006; RUTQVIST, 2011). The majority of numerical analyzes are performed using the finite element method

(FEM), which is capable of considering different types of nonlinearity, such as plasticity (KOSLOFF; SCOTT; SCRANTON, 1980; NIU; LI; WEI, 2017), viscosity (CHANG; MAILMAN; ZOBACK, 2014; VOYIADJIS; ZHOU, 2018), fracturing (WANGEN, 2013), and fault reactivation (HADDAD; EICHHUBL, 2020; LESUEUR; POULET; VEVEAKIS, 2020). Despite these qualities, in most cases, the simulations demand a high computational effort for the construction and processing of models. Furthermore, in the FEM, it is difficult to represent the boundary conditions of the semi-infinite environment in which the geological formation is embedded.

The Green's function approach (GFA) proposed by Peres et al. (2021), uses the classical Green's functions for point load as an auxiliary solution that together with the reciprocity theorem to capture the variation in the stress state of a geological formation subjected to processes of injection or extraction of fluids. This approach has no limitations in terms of geometry, number of layers, and heterogeneity of the geological profile and can be applied to materials with linear or non-linear behavior. Compared to the classical FEM, the great advantage of the GFA is that it does not require the imposition of boundary conditions and the problem analysis can be performed considering only the reservoir or other regions of interest. In general, when analyzing a geomechanical model using the FEM, it is necessary to discretize a large region around the domain of interest (semi-infinite media) to represent the continuity of the geological profile and, at the same time, reduce the effect of boundary condition in this domain.

The GFA can also be classified as an analysis method for unbounded problems, as the domain surrounding the reservoir regions is treated as infinite or semi-infinite. Chen et al. (1997) present several strategies to analyze unbounded electromagnetic problems. Some of these strategies are also applied to mechanical problems, such as FEM with simple truncation of the outer boundaries (LEUNG et al., 2004), FEM using infinite elements (BEER, 1983; LEUNG et al., 2004; MEDINA; TAYLOR, 1983) and hybrid methods that couple FEM to other methods like boundary element method (BEM) or Green's function methods (BEER, 1983; LEUNG et al., 2004; MOLINA-VILLEGAS; BALLESTEROS ORTEGA; RUIZ CARDONA, 2022; YUAN; YIN, 2011; ZIENKIEWICZ; KELLY; BETTESS, 1977). Hybrid methods are widely used to solve unbounded electromagnetic problems (CHEN; KONRAD, 1997; LOBRY, 2021; ORIKASA et al., 1983;

QIUSHI CHEN; KONRAD; BIRINGER, 1994; SILVESTER; HSIEH, 1971; SILVESTER et al., 1977). In the field of mechanical problems, these unbounded hybrid methods are treated in the works of Zienkiewicz et al. (1977) and Beer (1983), who perform a coupling between FEM and BEM, Leung et al. (2004), where the fractal FEM is extended to the analysis of static unbounded axisymmetric problems, Yuan and Yin (2011), who use Green's functions to consider an unlimited elastic domain when analyzing functionally graded materials, and Molina-Villegas et al. (2022), who use the Green's Function Stiffness Method (GFSM) to calculate the response of beams supported on elastic Winkler foundation.

In the original version of the GFA, the displacement field generated by a pore-pressure change is calculated using an iterative numerical scheme, which limits the computational performance of the method. In addition, the validation study presented by Peres et al. (2021) shows that the convergence rate of the iterative scheme decreases when the ratio among the mechanical properties of the rocks increases, reaching a point of no convergence when the ratio is greater than 100%. These limitations have prevented the application of the GFA in real problems. To overcome this limitation, this work presents a non-iterative numerical scheme capable of expanding the applicability of the GFA and, simultaneously, improving its computational performance. Analogously to the FEM, in the proposed method the domain of interest is discretized using finite elements, whose displacement, strain and stress fields are interpolated using polynomial shape functions. However, the nodal displacements are determined without the need to truncate the mesh or use elements with special formulations (infinite elements, interface elements or others) as show in previous studies (BEER, 1983; LEUNG et al., 2004; MEDINA; TAYLOR, 1983). The integral equation of the geomechanical problem is solved from the inversion of a full matrix, as in BEM. In the proposed method, the contact interface between the region of interest and the infinite domain is solved without using specific formulations or additional discretization, as done by Chen et al. (1994) and Lobry (2021), respectively.

5.2. Theoretical background

The Green's function approach (GFA) is formulated using the reciprocity theorem, from which the displacement field of the geomechanical problem is calculated with the aid of a classical fundamental solution (Kelvin's fundamental solution, Melan's fundamental solution, among others) as shown in the following.

5.2.1. Linear poroelasticity for heterogeneous problems

According to the theory of linear poroelasticity (BIOT, 1941), the poroelastic response of a porous material is defined through the linear relationship formed by the stress change $[\Delta\sigma]$, the strain $[\varepsilon]$, and the pore-pressure variation Δp_{f}, as shown in the following

$$[\Delta\sigma] = \mathbb{C}^{\mathrm{e}} : [\varepsilon] - [A]\,\Delta p_{\mathrm{f}}\,, \tag{5.1}$$

where $\mathbb{C}^{\mathrm{e}}$ and $[A]$ are the fourth-order stiffness tensor and the second-order Biot tensor, respectively. Eq. (5.1) is only applicable to homogeneous problems. In the case of heterogeneous problems, Peres et al. (2021) propose the inclusion of complementary tensor:

$$\left[\Delta\sigma_c(\underline{x})\right] = \left(\mathbb{C}^{\mathrm{e}} - \mathbb{C}(\underline{x})\right) : [\varepsilon] \tag{5.2}$$

that represents the difference between the mechanical properties of the auxiliary (homogeneous) and geomechanical (heterogeneous) problems. In this equation, $\mathbb{C}(\underline{x})$ is the fourth-order constitutive tensor obtained from the mechanical properties found at a position $\underline{x}$ contained in the geomechanical problem domain. Considering this complementary tensor, Eq. (5.1) can be rewritten as

$$[\Delta\sigma] = \mathbb{C}^{\mathrm{e}} : [\varepsilon] - [\mathrm{A}]\,\Delta \mathrm{p}_{\mathrm{f}} - \left[\Delta\sigma_{\mathrm{c}}(\underline{\mathrm{x}})\right]. \tag{5.3}$$

5.2.2. Reciprocity theorem applied to linear and heterogeneous porous media

The oil and gas recovery processes generate changes in the pressure of the fluids contained in the pores of the reservoir rock that cause changes in the displacement, strain, and stress fields of the geological formations. As demonstrated by Peres et al. (2021), using the principle of virtual works it is possible to establish the following relationship between displacement, strain, and stress

$$\int_{\Omega_t} [\Delta\sigma] : [\hat{\varepsilon}]\,\mathrm{d}V = \int_{\partial\Omega_t} \{\hat{u}\}^{\mathrm{T}} \cdot \{\Delta T\}\,\mathrm{d}S + \int_{\Omega_t} \{\hat{u}\}^{\mathrm{T}} \cdot \{f\}\,\mathrm{d}V, \tag{5.4}$$

where $\{\hat{u}\}$ is the virtual displacement vector associated with the virtual strain tensor $[\hat{\varepsilon}]$, $\{\Delta T\}$ is the vector with the variation of surface forces generated during the fluid recovery process and $\{f\}$ is the body forces vector.

Using the reciprocity theorem, the displacement field of the geomechanical problem (the real problem) can be determined with the aid of a classical fundamental solution (auxiliary problem) whose analytical answer is known. To demonstrate this application, consider that the real problem (index 1) and the auxiliary problem (index 2) are represented by the same semi-infinite domain Ω_t. In the real problem, this domain is divided into n subdomains, which represent the layers that make up the geological formation. As shown in Figure 5.1.a, one of these subdomains defines the reservoir region (Ω_R). For the auxiliary problem, Melan's fundamental solution, in which a point force is applied in a semi-infinite elastic medium, is admitted (Figure 5.1.b).

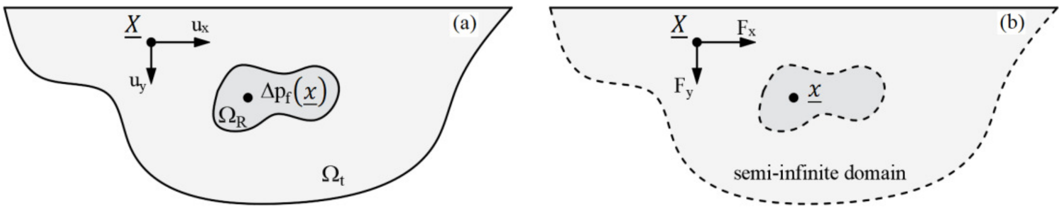

Figure 5.1. Geomechanical problem (real problem) (a) and auxiliary problem (b) domains.

Applying Eq. (5.4) to the real problem with the virtual field corresponding to the auxiliary problem and vice versa, and substituting Eq. (5.3), where the stiffness tensor $\mathbb{C}^{\mathrm{e}}$ is symmetric, results in the following relationship

$$
\begin{aligned}
&\int_{\partial\Omega_t} \{\hat{u}^{(2)}\}^{\mathrm{T}} \cdot \{\Delta T^{(1)}\}\, \mathrm{d}S + \int_{\Omega_t} \{\hat{u}^{(2)}\}^{\mathrm{T}} \cdot \{f^{(1)}\}\, \mathrm{d}V + \int_{\Omega_R} \Delta p_{\mathrm{f}}^{(1)} [A] : [\hat{\varepsilon}^{(2)}]\, \mathrm{d}V \\
&\quad + \int_{\Omega_t} \left[\Delta\sigma_c^{(1)}\right] : [\hat{\varepsilon}^{(2)}]\, \mathrm{d}V \\
&\quad = \int_{\partial\Omega_t} \{\hat{u}^{(1)}\}^{\mathrm{T}} \cdot \{\Delta T^{(2)}\}\, \mathrm{d}S + \int_{\Omega_t} \{\hat{u}^{(1)}\}^{\mathrm{T}} \cdot \{f^{(2)}\}\, \mathrm{d}V \\
&\quad + \int_{\Omega_R} \Delta p_{\mathrm{f}}^{(2)} [A] : [\hat{\varepsilon}^{(1)}]\, \mathrm{d}V + \int_{\Omega_t} \left[\Delta\sigma_c^{(2)}\right] : [\hat{\varepsilon}^{(1)}]\, \mathrm{d}V.
\end{aligned}
\tag{5.5}
$$

In the real problem (Figure 5.1.a) the unknown displacements are generated only by the pore-pressure variation Δp_{f}, so the vectors $\{\Delta T^{(1)}\}$ and $\{f^{(1)}\}$ are both null. In the auxiliary problem (Figure 5.1.b) the unknown displacements come from the unit point load $\{f^{(2)}\}$ applied at a position $\underline{X}$ of the domain (Ω_t) and, consequently, the vector $\{\Delta T^{(2)}\}$ and the variation $\Delta p^{(2)}$ can be disregarded (LEHNER; KNOGLINGER; D, 2005). The tensor $\left[\Delta\sigma_c^{(2)}\right]$ is also null, since $\mathbb{C}(\underline{x})$ is equal to $\mathbb{C}^{\mathrm{e}}$ for any position $\underline{x}$ of the auxiliary problem domain. For the case of isotropic materials, the Biot tensor $[A]$ is equal to the product of the Biot coefficient α by the identity tensor $[\mathbb{I}]$. Thus, eliminating the indices (1) and (2), the displacement in position $\underline{X}$ can be calculated by

$$\begin{aligned}\{u(\underline{X})\}^T\{e_\beta(\underline{X})\} \\ &= \int_{\Omega_R} \Delta p_{\mathrm{f}}(\underline{x})\, \alpha(\underline{x})\, \Theta_\beta(\underline{x},\underline{X})\, \mathrm{d}V \\ &+ \int_{\Omega_t} \{\varepsilon_\beta(\underline{x},\underline{X})\}^T \left[\mathbb{C}^{\mathrm{e}} - \mathbb{C}(\underline{x})\right] \{\varepsilon(\underline{x})\}\, \mathrm{d}V,\end{aligned} \tag{5.6}$$

where β is a subscript referring to the auxiliary problem, $\{u(\underline{X})\}$ is the displacement vector at position $\underline{X}$, $\{e_\beta\}$ is the direction vector of the unit point load applied in the auxiliary problem, $\Theta_\beta(\underline{x},\underline{X})$ and $\{\varepsilon_\beta(\underline{x},\underline{X})\}$ are, respectively, the volumetric strain variation and the strain vector at position $\underline{x}$ obtained from the auxiliary problem considering the unit point load applied at position $\underline{X}$, and $\{\varepsilon(\underline{x})\}$ is the strain vector calculated at position $\underline{x}$ of the real problem.

5.2.3. Numerical scheme proposed by Peres et al. (2021)

5.2.3.1. Mathematical formulation

Peres et al. (2021) present two ways of solving Eq. (5.6), which is implicit in terms of the displacement field for heterogeneous problems. The first method consists in determining the strain field $\{\varepsilon(\underline{x})\}$ directly by calculating the gradient $\partial u/\partial \underline{X}$ from the differentiation of the right side of Eq. (5.6). The second method, which is simpler and was used by the authors, consists of discretizing the problem domain into N triangular regions, generating an element mesh like those used in the FEM. As the strain field $\{\varepsilon(\underline{x})\}$ is defined by $\partial u(\underline{X})/\partial \underline{X}$, it is possible to use the discrete collocation method (ATKINSON; FLORES, 1993) to calculate the displacements at all nodes of the discretized domain. As a result, Eq. (5.6) can be rewritten as

$$
\begin{aligned}
\{u(\underline{X})\}^T\{e_\beta\} = \sum_{i=1}^{N_{\Omega_R}} \alpha^i \, \Delta p_{\mathrm{f}}^i \int_{\Omega_R^i} \Theta_\beta^{\mathrm{i}}(\underline{x},\underline{X}) \, \mathrm{d}V \\
+ \sum_{j=1}^{N_{\Omega_t}} \int_{\Omega_t^j} \{\varepsilon_\beta(\underline{x},\underline{X})\}^T [\mathbb{C}^{\mathrm{e}} - \mathbb{C}^j(\underline{x})] \, \{\varepsilon^j(\underline{x})\} \, \mathrm{d}V \, ,
\end{aligned}
\tag{5.7}
$$

where N_{Ω_R} is the number of elements in the reservoir region (subdomain Ω_R) and N_{Ω_t} is the number of elements in the domain Ω_t. In this equation, the pore-pressure variation $\left(\Delta p_{\mathrm{f}}^i\right)$ and the Biot coefficient $\left(\alpha^i\right)$ are assumed to be constant in each element. This consideration is coherent since the pore-pressure variation is provided by flow models, which are solved using discrete numerical methods.

An iterative fixed-point scheme is used to Eq. (5.7). In this scheme, the displacement field of iteration n is used to calculate the strains $\{\varepsilon^j\}$ in iteration $n+1$. The displacement field of the initial iteration is obtained using only the first summation of Eq. (5.7). The convergence of this numerical scheme is based on the norm of the displacement field (square root of the sum of the squared nodal displacement components) over the discretized domain.

5.2.3.2. Limitations

The iterative numerical scheme proposed by Peres et al. (2021) presents limitations related to the convergence rate and the CPU time required for the analysis. The results presented by them show that the numerical scheme tends to present convergence problems when the ratio between Young's modulus of the various rocks that compose the geological profile is greater than two. As the geological profile of an oil field is predominantly composed of siliciclastic rocks, carbonate rocks, and evaporites, whose ratios between Young's modules are greater than two, the use of GFA with iterative scheme to real problems becomes restrict. These results also demonstrate that the number of iterations increases with the growth of this ratio, which increases the CPU time of the analyses.

Another limitation related to the numerical scheme presented by Peres et al. (2021), which was not discussed in the article by the authors, is associated with the

Poisson's coefficient. Due to the lithostatic stress state, when analyzing an oil field formed by salt rocks (evaporitic rocks), such as the Brazilian pre-salt fields, it is common to admit that this type of rock behaves like an almost incompressible fluid (HUDEC; JACKSON, 2007; JACKSON; HUDEC, 2021; OUELLET et al., 2011). To simulate this behavior, some authors (OUELLET et al., 2011; WILLSON; FOSSUM; FREDRICH, 2002) suggest adopting a Poisson coefficient close to 0.5. For these Poisson coefficient values, the iterative scheme does not converge.

Due to these limitations, in the next section, a new numerical scheme is proposed with the aim of expanding the applicability of the GFA and, simultaneously, increasing its computational performance.

5.3. Proposed numerical scheme

The proposed numerical scheme consists of rewriting the strain vector $\{\varepsilon^j\}$ of Eq. (5.7) in order to explicitly determine the nodal displacements $\{u(\underline{X})\}^T\{e_\beta\}$ and, consequently, eliminate the iterative process. For this, the matrix $[\mathcal{B}^j(\underline{x})]$ that correlates the nodal displacements $\{u(\underline{X})\}^T\{e_\beta\}$ with the strains $\{\varepsilon^j\}$ is used. This matrix is formed by the derivatives of shape functions, as is classically found in the finite-element literature.

If the domain Ω_t is discretized into N triangular regions, as proposed by Peres et al., the displacement at each position $\underline{X}$ (nodes) can be calculated by Eq. (5.7). The first summation of this equation corresponds to the energy $\{E_\Theta\}$ generated by the volumetric strain of the elements contained in the subdomain Ω_R, that is represented by the vector with dimension $2n \times 1$ shown in the following equation

$$\{E_\Theta\} = \begin{Bmatrix} \sum_{i=1}^{N_{\Omega_R}} \alpha^i \, \Delta p_\mathrm{f}^i \int\limits_{\Omega_R^i} \Theta_{F_x}^i(\underline{x}, \underline{X}_1) \mathrm{d}V \\ \sum_{i=1}^{N_{\Omega_R}} \alpha^i \, \Delta p_\mathrm{f}^i \int\limits_{\Omega_R^i} \Theta_{F_y}^i(\underline{x}, \underline{X}_1) \, \mathrm{d}V \\ \vdots \\ \sum_{i=1}^{N_{\Omega_R}} \alpha^i \, \Delta p_\mathrm{f}^i \int\limits_{\Omega_R^i} \Theta_{F_x}^i(\underline{x}, \underline{X}_n) \mathrm{d}V \\ \sum_{i=1}^{N_{\Omega_R}} \alpha^i \, \Delta p_\mathrm{f}^i \int\limits_{\Omega_R^i} \Theta_{F_y}^i(\underline{x}, \underline{X}_n) \mathrm{d}V \end{Bmatrix}, \tag{5.8}$$

where n is the number of nodes in the mesh of triangular elements, and $\Theta_\beta^i(\underline{x}, \underline{X}_n)$ is the volumetric strain variation of the triangular element i generated by a horizontal unit point load (β equal to the horizontal force F_x) or vertical unit point load (β equal to the vertical force F_y) applied at position $\underline{X}_n$.

The second summation represents the complementary elastic energy $\{E_\mathrm{c}\}$ produced by the difference between the mechanical properties of the real and auxiliary problems. At the element level, this energy results in the vector with dimension $2n \times 1$ as

$$\{\bar{E}_\mathrm{c}\} = \begin{Bmatrix} \sum_{j=1}^{N_{\Omega_t}} \left\{ f_{c_{F_x}}^j(\underline{X}_1) \right\}^T \{u^j\} \\ \sum_{j=1}^{N_{\Omega_t}} \left\{ f_{c_{F_y}}^j(\underline{X}_1) \right\}^T \{u^j\} \\ \vdots \\ \sum_{j=1}^{N_{\Omega_t}} \left\{ f_{c_{F_x}}^j(\underline{X}_n) \right\}^T \{u^j\} \\ \sum_{j=1}^{N_{\Omega_t}} \left\{ f_{c_{F_y}}^j(\underline{X}_n) \right\}^T \{u^j\} \end{Bmatrix}, \tag{5.9}$$

with the vector $\left\{ f_{c_\beta}^j(\underline{X}_n) \right\}$ defined by

$$\left\{ f_{c\beta}^j(\underline{X}_n) \right\}^T = \int\limits_{\Omega_t^j} \{\varepsilon_\beta(\underline{x}, \underline{X}_n)\}^T [\mathbb{C}^\mathrm{e} - \mathbb{C}^j(\underline{x})] \, [\mathcal{B}^j(\underline{x})] \, \mathrm{d}V \,, \tag{5.10}$$

where $\left[\mathcal{B}^j(\underline{x})\right]$ is the matrix of the derivatives of the shape functions. Considering the connectivity of the elements used to discretize the domain Ω_t and assuming that the nodal displacements are written in terms of the global vector

$$\{U\} = \begin{Bmatrix} \{u(\underline{X}_1)\}^T\{e_{F_x}\} \\ \{u(\underline{X}_1)\}^T\{e_{F_y}\} \\ \vdots \\ \{u(\underline{X}_n)\}^T\{e_{F_x}\} \\ \{u(\underline{X}_n)\}^T\{e_{F_y}\} \end{Bmatrix}, \tag{5.11}$$

Eq. (5.9) can be rewritten in global terms as

$$\{E_c\} = [F_c]\,\{U\}\,, \tag{5.12}$$

being $[F_c]$ a matrix with dimension $2n \times 2n$. Using the vectors $\{U\}$ and $\{E_\Theta\}$ and the definition of the vector $\{E_c\}$, the nodal displacements can be obtained by

$$\{U\} = ([\mathbb{I}] - [F_c])^{-1}\{E_\Theta\}\,, \tag{5.13}$$

where $[\mathbb{I}]$ is the identity matrix of order $2n$.

The integrals of Eq. (5.8) and (5.10) are calculated using the quadrature rules indicated by Peres et al. (2021). As discussed in Appendix A, Kelvin's fundamental solution and Melan's fundamental solution are proportional to the terms $1/r$ or $1/r$ and $1/R$, respectively. In this way, if the point load is not at one of the nodes of the triangular element in which the quadrature is estimated, the quadrature rule proposed by Bartholomew (1959) is used directly. The presence of a point load at one of the nodes of the triangular element in which the quadrature is estimated makes the numerical scheme imprecise, due to the singularity in the terms $1/r$ or $1/R$. In this situation, the Duffy's transformation (BONNET, 2017; MOUSAVI; SUKUMAR, 2010) is performed, where the triangular element is transformed into a rectangle over which the function to be estimated is not singular.

The numerical system to be solved in Eq. (5.13) is formed by a full symmetric system of order $2n \times 2n$, which under similar conditions requires a higher processing time than the band system classically used in FEM. According to Golub and Van Loan (2013), to solve a full symmetric system using LU decomposition (method used by Python's NumPy library) $(64/3)n^3$ flops (floating point operations) are required and for the band system $4nk^2 + 16n^3$ flops are required, where k is the band size. When the dimensions of the two systems are equal and n tends to infinity, the ratio between the flops needed to solve the two systems is equal to $4/3$. However, when comparing the flops of the two processes, it must be considered that the geomechanical analysis via GFA requires the discretization of a small region of interest. On the other hand, when using the FEM, a large region surrounding the domain of interest must be discretized in order to simulate the infinite media and avoid the effects generated by the boundary conditions. In this way, the number of nodes in the geomechanical model used by the GFA (n_{GFA}) is typically much smaller than the number of nodes in the model used in the FEM (n_{FEM}) (for the application problem shown in Section 5.5, the relationship $n_{\mathrm{GFA}}/n_{\mathrm{FEM}}$ is equal 364). Since $n_{\mathrm{GFA}} \ll n_{\mathrm{FEM}}$, the number of operations to solve the full system of Eq. (5.13) will be less than the number of operations needed to solve the FEM band system.

5.4. Validation

The problem of a cylinder with two layers embedded in an infinite medium shown in Figure 5.2 is used to validate the proposed numerical scheme. This problem is selected because de analytical solution is available. The core of this cylinder corresponds to a reservoir of internal radius R, composed of an elastic-linear porous material with bulk modulus K_R, shear modulus G_R, and Biot coefficient α. The outer layer corresponds to the cap rock of external radius C and is formed by an elastic-linear material with incompressibility K_C and shear modulus G_C. These two layers are embedded in an infinite space composed of a linear-elastic material characterized by the modules K_∞ and G_∞. The core of this cylinder is subjected to a depletion process, in which the pressure of the fluids undergoes a variation Δp_{f}. During this variation, the pore-pressure in the other layers remains constant.

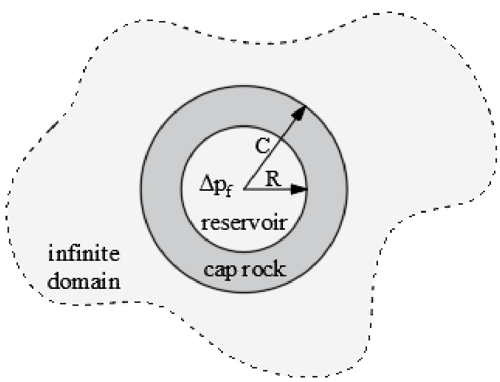

Figure 5.2. Layered cylinder geometry used for the numerical scheme validation study.

The results obtained via numerical simulation are compared with the results calculated from the analytical solution presented in Peres et al. (2021). The parameters selected for the numerical solutions are given in Table 5.1. The meshes of triangular elements are created using the Delaunay triangulation algorithm implemented in the Triangle software (SHEWCHUK, 1996) and are shown in Figure 5.3. Circular interfaces between layers are approximated using 200 line segments. The 2D Kelvin's solution is used as the auxiliary problem.

Table 5.1. Material, geometrical, and numerical data for the layered cylinder problem used for validation.

Notation	***Definition***	***Value/Range***	***Unit***
C/R	Ratio cap rock to Reserv. radius	1.5	-
E_R	Young's modulus, reservoir	10.0	GPa
ν_R	Poisson's ratio, reservoir	0.200	-
α_R	Biot coefficient, reservoir	0.800	-
Δp_f	Fluid pressure change, reservoir	-5.0	MPa
E_C	Young's modulus, cap rock	5.0(*) / 10.0 / 15.0 / 20.0 / 50.0	GPa
ν_C	Poisson's ratio, cap rock	0.20(*) / 0.40 / 0.45 / 0.49 / 0.495 / 0.499	-
E_∞	Young's modulus, infinite space	10.0	GPa
ν_∞	Poisson's ratio, infinite space	0.200	-
	Numerical scheme		
	Bartholomew level for quadr.	3	
	Gauss quadr. Duffy's transf.	3×3	
	Iterative scheme tol. (**) (***)	10^{-6}	
	Max. number of iterations (***)	50	

(*) Default value used in the analyses, except for the analyzes where the other values are evaluated.

(**) Tolerance used to calculate the relative CPU times shown in Section 5.4.2.

(***) Parameters for iterative scheme used by Peres et al. (2021).

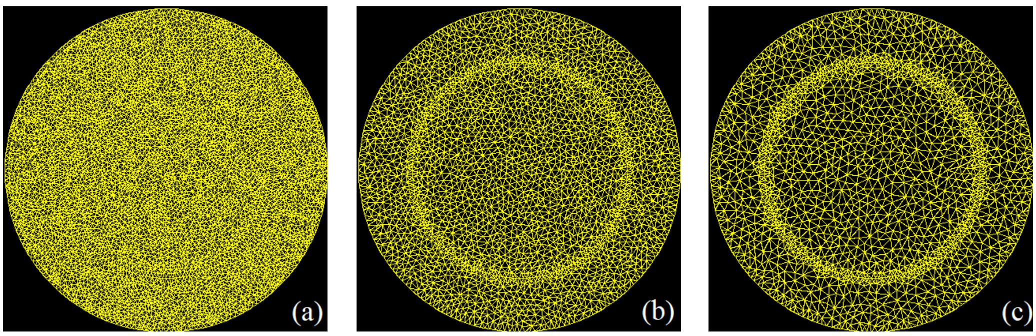

Figure 5.3. Meshes used in the validation study. The maximum normalized sizes of the elements are (a) 0.0010, (b) 0.0025, (c) 0.0050, (d) 0.0075, (e) 0.0100, (f) 0.0150, (g) 0.0200 e (h) 0.0500.

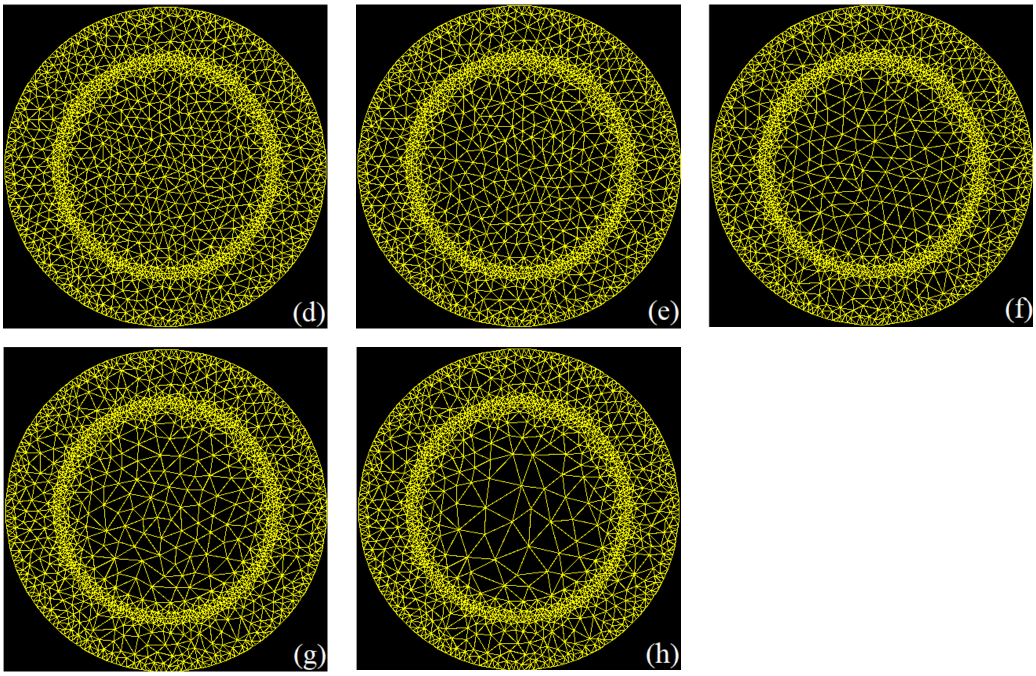

Figure 5.3. Meshes used in the validation study. The maximum normalized sizes of the elements are (a) 0.0010, (b) 0.0025, (c) 0.0050, (d) 0.0075, (e) 0.0100, (f) 0.0150, (g) 0.0200 e (h) 0.0500 (continuation).

5.4.1.
h-convergence and material properties variation

The h-convergence analysis aims to verify if the numerical solution approaches the analytical solution when the size of the elements decreases. The error introduced by the spatial discretization of the layered cylinder domain Ω_{LC} is estimated through the displacement field norm

$$\frac{1}{V_{LC}} \int_{\Omega_{LC}} \left|\{u(\underline{X})\}\right| dV \,, \tag{5.14}$$

where V_{LC} is the volume (area in 2D) of the layered cylinder. Figure 5.4 presents the relative error, defined by the difference between the norm of the numerical solution and the norm of the analytical solution and normalized by the latter, as a function of the average size of elements. This average size corresponds to the average area of the elements divided by the area of the layered cylinder. The results obtained show that the relative error decreases when the average size of the elements tends to zero. For an average size of less than 0.0002, it is observed that the relative error is less than 0.2%, an acceptable value for geomechanical problems.

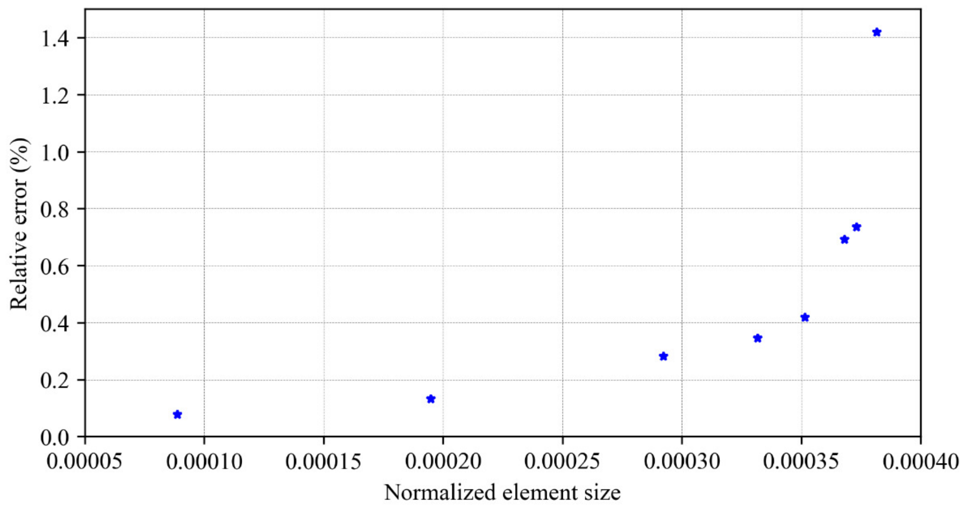

Figure 5.4. The relative error in displacement norm as a function of the average element size.

To illustrate h-convergence, the radial displacements of different models are plotted in Figure 5.5. The mechanical parameters (Young's modulus and Poisson's coefficient) of the rocks that form these models were defined to demonstrate that the proposed numerical scheme can be used when the ratio between Young's modulus of the rocks that make up the geological profile is greater than two or when the Poisson's coefficient of cap rock assumes values close to 0.5. The solid curves describe the results obtained via GFA and the circular points represent the analytical results. In all cases analyzed, the difference between these results is not perceptible.

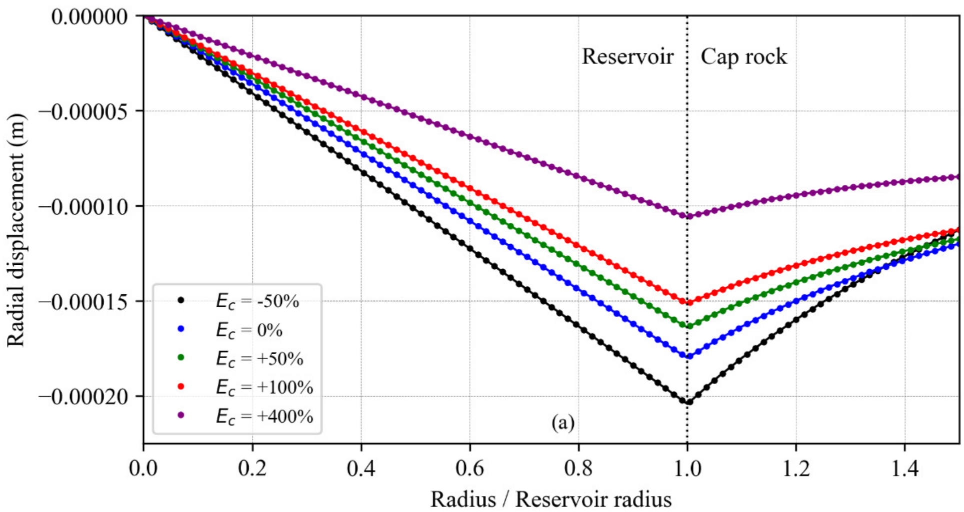

Figure 5.5. Comparison between the radial displacement results calculated by GFA (solid line) and via the analytical solution (circle symbols). In (a) different values of Young's modulus for the cap rock are analyzed, in (b) different values of Poisson's coefficient are verified, and in (c) the radial displacements of (b) are shown in detail.

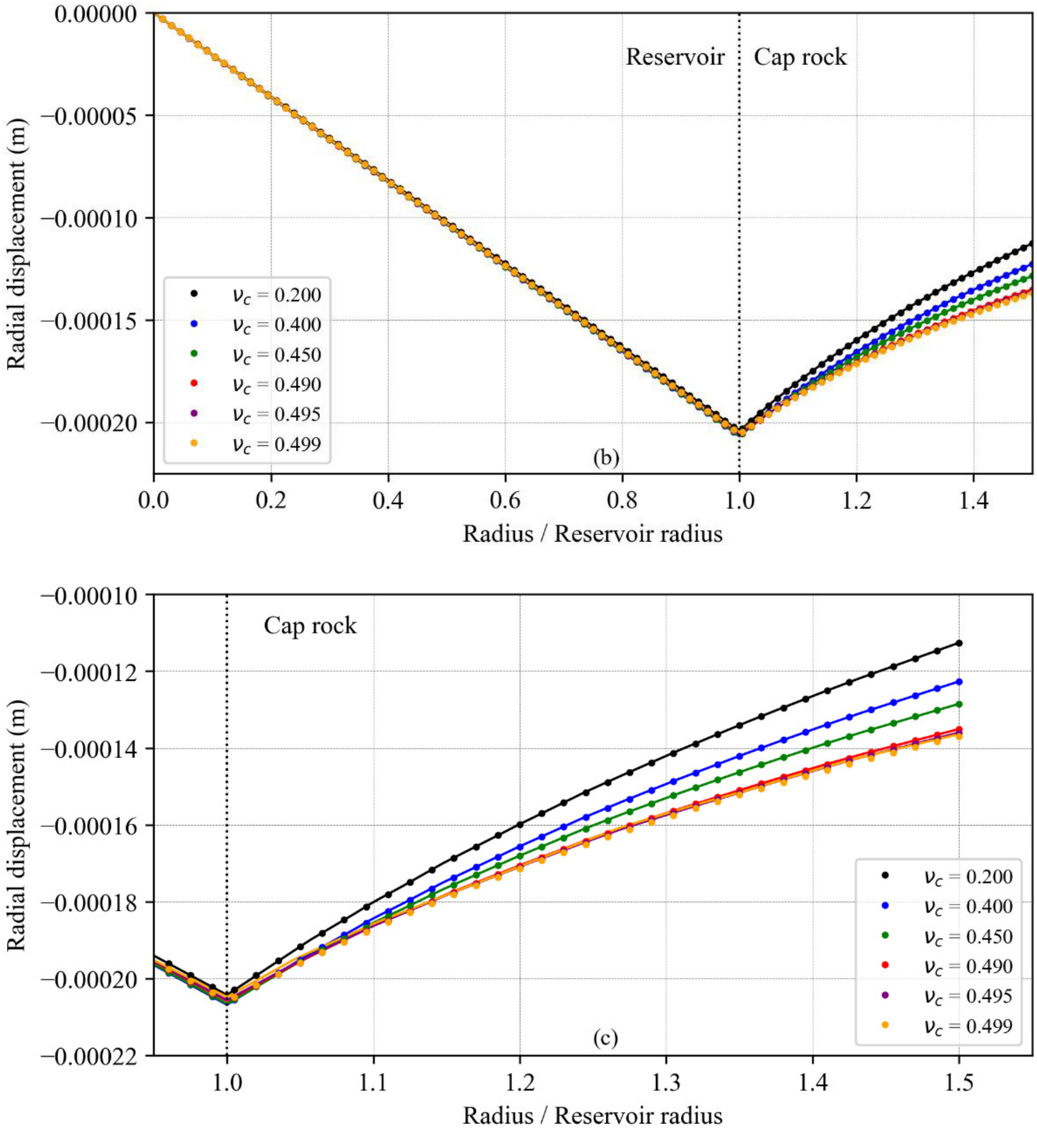

Figure 5.5. Comparison between the radial displacement results calculated by GFA (solid line) and via the analytical solution (circle symbols). In (a) different values of Young's modulus for the cap rock are analyzed, in (b) different values of Poisson's coefficient are verified, and in (c) the radial displacements of (b) are shown in detail (continuation).

5.4.2. CPU time comparison

The computational performance of the proposed numerical scheme is also an important parameter to be analyzed. For this, it is used the relative CPU time calculated by the relation between the CPU time obtained with the numerical scheme proposed by Peres et al. (2021) and with the current numerical scheme.

The results of Figure 5.6.a show that the proposed scheme is between 5.5 and 8.0 times faster than the iterative scheme when the mechanical properties are kept constant, and the element sizes are changed. Figure 5.6.b shows that the relative CPU time increases when the ratio between Young's modulus of cap rock and reservoir rock (elasticity contrast) increases. When the elasticity contrast is close to 1%, the CPU times of both numerical schemes are approximately equal. On the other hand, when the elasticity contrast is 90% the CPU time of the proposed scheme is between 12.5 (more refined mesh) and 17.5 (less refined mesh) times less than the CPU time of the iterative scheme.

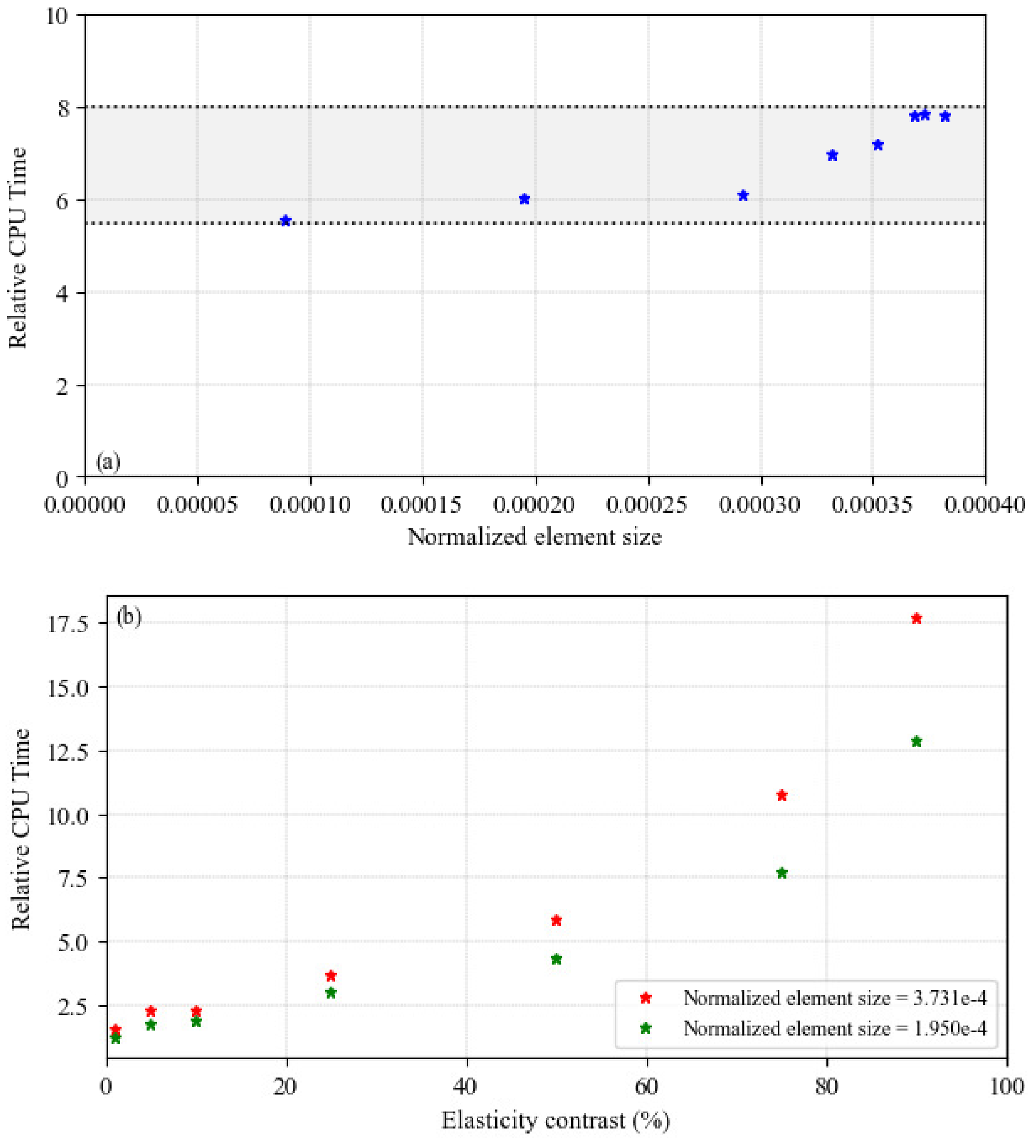

Figure 5.6. (a) relative CPU time as a function of the average size of the elements and (b) relative CPU time as a function of the elasticity contrast between cap rock and reservoir rock.

5.5. Application

In this Section, a geological profile formed by four distinct layers (Figure 5.7) is analyzed using Green's function approach with the proposed non-iterative numerical scheme. This profile represents a typical section of the Brazilian pre-salt and was inspired by a seismic image of the Tupi field (Santos Basin, Brazil) found in Mohriak et al. (2012). The mechanical properties of the rocks that form the geological profile are shown in Figure 5.7. The salt rock is simulated as an almost incompressible fluid (Poisson's coefficient equal to 0.495) to adequately represent the lithostatic stress state of the geological formation. The reservoir is divided into two regions whose pore-pressure variations are -50 MPa, in the production (depletion) region, and 20 MPa, in the injection region. Melan's fundamental solution (MELAN, 1932) is used as an auxiliary problem. The mechanical properties of semi-infinite media are the same as those of the under-burden layer.

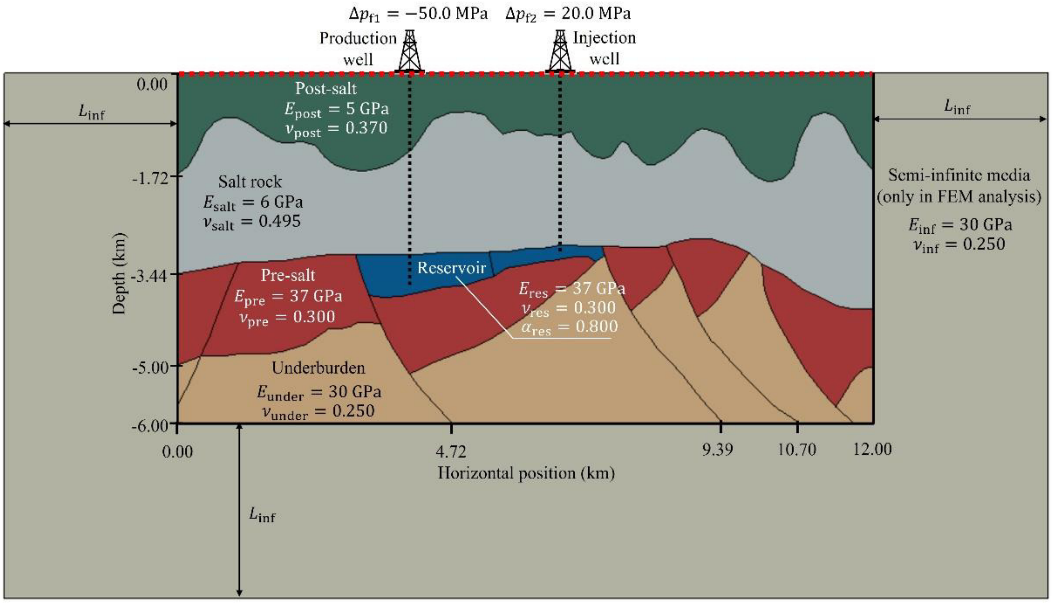

Figure 5.7. Representative 2D model of a geological section of the Brazilian pre-salt.

The analysis using GFA is performed considering the Bartholomew quadrature with level 3 and the Gauss quadrature, applied after the Duffy transformation, with 9 integration points. The results obtained with the GFA are compared with the results found in five FEM models developed using the commercial software Abaqus (DASSAULT SYSTEMES, 2017). In these models, the semi-infinite media is modeled considering the simple truncation of the outer boundary. For this, an extra layer with a length L_{inf} (showed in Figure 5.7), which varies between 0 (model without semi-infinite media), $2L_0$, $5L_0$, $10L_0$, and $20L_0$ with L_0 equal to 6.0 km, is used. In the analysis via non-iterative GFA the domain of interest (domain Ω_t) is discretized using triangular elements with three nodes and linear shape functions. In the analyzes carried out with the FEM, quadrilateral elements with four nodes and linear shape functions are used. In all cases, elements with a maximum dimension equal to 100 meters are used (this value was defined after carrying out mesh convergence studies). Due to the values of the mechanical properties of the materials, the solution to this problem is not achieved using the numerical scheme proposed by Peres et al. (2021), because the iterative process does not converge.

Figure 5.8 presents the horizontal and vertical displacement along the dotted segment defined in Figure 5.7. These curves show that the results obtained by GFA are close to the results found using FEM when L_{inf} increases. Furthermore, the results obtained via FEM by the models with L_{inf} equal to $10L_0$ and $20L_0$ are the closest to the results obtained using the proposed method. For these two values, the greatest divergences are observed at the ends of the horizontal displacement curve (Figure 5.8.a), where the values calculated by the GFA are 0.87% ($10L_0$) and 0.84% ($20L_0$) higher than those found by the FEM. In the case of vertical displacement (Figure 5.8.b), in both methods, the maximum value occurred close to the position of 3900 meters, where the value obtained by the GFA is 2.4% and 0.5% higher than the values found using FEM with $10L_0$ and $20L_0$, respectively.

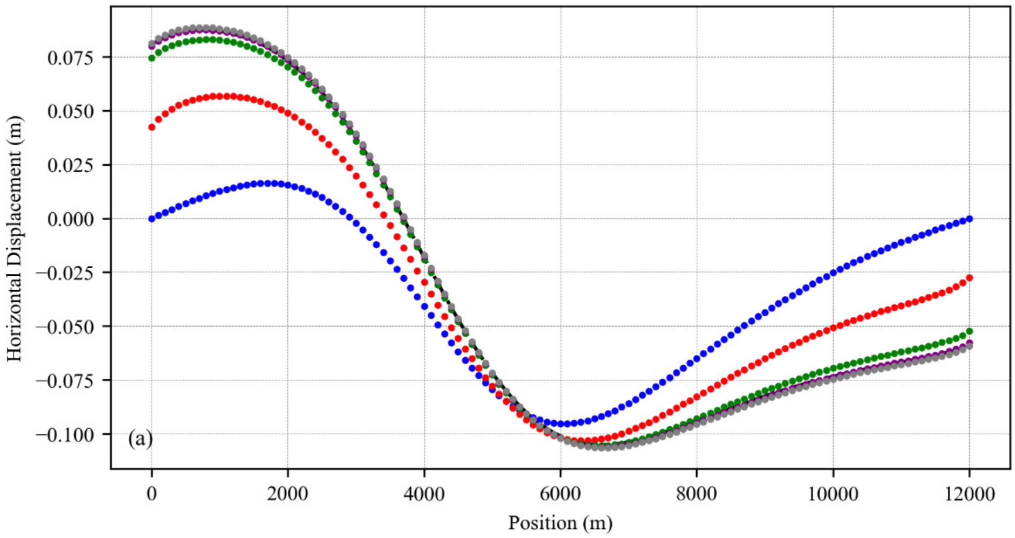

Figure 5.8. (a) horizontal and (b) vertical displacement along the dotted segment defined in Figure 5.7.

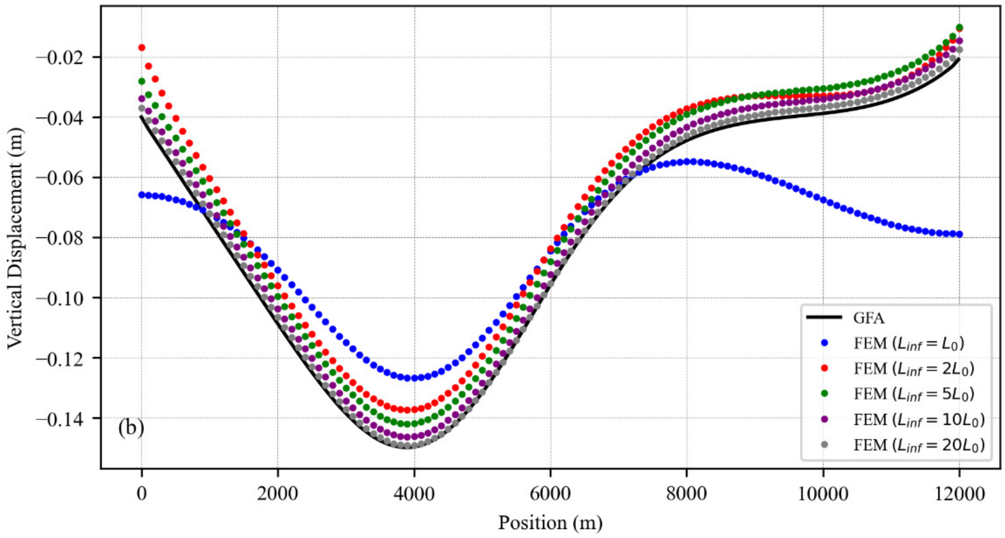

Figure 5.8. (a) horizontal and (b) vertical displacement along the dotted segment defined in Figure 5.7 (continuation).

Figure 5.9 presents the displacement fields obtained from GFA (Figure 5.9.a) and FEM model with $L_{\mathrm{inf}} = 20L_0$ (Figure 5.9.b). Visually analyzing these results, it is noted that the displacement fields are almost identical at all points in the problem domain.

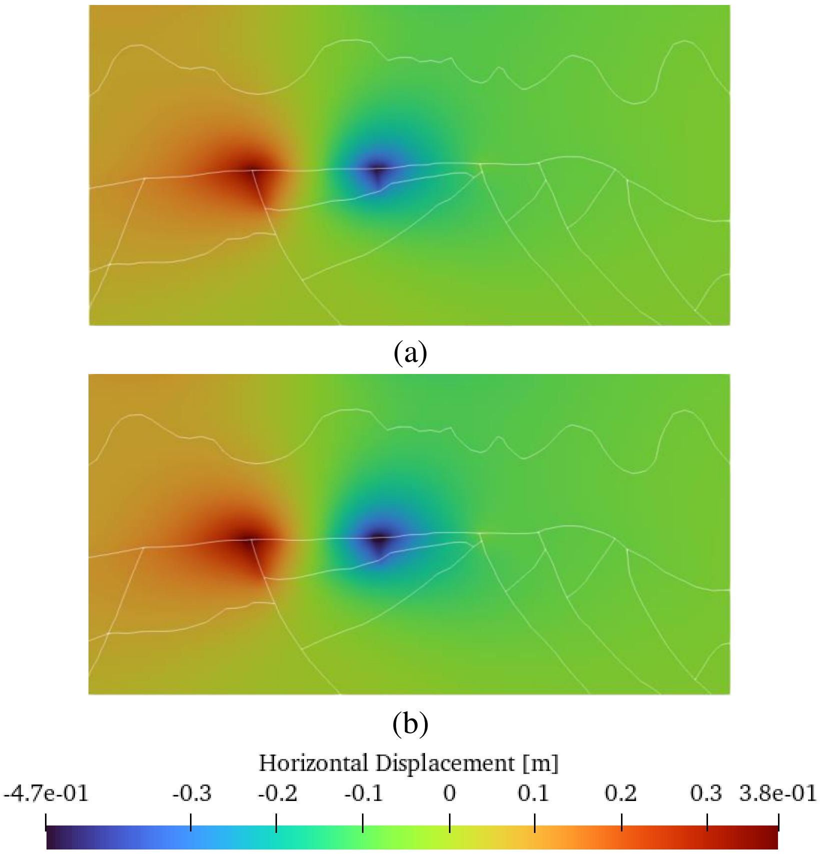

Figure 5.9. Vertical and horizontal displacement fields calculated from the GFA (top) and FEM (bottom) after the injection and production process indicated in Figure 5.7.

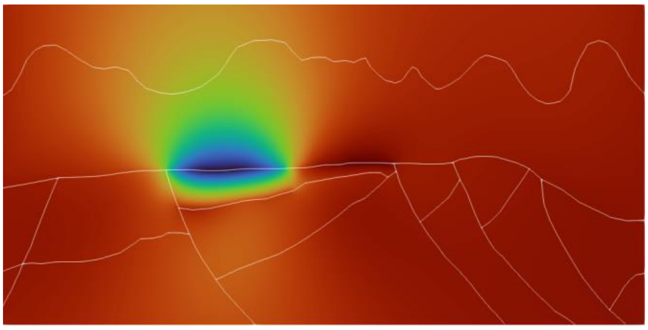

(c)

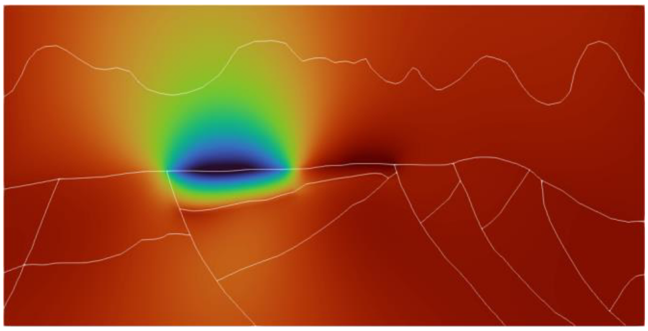

(d)

Figure 5.9. Vertical and horizontal displacement fields calculated from the GFA (top) and FEM (bottom) after the injection and production process indicated in Figure 5.7 (continuation).

Comparing the strain fields found by both methods (Figure 5.10), it is observed an agreement between the results, being possible to identify the same regions of maximum swelling and compaction. In both cases, the maximum horizontal swelling (Figure 5.10.a and Figure 5.10.b) occurs within the production region and in part of the salt rock layer. The maximum vertical swelling (Figure 5.10.c and Figure 5.10.d) happens in the injection region and the salt rock layer above the reservoir. The maximum vertical compaction (Figure 5.10.c and Figure 5.10.d) is located in the production region, the same region where shear strains (Figure 5.10.e and Figure 5.10.f) are visible.

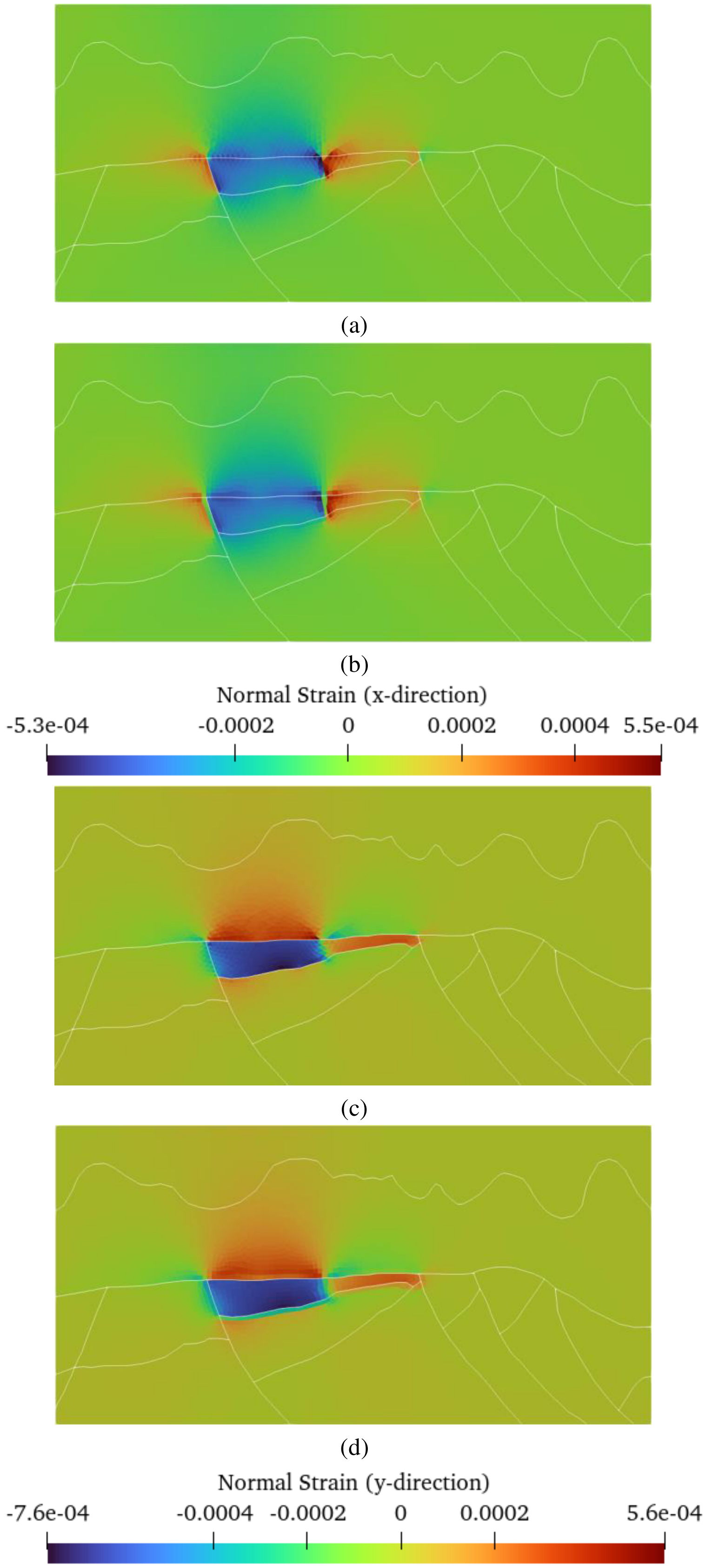

Figure 5.10. Strain fields calculated from the GFA (top) and FEM (bottom) after the injection and production process indicated in Figure 5.7.

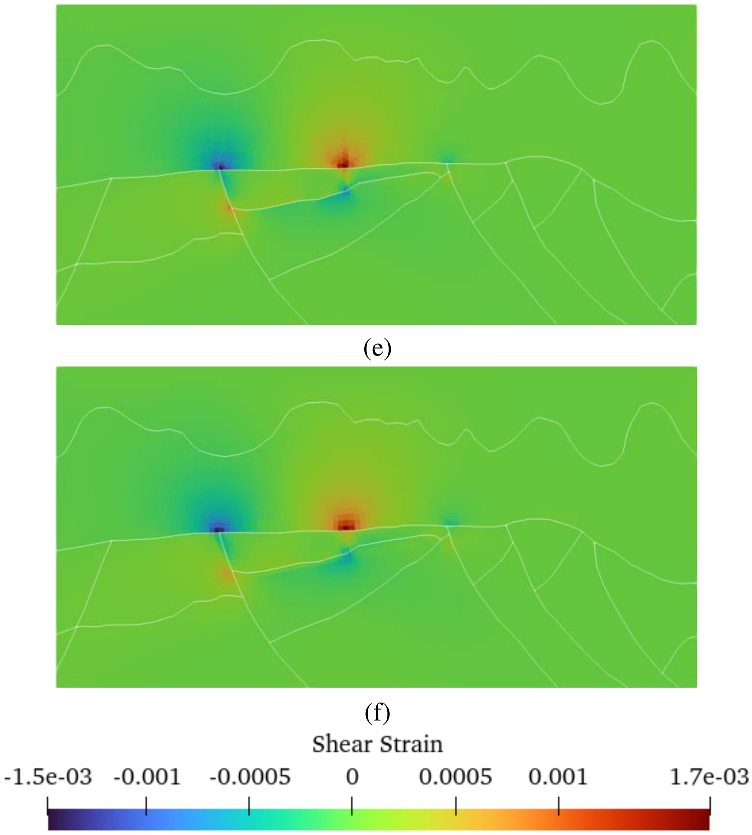

Figure 5.10. Strain fields calculated from the GFA (top) and FEM (bottom) after the injection and production process indicated in Figure 5.7 (continuation).

It is important to note that in the present work, the non-iterative GFA method was implemented using Python and it was not parallelized. On the other hand, the FEM results were obtained using Abaqus software, which is implemented in FORTRAN, which is widely recognized to be a much more efficient language than Python. Furthermore, Abaqus is a commercial software that has been parallelized and optimized. Thus, comparing CPU times between the two simulations would not be very meaningful. A fairer way of comparing the efficiency of the two methods would be to count the number of floating-point operations (flops) performed in each method. The number of degrees of freedom (DOF) of the model used in the GFA is 364 smaller than the DOF of the model analyzed through the FEM ($20L_0$). Using the concept of flops discussed in Section 5.3, it takes approximately 1.33×10^{12} flops to solve the full system ($[\mathbb{I}] - [F_c]$) of the GFA shown in Eq. (5.13) and 3.83×10^{20} flops to solve the band system classically used in FEM, a value that is 2.88×10^{8} times large. This demonstrates that the application of the proposed method for the analysis of real geomechanical problems is feasible and computationally attractive.

5.6. Conclusion

The present work proposes a non-iterative numerical scheme for the GFA. Through this scheme, the GFA can be used for the analysis of geological formations with mechanical properties like those found in the field. Using the iterative numerical scheme proposed by Peres et al. (2021), this type of analysis does not converge, due to the ratios of Young´s modulus of elasticity between rock layers. Furthermore, when compared to the iterative scheme, the validation and performance tests demonstrate that the proposed scheme is more efficient. In the layered cylinder problem, the non-iterative scheme is between 5.5 and 8.0 times faster than the iterative scheme when the mechanical properties are kept constant, and the element sizes are modified. In the analysis where the elasticity contrasts are changed this relation reaches 17.5. The validation tests also show that the GFA using the proposed numerical scheme presents satisfactory results when the Poisson's coefficient of one of the layers is closer to 0.5, unlike the iterative scheme.

The applicability of this Green's function with the non-iterative scheme is demonstrated using a geological profile constructed from a seismic image of the Tupi field located in the Brazilian pre-salt. In this analysis, the salt rock is simulated as a nearly incompressible fluid with Young's modulus of 6 GPa and Poisson's coefficient of 0.495. The displacement and strain fields found from the GFA are compared to the fields obtained through the FEM using the commercial software Abaqus (DASSAULT SYSTEMES, 2017). However, to obtain similar accuracy, in the FEM model it is necessary to discretize a region much larger than the one necessary to carry out the analysis via GFA. Consequently, the GFA has 364 times fewer degrees of freedom (considering the model $20L_0$) than the FEM and, therefore, less computational effort is required to perform the analysis. This is highlighted using the metric of floating-point operations (flops) discussed in Section 5.3. According to this metric, it takes approximately 1.33×10^{12} flops to solve invert the complete system $([\mathbb{I}] - [F_c])$ of the GFA shown in Eq. (5.13) and 3.83×10^{20} flops to solve the band system classically used in FEM, a value that is 2.88×10^{8} times larger.

The non-iterative numerical scheme is able to expand the applicability of the GFA and to reduce the CPU time of the analysis. In this way, it can be concluded that the objectives of the research are achieved. Future developments include the extension of the method for the analysis of 3D problems and the implementation of viscoelastic and plastic constitutive models that allow an adequate representation of the mechanical behavior of rocks.

6
“Evaluation of the spatial variability of the mechanical properties of rocks in heterogeneous fluid-saturated media using non-iterative Green's function approach and first-order second-moment stochastic method”

Paper submitted by Leonardo C. Mesquita, Elisa D. Sotelino, and Matheus L. Peres in the Computer Methods in Applied Mechanics and Engineering (under review).

Abstract

The present work proposes a new version of the Green-FOSM method, which eliminates the iterative calculation process of the original version and, simultaneously, solves the convergence problems related to the mechanical properties of rocks that form the geological formation. Considering the same computational resources, this non-iterative version of the Green-FOSM method is up to 200 times faster than the original iterative process. In addition, it allows analyzing problems with more than 10,000 random variables, value that in the original method is less than 3,000. To demonstrate its validity, the proposed method is applied to a hypothetical 2D model submitted to a fluid depletion process. For all the different levels of correlation and spatial variability, the statistical results obtained by the proposed methods agree well with the results obtained via Monte Carlo Simulation (MSC). The relationship between CPU times demonstrates that the proposed method is at least 50 times faster than MCS. In the end, the non-iterative Green-FOSM method is used to obtain the displacement, strain and stress fields of a geological section constructed from a seismic image of Brazilian pre-salt oil region. The results found show that, depending on the levels of spatial variability, the analyzed fields can assume values up to 30.6% higher or lower than the values obtained deterministically.

6.1. Introduction

The injection or extraction of fluids in underground reservoir produces alterations in pore pressure of the reservoir rock, which impacts the mechanical behavior of the entire geological formation. These alterations, generated during the processes of hydrocarbon production (MINKOFF; KRIDLER, 2006), water extraction (TEATINI et al., 2006), transport of solutes in aquifers (BONAZZI; JHA; DE BARROS, 2021), or CO_2 or natural gas storage (FERRONATO et al., 2010; LU, 2010; PAN et al., 2016; RUTQVIST et al., 2016; SIRIWARDANE et al., 2016; TEATINI et al., 2011; VILARRASA et al., 2019), modify the displacement, strain and stress fields of the rock massif. As a direct consequence of these alteration, the rock reservoir undergoes a volumetric variation, which can affect its permeability and reduce the rate of fluid extraction (GAMAGE et al., 2011; OSTENSEN, 1986). At the same time, subsidence or uplifting of the free surface can occur, and this affects the functionality and stability of the structures present in the reservoir region (FIGUEROA-MIRANDA et al., 2018). These alterations can also generate secondary problems, such as wellbore collapse, failures in offshore platforms, fault reactivation, and seismic events (BOURNE et al., 2014; MINKOFF; KRIDLER, 2006; PAULLO MUÑOZ; ROEHL, 2017; VERDON et al., 2016). In addition, during the fluid recovery process, the monitoring of the geological profile is done using seismic measurements, which are affected by alterations in the strain field (BARKVED; KRISTIANSEN; FJÆR, 2005; HATCHELL et al., 2007; HERWANGER; HORNE, 2009; TEMPONE; LANDRØ; FJÆR, 2012). These examples have motivated the development of deterministic analytical and numerical methods that allow the prediction of the impact of injection or extraction of fluids on the geological formation.

In general, the analytical methods have the advantage of being simple. However, they are limited in terms of the geometry and heterogeneity of the geological profile and the mechanical behavior of the materials that they can consider. Among these methods, the most used is the method proposed by Geertsma (GEERTSMA, 1957, 1973a, 1973b), which is based on the nucleus-of-strain principle introduced by Mindlin and Cheng (1950). The restrictions of analytical methods are overcome using numerical methods, which are commonly based on the finite element method (FEM) (HADDAD; EICHHUBL, 2020; LELE et al., 2016; WATANABE et al., 2010). These methods are capable of considering the particularities of each geological formation. However, in most situations, the construction of the models is labor intensive and require large amounts of storage, and model processing demands a high computational effort.

The Green's function approach (GFA) (PERES et al., 2021), uses classical Green's function as an auxiliary solution to obtain the variation of the displacement field of a geological massif subjected to a fluid injection and/or extraction process. The great advantage of this method compared to the classic FEM is that it does not require the imposition of boundary conditions and the analysis can be performed considering only the reservoir or other regions of interest. As the analytical methods, o GFA is simple and computationally efficient. Furthermore, it does not present limitations in terms of geometry, number of layers, and heterogeneity of the geological profile, and it can be applied to materials with linear and non-linear behavior.

The analytical and numerical methods presented above deal with the effects of fluid extraction or injection process deterministically, as they do not consider the uncertainties associated with the process. However, these uncertainties can affect the results (BAÙ et al., 2016) and lead to responses that do not agree with in-situ observations (MULLER et al., 2009b, 2009a). In order to consider these uncertainties, Mesquita et al. (2023) developed a stochastic statistical method, called Green-FOSM, based on GFA and the first-order second-moment method (FOSM). Using this method, it is possible to predict changes in the displacement field generated by variation in pore pressure and, at the same time, consider the spatial variability of the mechanical properties of the rock that form the geological profile.

As in the original version of the GFA, the original Green-FOSM method uses an iterative calculation scheme, which presents convergence problems when the relationship between the Young's modulus of the rocks that make up the geological profile increases (not converging when this relationship is greater than 100%), or when Poisson's ratio is close to 0.5 (Chapter 5). These limitations prevent the application of the Green-FOSM method in real problems. Additionally, the iterative scheme jeopardizes the computational performance of the method. Due to these limitations, the present work proposes a new version of the Green-FOSM method. This version eliminates the iterative calculation process of the original version and, simultaneously, solves the convergence problems related to the mechanical properties of rocks. Furthermore, by eliminating the iterative process, the computation performance of the Green-FOSM method is improved.

6.2. Deterministic formulation of the Green's function approach

The GFA is formulated from the principle of virtual work and the theorem of reciprocity (PERES et al., 2021). Using these concepts, the displacement field of the analyzed geomechanical problem is calculated with the aid of a classic fundamental solution such as Kelvin's fundamental solution (THOMSON, 2015) and Melan's fundamental solution (MELAN, 1932), among others as is presented in the following sections.

6.2.1. Linear poroelasticity applied to heterogeneous problems

The linear poroelasticity theory proposed by (BIOT, 1941) establishes that the poroelastic response of a porous material is given by the linear relationship between stress variation $[\Delta\sigma]$, strain $[\varepsilon]$, and pore pressure variation Δp_{f}, as shown in Eq. (6.1)

$$[\Delta\sigma] = \mathbb{C}^{\mathrm{e}} : [\varepsilon] - [A]\,\Delta p_{\mathrm{f}}\,, \tag{6.1}$$

where $\mathbb{C}^{\mathrm{e}}$ and $[A]$ are the fourth-order constitutive tensor and the second-order Biot tensor, respectively. Eq. (6.1) is valid for homogeneous problems. For heterogeneous problems, Peres et al. (2021) propose the addition of the complementary tensor, which considers the difference between the mechanical properties of the homogeneous problem, represented by the classical fundamental solution, and the heterogeneous problem, defined as a real geomechanical problem. This is shown in Eq. (6.2), in which the term $\mathbb{C}(\underline{x})$ corresponds to the fourth-order constitutive tensor calculated from the mechanical properties of the material located in position $\underline{x}$ contained in the domain of the real geomechanical problem.

$$[\Delta\sigma_c(\underline{x})] = \left(\mathbb{C}^{\mathrm{e}} - \mathbb{C}(\underline{x})\right) : [\varepsilon] \tag{6.2}$$

Using this tensor, the poroelastic response of the heterogeneous geomechanical problem is given by

$$[\Delta\sigma] = \mathbb{C}^{\mathrm{e}} : [\varepsilon] - [A]\,\Delta p_{\mathrm{f}} - \left[\Delta\sigma_c(\underline{x})\right]. \tag{6.3}$$

6.2.2. Reciprocity theorem extended to linear and heterogeneous porous media

From the principle of virtual work, it is possible to establish the following relationship amongst displacement, strain, and stress

$$\int_{\Omega_t} [\Delta\sigma] : [\hat{\varepsilon}]\,\mathrm{d}V = \int_{\partial\Omega_t} \{\hat{u}\}^{\mathrm{T}} \cdot \{\Delta T\}\,\mathrm{d}S + \int_{\Omega_t} \{\hat{u}\}^{\mathrm{T}} \cdot \{f\}\,\mathrm{d}V, \tag{6.4}$$

with $\{\hat{u}\}$ being the virtual displacement vector, $[\hat{\varepsilon}]$ the virtual strain tensor, $\{\Delta T\}$ the vector that contains the variation of surfaces forces generated by the fluid injection or depletion processes, and $\{f\}$ the force vector that does not consider the surface forces. Applying the theorem of reciprocity, the displacement field of the geomechanical problem (real problem) can be determined with the aid of a classic fundamental solution (auxiliary problem) whose analytical response is known. To demonstrate this application, admit that the real problem (index 1) and the auxiliary problem (index 2) have the same semi-infinite domain Ω_t. In the real problem, this domain is divided into n subdomains Ω_n, which define the layers of geological formation. As shown in Figure 6.1.a, one of these subdomains represents the reservoir region (subdomain Ω_{R}), which is subjected to pore pressure variation Δp_{f}. As the auxiliary problem Melan's fundamental solution (MELAN, 1932) is adopted, where a concentrated force is applied in a homogeneous elastic semi-infinite domain (Figure 6.1.b).

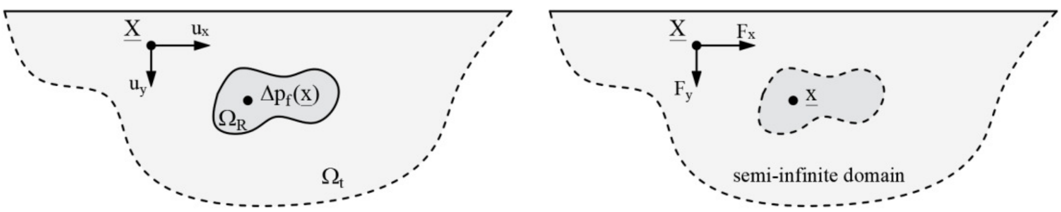

Figure 6.1. (a) real problem domain with reservoir region (subdomain Ω_R) and (b) auxiliary problem domain.

Applying the Eq. (6.4) to the real problem (index 1) with the virtual field of the auxiliary problem (index 2) and vice versa, and substituting in Eq. (6.3), in which the fourth order constitutive tensor $\mathbb{C}^{\mathrm{e}}$ is symmetric, it is possible to reach the following relationship

$$\int_{\partial\Omega_t} \{\hat{u}^{(2)}\}^{\mathrm{T}} \cdot \{\Delta T^{(1)}\}\, \mathrm{d}S + \int_{\Omega_t} \{\hat{u}^{(2)}\}^{\mathrm{T}} \cdot \{f^{(1)}\}\, \mathrm{d}V + \int_{\Omega_R} \Delta p_{\mathrm{f}}^{(1)} [A] : [\hat{\varepsilon}^{(2)}]\, \mathrm{d}V$$
$$+ \int_{\Omega_t} \left[\Delta\sigma_c^{(1)}\right] : [\hat{\varepsilon}^{(2)}]\, \mathrm{d}V \tag{6.5}$$
$$= \int_{\partial\Omega_t} \{\hat{u}^{(1)}\}^{\mathrm{T}} \cdot \{\Delta T^{(2)}\}\, \mathrm{d}S + \int_{\Omega_t} \{\hat{u}^{(1)}\}^{\mathrm{T}} \cdot \{f^{(2)}\}\, \mathrm{d}V$$
$$+ \int_{\Omega_R} \Delta p_{\mathrm{f}}^{(2)} [A] : [\hat{\varepsilon}^{(1)}]\, \mathrm{d}V + \int_{\Omega_t} \left[\Delta\sigma_c^{(2)}\right] : [\hat{\varepsilon}^{(1)}]\, \mathrm{d}V.$$

In the real problem (index 1) the unknown displacements are generated only by pore pressure variation Δp_{f}, so the vectors $\{\Delta T^{(1)}\}$ and $\{f^{(1)}\}$ are both nulls. In the auxiliary problem (index 2) the displacements come from the unit concentrated force $\{f^{(2)}\}$ applied to a position $\underline{X}$ of the domain (Ω_t) and, therefore, the vector $\{\Delta T^{(2)}\}$ and the variation $\Delta p^{(2)}$ can be disregarded (LEHNER; KNOGLINGER; D, 2005). The tensor $\left[\Delta\sigma_c^{(2)}\right]$ is also null, because $\mathbb{C}(\underline{x})$ is equal to $\mathbb{C}^{\mathrm{e}}$ for any position $\underline{x}$ within the domain of the auxiliary problem. For the case of isotropic materials, the second-order Biot tensor $[A]$ is equal to the product of the Biot coefficient α by the second order identity tensor $[\mathbb{I}]$. Thus, eliminating the indexes (1) and (2), the horizontal or vertical displacement in position $\underline{X}$ can be obtained by

$$\{u(\underline{X})\}^T \{e_\beta(\underline{X})\}$$
$$= \int_{\Omega_R} \Delta p_{\mathrm{f}}(\underline{x})\, \alpha(\underline{x})\, \Theta_\beta(\underline{x}, \underline{X})\, \mathrm{d}V \tag{6.6}$$
$$+ \int_{\Omega_t} \{\varepsilon_\beta(\underline{x}, \underline{X})\}^T [\mathbb{C}^{\mathrm{e}} - \mathbb{C}(\underline{x})]\, \{\varepsilon(\underline{x})\}\, \mathrm{d}V,$$

where β is a subscript referring to the auxiliary problem, $\{u(\underline{X})\}$ is the displacement vector at position $\underline{X}$, $\{e_\beta\}$ is the direction vector of the unit point load applied in the auxiliary problem, $\Theta_\beta(\underline{x}, \underline{X})$ and $\{\varepsilon_\beta(\underline{x}, \underline{X})\}$ are, respectively, the volumetric strain variation and the strain vector at position $\underline{x}$ obtained from the auxiliary problem considering the unit point load applied at position $\underline{X}$, and $\{\varepsilon(\underline{x})\}$ is the strain vector calculated at position $\underline{x}$ of the real problem.

6.3. Uncertainties evaluation using the non-iterative Green's function approach

Due to the heterogeneity of the real problem, in Eq. (6.6) the displacement vector $\{u(\underline{X})\}$ is implicitly calculated from the strains $\{\varepsilon(\underline{x})\}$. Peres et al. (2021) present two ways to solve this equation. The first way consists in determining the strains $\{\varepsilon(\underline{x})\}$ directly, calculating the gradient $\partial u/\partial \underline{X}$ from the differentiation of the right side of Eq. (6.6). The second way, which is used by Peres et al. (2021), consists of discretizing the Ω_t domain into N_Ω triangular regions forming an element mesh like those used in the FEM. From the direct colocation method (ATKINSON; FLORES, 1993), the displacements are calculated at each node of the discretized domain Ω_t. Considering this discretization, Eq. (6.6) can be rewritten as

$$\begin{aligned}\{u(\underline{X})\}^T\{e_\beta\} = &\sum_{i=1}^{N_{\Omega_R}} \alpha^i\, \Delta p_{\mathrm{f}}^i \int_{\Omega_R^i} \Theta_\beta^{\mathrm{i}}(\underline{x},\underline{X})\,\mathrm{d}V \\ &+\sum_{j=1}^{N_{\Omega_t}} \int_{\Omega_t^j} \{\varepsilon_\beta(\underline{x},\underline{X})\}^T[\mathbb{C}^{\mathrm{e}}-\mathbb{C}^j(\underline{x})]\,\{\varepsilon^j(\underline{x})\}\,\mathrm{d}V\,,\end{aligned} \tag{6.7}$$

where N_{Ω_R} is the number of elements in the reservoir region (subdomain Ω_R) and N_{Ω_t} is the number of elements in the entire model (domain Ω_t). In this equation, the terms referring to the pore pressure variation $(\Delta p_{\mathrm{f}}^i)$ and Biot coefficient (α^i) are constants within each element.

Peres et al. (2021) solve Eq. (6.7) using an iterative fixed-point method, in which the displacement field of iteration ζ is used to calculate the strains $\{\varepsilon^j\}$ of iteration $\zeta+1$. The displacement field of the initial iteration is determined considering only the summation in the subdomain Ω_R and the convergence of the method is based square root of the sum of the squared nodal displacement components over the domain Ω_t. As demonstrated in Chapter 5, this iterative method has limitations related to convergence, values of the mechanical properties of the materials, and computational performance. As a result, the authors proposed a non-iterative numerical scheme capable of expanding the applicability and improving the computational performance of the GFA.

An iterative fixed-point method, similar to that proposed by Peres et al. (2021), is used in the original version of the Green-FOSM method by Mesquita et al. (2023). However, despite the original method being up to 30 times faster (problem with 1,500 random variables) than the MCS, the iterative Green-FOSM method also has the same limitations mentioned in Chapter 5. Furthermore, it is computationally infeasible when the problem to be analyzed has more than 3,000 random variables (considering the following computing resources: workstation with an Intel Core i9-10850K processor and 64 Gb of RAM). Due to this, a non-iterative version of the Green-FOSM method is proposed. This new version aims to expand the applicability of the Green-FOSM method (application to problems with more than 10,000 random variables) and, at the same time, to improve its CPU time.

6.3.1. FOSM based on non-iterative Green's function approach

Using the Eq. (6.7) it is possible to deterministically calculate the displacements produced by pore pressure variations. As presented by Mesquita et al. (2023), the GFA can be statistically extended in order to incorporate the uncertainties related to the mechanical properties of the rocks that make up the geological formation. This extension is done using statistical methods that are able to propagate the uncertainty of the random input variables (in this case, the mechanical properties of the rocks) to the random variables that represent the answer to the problem (displacement, strain, and stress fields).

According to Fenton and Griffiths (2008), statistical methods of uncertainty propagation can be exact or approximate. When the relationship between input and output random variables is represented by a complex mathematical function, such as Eq. (6.7), the exact method becomes unfeasible. In this case, approximate methods such as Monte Carlo Simulation (MCS) and FOSM method can be used. Mesquita et al. (2023) use the FOSM method to statistically expand GFA.

In the FOSM method, the mean values $\mathrm{E}\left[\tilde{Y}\left(\tilde{X}_N\right)\right]$ and variances $\mathrm{Var}\left[\tilde{Y}\left(\tilde{X}_N\right)\right]$ of the response random variables $\left(\tilde{Y}_N\right)$ are determined through the first terms of the Taylor series expansion centered on the mean values $\left(\mu_{\tilde{X}_N}\right)$ of the N random input variables $\left(\tilde{X}_N\right)$ as shown in the following

$$\mathrm{E}\left[\tilde{Y}\left(\tilde{X}_1, \tilde{X}_2, \dots, \tilde{X}_N\right)\right] \approx \mathrm{g}\left(\mu_{\tilde{X}_1}, \mu_{\tilde{X}_2}, \dots, \mu_{\tilde{X}_N}\right), \qquad \text{and} \tag{6.8}$$

$$\begin{aligned}&\mathrm{Var}\left[\tilde{Y}\left(\tilde{X}_1,\tilde{X}_2,\dots,\tilde{X}_N\right)\right]\\&\approx\sum_{m=1}^{N}\sum_{n=1}^{N}\left(\frac{\partial \mathrm{g}\left(\mu_{\tilde{X}_1},\mu_{\tilde{X}_2},\dots,\mu_{\tilde{X}_N}\right)}{\partial\tilde{X}_m}\right)\left(\frac{\partial \mathrm{g}\left(\mu_{\tilde{X}_1},\dots,\mu_{\tilde{X}_N}\right)}{\partial\tilde{X}_n}\right)\rho_{mn}\sigma_m\sigma_n.\end{aligned}\tag{6.9}$$

Where μ_i is the mean value of random variable i, σ_i is the standard deviation of random variable i, and ρ_{ij} is the correlation coefficient between random variables i and j (ANG; TANG, 2015). Compared to MCS, the great advantage of the FOSM method is associated with the CPU time required to obtain the statistical answer to the problem.

6.3.1.1. First moment using non-iterative Green's function approach

As shown in Eq. (6.8), in the FOSM method the mean values of the output random variables $(\tilde{Y}_N)$ are determined from the function $\mathrm{g}(\mu_{\tilde{X}_N})$ and the mean values of the input random variables $(\tilde{X}_N)$. By extending the GFA to the statistical case, the function $\mathrm{g}(\mu_{\tilde{X}_N})$ is defined by Eq. (6.7). In this way, the mean values of the variables $(\tilde{Y}_N)$ can be obtained directly using the non-iterative numerical scheme proposed in Chapter 5. In this scheme, the strain vector $\{\varepsilon^j\}$ is rewritten using a matrix $[\mathcal{B}^j(\underline{x})]$, formed by the derivatives of shape functions, which correlate the nodal displacements $\{u(\underline{X})\}^T\{e_\beta\}$ with this strain vector, as it is classically done in the finite-element literature.

The first summation shown in Eq. (6.7) corresponds to the energy $\{E_\Theta\}$ generated by the volumetric deformation of the elements contained in the reservoir region, which is statistically represented by the $2n\times 1$ dimension vector shown below

$$\{E_{\Theta}(\mu_{\tilde{\alpha}},\mu_{\tilde{E}_{\mathrm{inf}}},\mu_{\tilde{\nu}_{\mathrm{inf}}})\} = \begin{Bmatrix} \sum_{i=1}^{N_{\Omega_R}} \mu_{\tilde{\alpha}}^{i}\,\Delta p_{\mathrm{f}}^{i} \int_{\Omega_R^i} \Theta_{F_x}^{i}(\underline{x},\underline{X}_1,\mu_{\tilde{E}_{\mathrm{inf}}},\mu_{\tilde{\nu}_{\mathrm{inf}}})\,\mathrm{d}V \\ \sum_{i=1}^{N_{\Omega_R}} \mu_{\tilde{\alpha}}^{i}\,\Delta p_{\mathrm{f}}^{i} \int_{\Omega_R^i} \Theta_{F_y}^{i}(\underline{x},\underline{X}_1,\mu_{\tilde{E}_{\mathrm{inf}}},\mu_{\tilde{\nu}_{\mathrm{inf}}})\,\mathrm{d}V \\ \vdots \\ \sum_{i=1}^{N_{\Omega_R}} \mu_{\tilde{\alpha}}^{i}\,\Delta p_{\mathrm{f}}^{i} \int_{\Omega_R^i} \Theta_{F_x}^{i}(\underline{x},\underline{X}_n,\mu_{\tilde{E}_{\mathrm{inf}}},\mu_{\tilde{\nu}_{\mathrm{inf}}})\,\mathrm{d}V \\ \sum_{i=1}^{N_{\Omega_R}} \mu_{\tilde{\alpha}}^{i}\,\Delta p_{\mathrm{f}}^{i} \int_{\Omega_R^i} \Theta_{F_y}^{i}(\underline{x},\underline{X}_n,\mu_{\tilde{E}_{\mathrm{inf}}},\mu_{\tilde{\nu}_{\mathrm{inf}}})\,\mathrm{d}V \end{Bmatrix}, \tag{6.10}$$

where n is the number of nodes in the element mesh, N is the number of random variables in the problem, Θ_{β}^{i} is the volumetric deformation do the triangular element i generated by a concentrated horizontal (β equal to the horizontal force F_x) or vertical (β equal to the vertical force F_y) force applied at position $\underline{X}_n$, and $\mu_{\tilde{\alpha}}^{i}$, $\mu_{\tilde{E}_{\mathrm{inf}}}$ and $\mu_{\tilde{\nu}_{\mathrm{inf}}}$ are the mean values of the random variables that represents the Biot coefficient, Young's modulus, and Poisson's ratio in triangular element i, respectively.

The second summation of Eq. (6.7) represents the portion of complementary energy $\{\bar{E}_{\mathrm{c}}\}$ generated by the difference between the mean values of the input random variables of the real problem and the random variables of the auxiliary problem. At the element level, this energy portion can be written using the $2n \times 1$ follows

$$\{\bar{E}_{\mathrm{c}}(\mu_{\tilde{X}_1},\dots,\mu_{\tilde{X}_N})\} = \begin{Bmatrix} \sum_{j=1}^{N_{\Omega_t}} \left\{f_{c\beta}^{j}(\underline{X}_n,\mu_{\tilde{E}_{\mathrm{inf}}},\mu_{\tilde{\nu}_{\mathrm{inf}}},\mu_{\tilde{E}}^{j},\mu_{\tilde{\nu}}^{j})\right\}^T \{\tilde{u}^j\} \\ \sum_{j=1}^{N_{\Omega_t}} \left\{f_{c\beta}^{j}(\underline{X}_n,\mu_{\tilde{E}_{\mathrm{inf}}},\mu_{\tilde{\nu}_{\mathrm{inf}}},\mu_{\tilde{E}}^{j},\mu_{\tilde{\nu}}^{j})\right\}^T \{\tilde{u}^j\} \\ \vdots \\ \sum_{j=1}^{N_{\Omega_t}} \left\{f_{c\beta}^{j}(\underline{X}_n,\mu_{\tilde{E}_{\mathrm{inf}}},\mu_{\tilde{\nu}_{\mathrm{inf}}},\mu_{\tilde{E}}^{j},\mu_{\tilde{\nu}}^{j})\right\}^T \{\tilde{u}^j\} \\ \sum_{j=1}^{N_{\Omega_t}} \left\{f_{c\beta}^{j}(\underline{X}_n,\mu_{\tilde{E}_{\mathrm{inf}}},\mu_{\tilde{\nu}_{\mathrm{inf}}},\mu_{\tilde{E}}^{j},\mu_{\tilde{\nu}}^{j})\right\}^T \{\tilde{u}^j\} \end{Bmatrix}. \tag{6.11}$$

The vector $\left\{f_{c\beta}^{j}(\underline{X}_n,\mu_{\tilde{E}_{\mathrm{inf}}},\mu_{\tilde{\nu}_{\mathrm{inf}}},\mu_{\tilde{E}}^{j},\mu_{\tilde{\nu}}^{j})\right\}$ is defined by

$$\left\{f_{c\beta}^{j}\left(\underline{X}_{n},\mu_{\tilde{E}_{\mathrm{inf}}},\mu_{\tilde{\nu}_{\mathrm{inf}}},\mu_{\tilde{E}}^{j},\mu_{\tilde{\nu}}^{j}\right)\right\}^{T}$$

$$= \int_{\Omega_t^j} \left\{\varepsilon_{\beta}\left(\underline{x},\underline{X}_{n},\mu_{\tilde{E}_{\mathrm{inf}}},\mu_{\tilde{\nu}_{\mathrm{inf}}}\right)\right\}^{T}\left[\mathbb{C}^{\mathrm{e}}\left(\mu_{\tilde{E}_{\mathrm{inf}}},\mu_{\tilde{\nu}_{\mathrm{inf}}}\right) - \mathbb{C}^{j}\left(\underline{x},\mu_{\tilde{E}}^{j},\mu_{\tilde{\nu}}^{j}\right)\right]\left[\mathcal{B}^{j}\left(\underline{x}\right)\right] \mathrm{d}V\,, \tag{6.12}$$

where $\left[\mathcal{B}^{j}\left(\underline{x}\right)\right]$ is the matrix formed by the derivatives of shape functions and $\mu_{\tilde{X}_N}$ are the mean values of input random variables that make up the matrix $[\mathbb{C}^{j}]$, that is, Young's modulus $\tilde{E}$ and Poisson's coefficient $\tilde{\nu}$ of each triangular element j. Considering the connectivity of the triangular elements used to discretize the domain Ω_t and assuming that the output random variables that represent the nodal displacements are written in terms of global vector

$$\left\{\widetilde{U}\left(\mu_{\tilde{X}_1},\dots,\mu_{\tilde{X}_N}\right)\right\} = \begin{Bmatrix} \left\{\tilde{u}\left(\underline{X}_1,\mu_{\tilde{X}_1},\dots,\mu_{\tilde{X}_N}\right)\right\}^{T}\left\{e_{F_x}\right\} \\ \left\{\tilde{u}\left(\underline{X}_1,\mu_{\tilde{X}_1},\dots,\mu_{\tilde{X}_N}\right)\right\}^{T}\left\{e_{F_y}\right\} \\ \vdots \\ \left\{\tilde{u}\left(\underline{X}_n,\mu_{\tilde{X}_1},\dots,\mu_{\tilde{X}_N}\right)\right\}^{T}\left\{e_{F_x}\right\} \\ \left\{\tilde{u}\left(\underline{X}_n,\mu_{\tilde{X}_1},\dots,\mu_{\tilde{X}_N}\right)\right\}^{T}\left\{e_{F_y}\right\} \end{Bmatrix}, \tag{6.13}$$

the Eq. (6.11) can be rewritten as

$$\left\{E_{\mathrm{c}}\left(\mu_{\tilde{X}_1},\dots,\mu_{\tilde{X}_N}\right)\right\} = \left[F_c\left(\mu_{\tilde{X}_1},\dots,\mu_{\tilde{X}_N}\right)\right]\left\{\widetilde{U}\left(\mu_{\tilde{X}_1},\dots,\mu_{\tilde{X}_N}\right)\right\}, \tag{6.14}$$

where $\left[F_c\left(\mu_{\tilde{X}_1},\dots,\mu_{\tilde{X}_N}\right)\right]$ is a matrix with dimension $2n \times 2n$.

Using the vectors $\{\widetilde{U}(\mu_{\tilde{X}_1},\dots,\mu_{\tilde{X}_N})\}$ and $\left\{E_{\Theta}\left(\mu_{\tilde{\alpha}},\mu_{\tilde{E}_{\mathrm{inf}}},\mu_{\tilde{\nu}_{\mathrm{inf}}}\right)\right\}$, and the definition of $\left\{E_{\mathrm{c}}\left(\mu_{\tilde{X}_1},\dots,\mu_{\tilde{X}_N}\right)\right\}$, the mean values of the nodal displacements can be approximated by

$$\begin{aligned}\mathbb{E}\left[\widetilde{U}\left(\tilde{X}_1,\tilde{X}_2,\dots,\tilde{X}_N\right)\right] &\approx \left\{\widetilde{U}\left(\mu_{\tilde{X}_1},\dots,\mu_{\tilde{X}_N}\right)\right\} \\ &= \left([\mathbb{I}] - \left[F_c\left(\mu_{\tilde{X}_1},\dots,\mu_{\tilde{X}_N}\right)\right]\right)^{-1}\left\{E_{\Theta}\left(\mu_{\tilde{\alpha}},\mu_{\tilde{E}_{\mathrm{inf}}},\mu_{\tilde{\nu}_{\mathrm{inf}}}\right)\right\},\end{aligned} \tag{6.15}$$

where $[\mathbb{I}]$ is the second order identity matrix.

6.3.1.2.
Second moment using non-iterative Green's function approach

As shown in Eq. (6.9), in the FOSM method the variances of the output random variables $\left(\tilde{Y}_N\right)$ are determined from the partial derivatives of function $\mathrm{g}\left(\mu_{\tilde{X}_N}\right)$ in relation to the input random variables $\left(\tilde{X}_N\right)$. As previously mentioned, the function $\mathrm{g}(\mu_{\tilde{X}_N})$ is defined by Eq. (6.7). In this way, the derivatives with respect to N input random variables $(\tilde{X}_N)$ can be calculated as

$$\begin{aligned}&\left\{\frac{\partial U(\mu_{\tilde{X}_1},\dots,\mu_{\tilde{X}_N})}{\partial(\tilde{X}_1,\dots,\tilde{X}_N)}\right\}\\&\qquad=\left([\mathbb{I}]-[F_{\mathrm{c}}(\mu_{\tilde{X}_1},\dots,\mu_{\tilde{X}_N})]\right)^{-1}\left(\left\{\frac{\partial E_{\theta}(\mu_{\tilde{X}_1},\dots,\mu_{\tilde{X}_N})}{\partial(\tilde{X}_1,\dots,\tilde{X}_N)}\right\}\right.\\&\qquad\left.+\left[\frac{\partial F_{\mathrm{c}}(\mu_{\tilde{X}_1},\dots,\mu_{\tilde{X}_N})}{\partial(\tilde{X}_1,\dots,\tilde{X}_N)}\right]\{U(\mu_{\tilde{X}_1},\dots,\mu_{\tilde{X}_N})\}\right).\end{aligned} \tag{6.16}$$

The terms $\left([\mathbb{I}]-[F_{\mathrm{c}}(\mu_{\tilde{X}_1},\dots,\mu_{\tilde{X}_N})]\right)^{-1}$ and $\{U(\mu_{\tilde{X}_1},\dots,\mu_{\tilde{X}_N})\}$ are obtained during the calculation process of the mean values shown in Eq. (6.15). Using the partial derivatives of the nodal displacements with respect to the input random variables $(\tilde{X}_N)$, the variance of the horizontal ($\kappa=1$) or vertical ($\kappa=1$) displacements at position $\underline{X}_n$ is given by

$$\begin{aligned}&\mathrm{Var}[\tilde{U}_{\kappa}(\underline{X}_n,\tilde{X}_1,\tilde{X}_2,\dots,\tilde{X}_N)]\\&=\left\{\mathbb{D}_{\kappa}^{(n)}(\mu_{\tilde{X}_1},\dots,\mu_{\tilde{X}_N})\right\}^{\mathrm{T}}[\mathbb{S}(\rho_{\tilde{X}_N},\sigma_{\tilde{X}_N})]\left\{\mathbb{D}_{\kappa}^{(n)}(\mu_{\tilde{X}_1},\dots,\mu_{\tilde{X}_N})\right\},\end{aligned} \tag{6.17}$$

where $\left\{\mathbb{D}_{\kappa}^{(n)}(\mu_{\tilde{X}_1},\dots,\mu_{\tilde{X}_N})\right\}$ is a vector of dimension $N\times 1$ that contain the partial derivatives,

$$\left\{\mathbb{D}_{\kappa}^{(n)}(\mu_{\tilde{X}_1},\dots,\mu_{\tilde{X}_N})\right\}=\begin{Bmatrix}\dfrac{\partial\tilde{U}_{\kappa}(\underline{X}_n,\mu_{\tilde{X}_1},\dots,\mu_{\tilde{X}_N})}{\partial\tilde{X}_1}\\\dfrac{\partial\tilde{U}_{\kappa}(\underline{X}_n,\mu_{\tilde{X}_1},\dots,\mu_{\tilde{X}_N})}{\partial\tilde{X}_2}\\\vdots\\\dfrac{\partial\tilde{U}_{\kappa}(\underline{X}_n,\mu_{\tilde{X}_1},\dots,\mu_{\tilde{X}_N})}{\partial\tilde{X}_m}\end{Bmatrix},\quad\text{and} \tag{6.18}$$

$\mathbb{S}(\rho_{\tilde{X}_N},\sigma_{\tilde{X}_N})$ is the matrix that considers the spatial variability of input random variables that represent the mechanical properties of materials, as discussed in the next section.

6.3.2. Random variables, stochastic grid, and spatial variability of properties

Due to their inherent spatial variability, the mechanical properties of the rocks that make up the geological formation can be treated as random variables

(VANMARCKE, 2010). This variability is incorporated into the geomechanical problem through a stochastic random field, which is delimited by the domain Ω_t. As proposed by Cho (2012) and Li et al. (2015), the domain Ω_t is discretized into several subdomains Ω_i forming a stochastic grid in which the input random variables $(\tilde{X}_N)$ are considered statistically stationary, that is, the mean values and variances remain constant within the same geological layer, and an autocorrelation function defines the degree of correlation between random variables of any two subdomains Ω_i, regardless of their absolute coordinates. In this work, the correlation between random variables of subdomains Ω_i contained in different geological layers and the cross correlation between random variables that represents different mechanical properties are assumed equal to zero. Defining $\rho\left(\tau_{x_{pq}}, \tau_{y_{pq}}\right)$ as the autocorrelation function between the random variables of the subdomains Ω_p and Ω_q, respectively, the matrix $\mathbb{S}(\rho_{\tilde{X}_N}, \sigma_{\tilde{X}_N})$ is defined by

$$\begin{aligned}&\mathbb{S}(\rho_{\tilde{X}_N}, \sigma_{\tilde{X}_N})\\ &= \begin{bmatrix} \sigma_{\tilde{X}_1}\sigma_{\tilde{X}_1} & \rho(\tau_{x_{12}}, \tau_{y_{12}})\,\sigma_{\tilde{X}_1}\sigma_{\tilde{X}_2} & \cdots & \rho\left(\tau_{x_{1q}}, \tau_{y_{1q}}\right)\,\sigma_{\tilde{X}_1}\sigma_{\tilde{X}_q} \\ \rho(\tau_{x_{21}}, \tau_{y_{21}})\,\sigma_{\tilde{X}_2}\sigma_{\tilde{X}_1} & \sigma_{\tilde{X}_2}\sigma_{\tilde{X}_2} & \cdots & \rho\left(\tau_{x_{2q}}, \tau_{y_{2q}}\right)\,\sigma_{\tilde{X}_2}\sigma_{\tilde{X}_q} \\ \vdots & \vdots & \ddots & \vdots \\ \rho\left(\tau_{x_{p1}}, \tau_{y_{p1}}\right)\,\sigma_{\tilde{X}_p}\sigma_{\tilde{X}_1} & \rho\left(\tau_{x_{p2}}, \tau_{y_{p2}}\right)\,\sigma_{\tilde{X}_p}\sigma_{\tilde{X}_2} & \cdots & \rho\left(\tau_{x_{pq}}, \tau_{y_{pq}}\right)\,\sigma_{\tilde{X}_p}\sigma_{\tilde{X}_q} \end{bmatrix},\end{aligned} \tag{6.19}$$

where $\sigma_{\tilde{X}_p}$ and $\sigma_{\tilde{X}_q}$ are the standard deviations of the random variables $\tilde{X}_p$ and $\tilde{X}_q$. The autocorrelation function varies between 0.0 and 1.0 (LI et al., 2015). When $\rho\left(\tau_{x_{pq}}, \tau_{y_{pq}}\right)$ is equal to 1.0, the random variables of the domains Ω_p and Ω_q assume equal values. Otherwise, these variables assume different values. The mechanical properties of materials are considered homogeneous when all the relationships between the Ω_p and Ω_q subdomains of the same geological layer are equal to 1.0. On the other hand, when this ratio is different from 1.0, the materials are considered heterogeneous. In general, to define the autocorrelation function between the random variables of a geological layer, a large dataset is needed, which are not always available. As a result, the theoretical equations presented by Li et al. (2015) are commonly used in statistical analysis of geotechnical problems.

In the applications presented in the following sections, the mesh of triangular elements used to discretize the domain Ω_t in the geomechanical analysis is used to define the subdomains Ω_i of the stochastic grid. For each triangular element, three random variables are admitted, which represent Young's modulus, Poisson's ratio, and the Biot coefficient. In addition to these random variables, three more random variables are considered to represent the mechanical properties of the infinite medium. Therefore, the total number of random variables N is equal to $3(N_{\Omega_t} + 1)$.

6.4.
Validation study: Reservoir under uniform depletion

The non-iterative Green-FOSM method is validated using the geological profile shown in Figure 6.2. This section is composed of three rock layers (overburden, reservoir, and underburden) with different mechanical properties. The uncertainties associated with the mechanical parameters of the rock (Young's modulus, Poisson's ratio, and Biot coefficient) are propagated to the output random variables (nodal displacements) using the non-iterative Green-FOSM method and the MCS. The MCS is adopted to generate the "reference" solutions used to validate the proposed methodology, as has been done in other works (LÖFMAN; KORKIALA-TANTTU, 2021; QI et al., 2022; WU et al., 2021).

In this application, the problem domain (Ω_t) is divided into 608 sub-regions, which form the mesh of triangular elements of the geomechanical analysis and the stochastic grid of the statistical analysis. This number of divisions was defined through a sensitivity analysis and represents the maximum number of sub-regions for which the MCS is computationally feasible considering the computational resources available (workstation with an Intel Core i9-10850K processor and 64 Gb of RAM). The reservoir region (subdomain Ω_R) is subjected to a uniform fluid extraction process in which the pore pressure variation (Δp_{f}) is equal to -20 MPa.

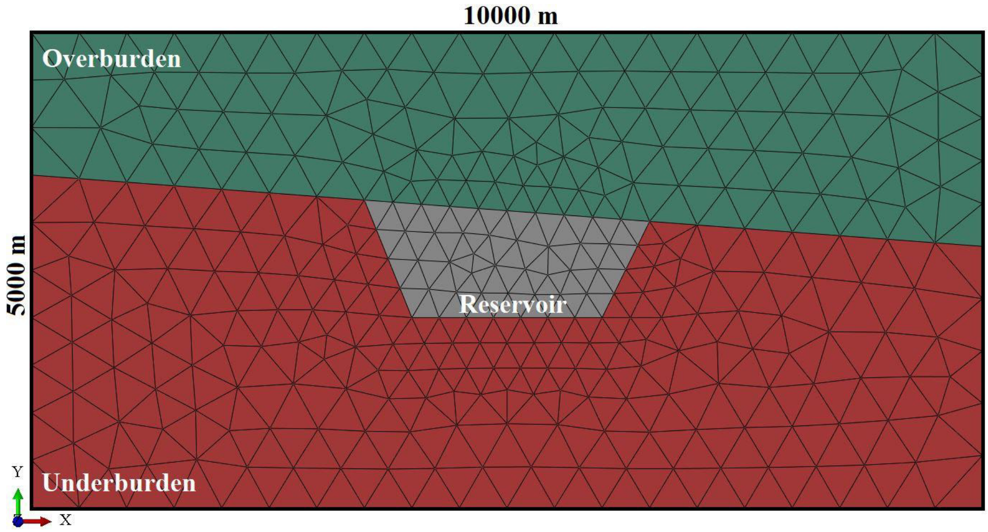

Figure 6.2. 2D model (plane strain state) used to represent the geological formation.

In the MCS, the statistical moments of the nodal displacements are determined after 3000 repetitions, performed using the deterministic and non-iterative GFA presented in Chapter 5. In addition, it is also necessary to know the probability density function that describes the input random variables. In this work, the random variables that represent Young's modulus and Poisson's ratio are described using a normal distribution function (JHA et al., 2015; PLÚA et al., 2021a, 2021b). The random variables that represent the Biot coefficient are defined by a uniform distribution function (PLÚA et al., 2021a, 2021b).

In all analyses, the integrals of Eq. (6.10) and Eq. (6.12) are numerically solved using Gauss quadrature (4×4 points), Bartholomew quadrature (level 3), and Duffy transformation, similarly to Peres et al. (2021), and Mesquita et al. (2023).

6.4.1. Validation regarding the spatial variability of the mechanical parameters of the rocks

In order to evaluate the effectiveness of the non-iterative Green-FOSM method with respect to the spatial variability of the input random variables, the example presented in this section is analyzed assuming three situations. In the first situation, the input random variables (with the same nature and belonging to the same geological layer) of the subdomains Ω_p and Ω_q are admitted as fully correlated. In the second situation, these random variables are assumed to be totally uncorrelated. In the last situation, these input random variables are correlated through the exponential autocorrelation function in Eq. (6.20), which equation is used in geotechnical problem by Cho (2012), Wang et al. (2020), and Wu et al. (2021).

$$\rho\left(\tau_{x_{pq}}, \tau_{y_{pq}}\right) = \exp\left(-\frac{\tau_{x_{pq}}}{l_h} - \frac{\tau_{y_{pq}}}{l_v}\right) \qquad (6.20)$$

The parameters $\tau_{x_{pq}}$ and $\tau_{y_{pq}}$ are the absolute distances between the centroids of the subdomains Ω_p e Ω_q in the horizontal and vertical directions, respectively. The parameters l_h and l_v are the horizontal and vertical correlation lengths, respectively. In this example, the horizontal correlation length is equal to 1,000 meters and the vertical correlation length is equal to 200 meters. In this last situation, to obtain the reference responses via MCS, the random variables that represent Young's modulus and Poisson's ratio (input random variables defined by a normal density function) are generated using the Cholesky decomposition technique (LI et al., 2015; YANG; WANG; BRANDENBERG, 2022) and the random values representing the Biot coefficient (values generated from a uniform density function) are assumed to be fully correlated.

In the three situations described above, two coefficients of variation (CV) for the Young's modulus and for the Poisson's ratio are considered, 10% and 20%. For the Biot coefficient, the CV is taken 10% in all analysis, since CV's above 10% can result in Biot coefficients greater than 1.0, which have no real physical meaning. The set of all mechanical parameters used in this application are shown in Table 6.1.

Table 6.1. Mechanical parameters of the rock that form the geological profile used in this application.

Material Parameters						
	Young's modulus [GPa]		Poisson's ratio		Biot coefficient	
Layer	Mean	CV	Mean	CV	Mean	CV
Reservoir	15.0	10% - 20%	0.30	10% - 20%	0.80	10%
Overburden	6.0	10% - 20%	0.20	10% - 20%	-	-
Underburden	20.0	10% - 20%	0.25	10% - 20%	-	-
Infinite domain	20.0	10% - 20%	0.25	10% - 20%	-	-

In Figure 6.3 the relationships between the statistical moments of horizontal and vertical nodal displacements calculated using the non-iterative Green-FOSM method and MCS are presented, considering the CV equal to 10% and the three situations of spatial variability proposed. As can be seen, in general, the values obtained by the proposed method are close to the values found through MCS. In some nodes, it is observed that the mean value of the vertical displacement calculated by proposed method is up to 20% higher than the mean value found via MCS. This difference is justified by the magnitude of the vertical displacements in these nodes, which are close to zero, and can be reduced by increasing the number of repetitions in MCS.

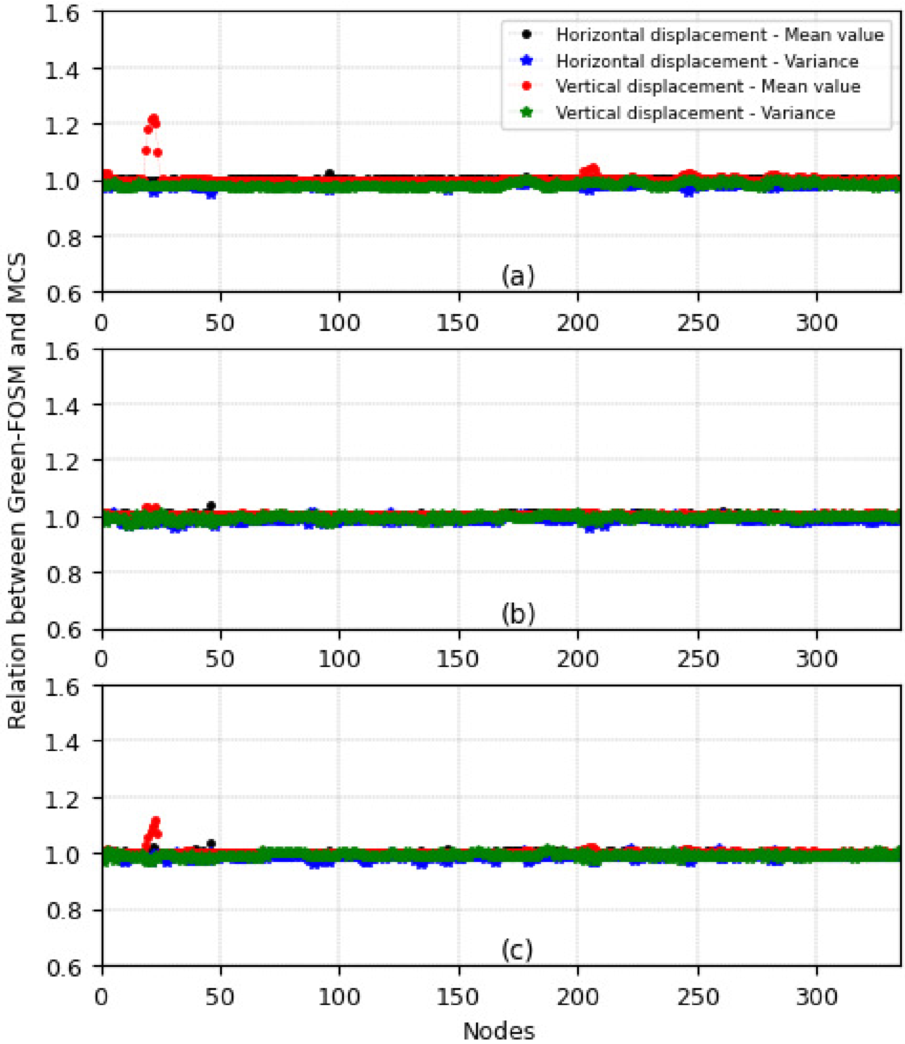

Figure 6.3. Relationships between the statistical moments obtained by the non-iterative Green-FOSM method and by MCS considering the CV equal to 10%. In (a) the random variables are fully correlated, in (b) the random variables are fully uncorrelated, and in (c) the random variables are correlated following the exponential function described in Eq. (6.20).

In Figure 6.4 the relationships between the results obtained via non-iterative Green-FOSM method and MCS with CV equal to 20% are presented. For this situation, the variances of the horizontal and vertical displacements present a greater dispersion compared to the case with CV equal to 10%. In the three cases of spatial variability analyzed, the mean values obtained by non-iterative Green-FOSM method are close to those found through MCS. On the other hand, the variances obtained by the proposed method are, on average, 5.5% (horizontal displacement) and 6.9% (vertical displacement) lower that the variances found via MCS for the fully correlated situation (Figure 6.4.a). For the totally uncorrelated situation (Figure 6.4.b) these values are 6.9% (horizontal displacement) and 9.7% (vertical displacement). For the situation whose random variables follow the exponential autocorrelation function (Figure 6.4.c) these values are 2.7% (horizontal displacement) and 2.8% (vertical displacement). Also, except for three nodes shown in Figure 6.4.c, the relationships between the variances found via Green-FOSM method and MCS are less 0.8.

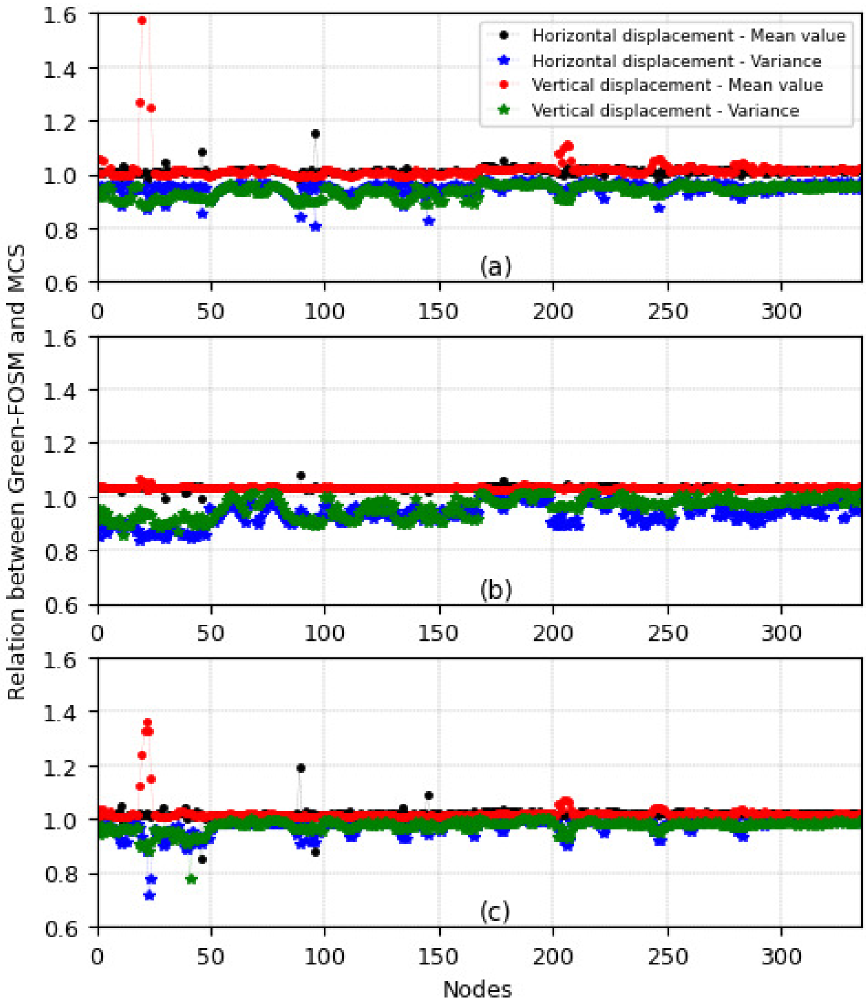

Figure 6.4. Relationships between the statistical moments obtained by the non-iterative Green-FOSM method and by MCS considering the CV equal to 20%. In (a) the random variables are fully correlated, in (b) the random variables are fully uncorrelated, and in (c) the random variables are correlated following the exponential function described in Eq. (6.20).

As verified by Bungenstab and Bicalho (2016), due to the truncation of the Taylor series, when increasing the CV of the input random variables, the FOSM method tends to underestimate the variances of the output random variables. Despite this, as already discussed by Mesquita et al. (2023), for the variability situations and the analyzed CV levels, the difference between the values obtained through the proposed method and by SMC are small in relation to the dimensions of the geomechanical problems. Thus, it can be concluded that for the analyzed situations, the non-iterative Green-FOSM method is able to obtain results compatible with those found by the MCS.

6.4.2. CPU time comparison

The computational performance of the proposed method is evaluated using a relative CPU time parameter calculated by the relation of the CPU times obtained by iterative Green-FOSM method or MCS and the proposed method. As shown in Figure 6.5, the relative CPU times are evaluated considering different meshes and, consequently, different numbers of random variables. In the case of the iterative Green-FOSM method, the maximum number of input random variables is 2,388, since the available computational resources (workstation with an Intel Core i9-10850K processor and 64 Gb of RAM) do not allow the analysis the problems with more random variables.

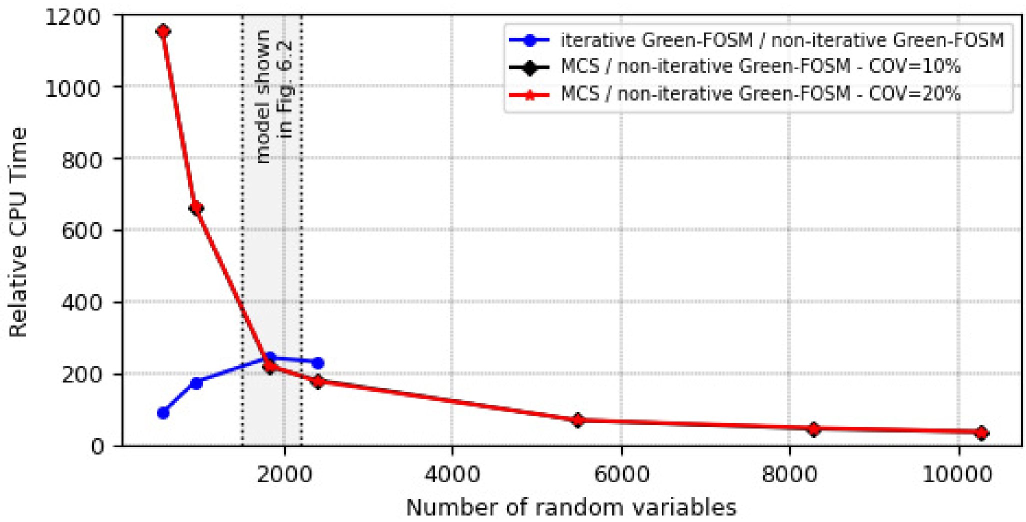

Figure 6.5. Relative CPU times as a function of the number of random variables in the model.

The results obtained show that the non-iterative Green-FOSM method is between 100 and 200 times faster than the iterative Green-FOSM method. Comparing the CPU times of the MCS and the proposed method, it is observed that the proposed method is at least 50 times faster than the MCS. Furthermore, using the same computational resources, with the proposed method it is possible to analyze problems with more than 10,000 random variables.

Despite sharing the same theoretical formulation, Eq. (6.7), in the iterative Green-FOSM method (MESQUITA et al., 2023) the mean values and partial derivatives are calculated $N + 1$ times in each interaction, where N is the number of random variables. In the non-iterative method, the partial derivatives are calculated from the mean values of the nodal displacements and the inverse matrix shown in Eq. (6.15), which is previously determined. As a result, in addition to eliminating iterations, the proposed method presents an additional performance gain, since it is not necessary to perform any additional matrix inversion.

6.5. Application: Uncertainties consideration in a Brazilian pre-salt reservoir

In order to demonstrate the applicability of the proposed method to real problems, the uncertainties related to the mechanical properties of materials are incorporated into the geomechanical analysis of the geological profile shown in Figure 6.6. This geological profile represents a typical section of the Brazilian pre-salt and is inspired by a seismic image of the Tupi field (Santos Basin, Brazil) found in Mohriak et al. (2012). The mean values of the mechanical properties of the rocks that make up the geological profile are presented in Figure 6.6. The problem domain (Ω_t domain) is divided into 3,642 sub-regions, which form the mesh of triangular elements of the geomechanical analysis and the stochastic grid of the statistical analysis, totaling 10,929 random variables. The reservoir region (subdomain Ω_R) is divided into two regions whose pore pressure variation are -80 MPa (depletion region) and 30 MPa (injection region). Melan's fundamental solution (MELAN, 1932) is used as an auxiliary problem. The mechanical properties of the infinite domain are the same as the underburden layer. The integrals in Eq. (6.10) and Eq. (6.12) are numerically solved using Gauss quadrature (4×4 points), Bartholomew quadrature (level 3), and Duffy transformation, as was done in Peres et al. (2021), and Mesquita et al. (2023).

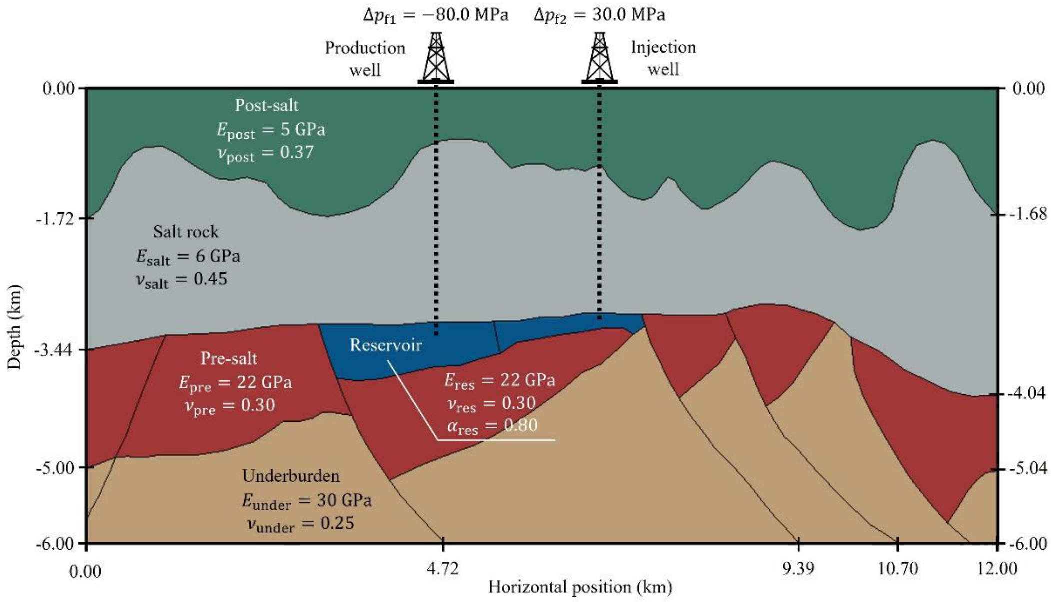

Figure 6.6. Representative 2D model of geological section of the Brazilian pre-salt field.

The random variables of the Ω_p and Ω_q subdomains, contained in the same geological layer, are correlated through the exponential autocorrelation function defined in Eq. (6.20), assuming the horizontal and vertical correlation lengths shown in Figure 6.7. Although Figure 6.7 uses as a reference a subdomain located in the salt rock layer, the correlation lengths shown in this figure are considered in the other geological layers. The CVs of the random variables that represent Young's modulus and Poisson's ratio are equal to 20%. For the Biot coefficient, a CV equal to 10% is used.

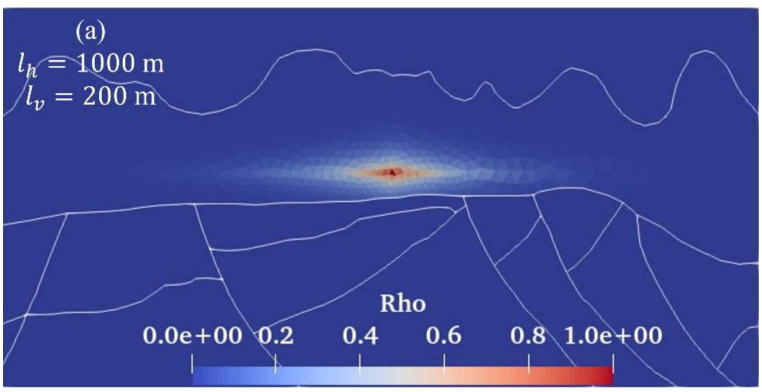

Figure 6.7. Correlation variation between a reference point Ω_p (located in the center of the layer) and the other subdomains Ω_q of the salt rock layer as a function of horizontal and vertical correlation lengths.

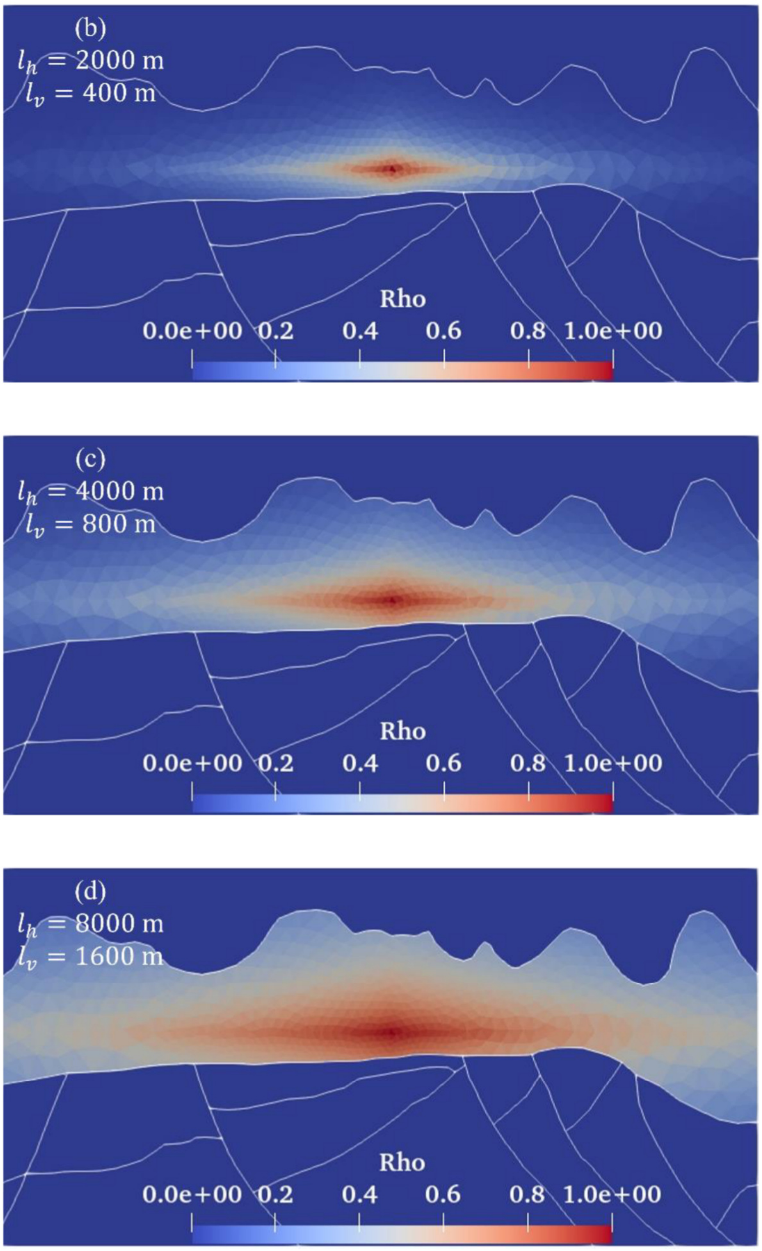

Figure 6.7. Correlation variation between a reference point Ω_p (located in the center of the layer) and the other subdomains Ω_q of the salt rock layer as a function of horizontal and vertical correlation lengths (continuation).

The obtained vertical displacement fields are presented next. These fields are obtained assuming that the output random variables are represented by a normal probability density function, as proposed by Mesquita et al. (2023). Figure 6.8.a shows the displacement field obtained by a deterministic process. Figure 6.8.b and Figure 6.8.c show the lower and upper limits of the interval with a confidence level of 95%, respectively, obtained through the analysis with the correlation lengths indicated in Figure 6.7.d.

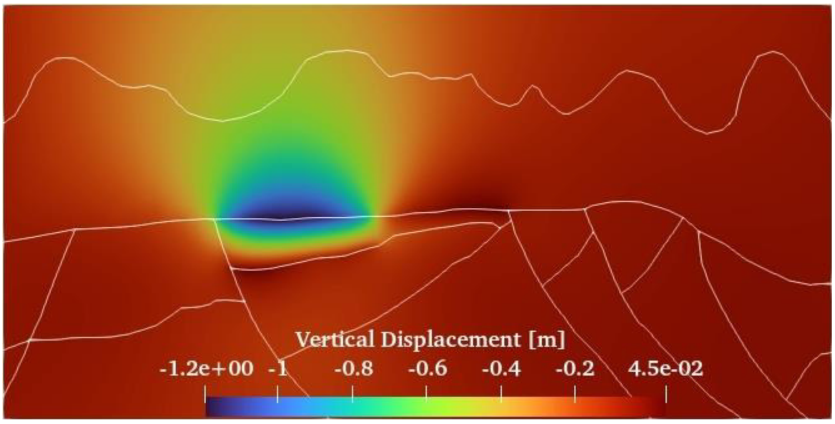

(a) Deterministic results (mean values)

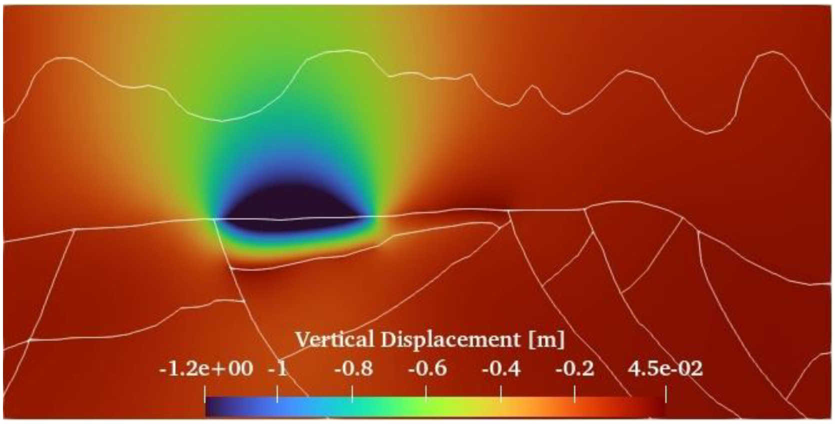

(b) Lower limit results

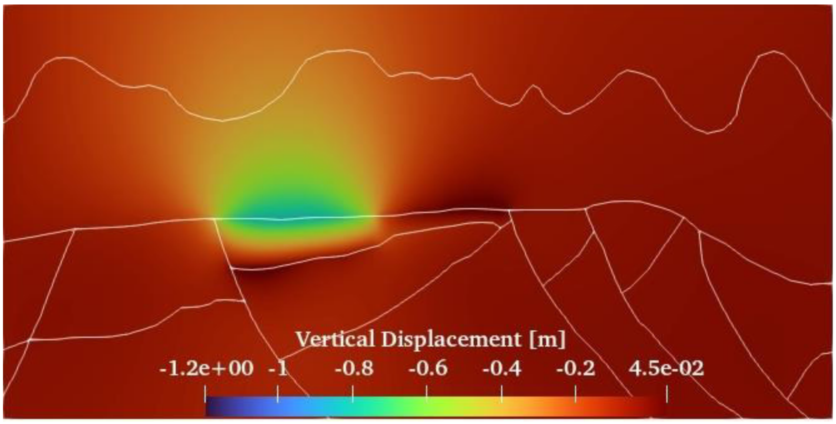

(c) Upper limit results

Figure 6.8. Vertical displacement fields obtained after the injection and depletion process shown in Figure 6.6. In (a) the deterministic results are shown, in (b) the displacements referring to the lower limit of the 95% confidence interval are shown, and in (c) the displacements referring to the upper limit of the 95% confidence interval are shown.

Analyzing these displacements fields, it is observed that the deterministic and statistical responses can be significantly different. The maximum vertical displacement obtained by the deterministic analysis is 1.20 meters. Considering the uncertainties and correlation lengths shown in Figure 6.7.a, this parameter can vary between 0.97 and 1.42 meters, which corresponds to ±18.5% of the deterministic value. Increasing the correlation lengths this percentage increases, being equal to ±24.0% for the lengths shown in Figure 6.7.b, ±28.1% for the lengths shown in Figure 6.7.c, and ±30.6% for the lengths shown in Figure 6.7.d.

Using seismic measurement results and geomechanical analysis it is possible to predict future events associated with the fluid injection or extraction process (HERWANGER; HORNE, 2009). This prediction is performed through the R-factor, which relates the vertical strains estimated by the geomechanical model with seismic velocity variations measured in the field (HATCHELL; BOURNE, 2005; RØSTE; STOVAS; LANDRØ, 2006). As shown in Figure 6.9, the statistical vertical strain fields differ from the deterministic strain field. This demonstrate that the uncertainties associated with the mechanical properties of rock must be considered when predicting future events associated with the fluid injection or extraction process.

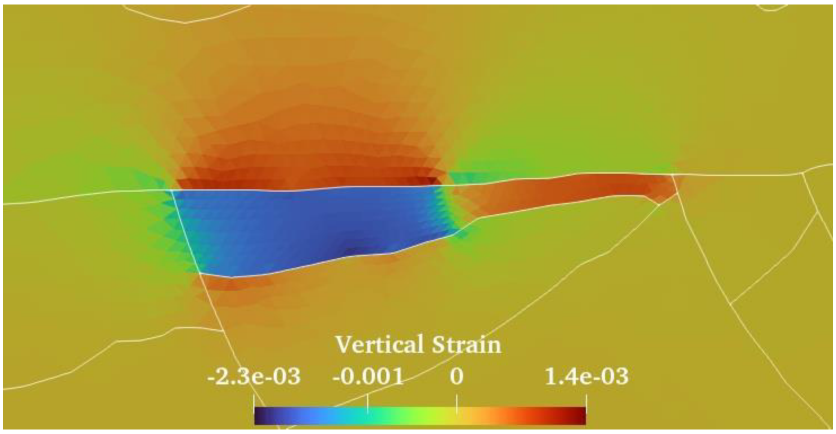

(a) Deterministic results (mean values)

Figure 6.9. Vertical strain fields obtained after the injection and depletion process shown in Figure 6.6. In (a) the deterministic results are shown, in (b) the displacements referring to the lower limit of the 95% confidence interval are shown, and in (c) the displacements referring to the upper limit of the 95% confidence interval are shown.

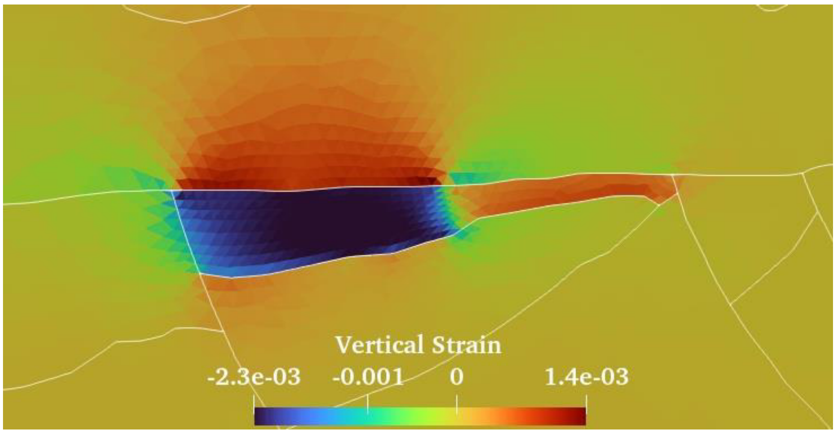

(b) Lower limit results

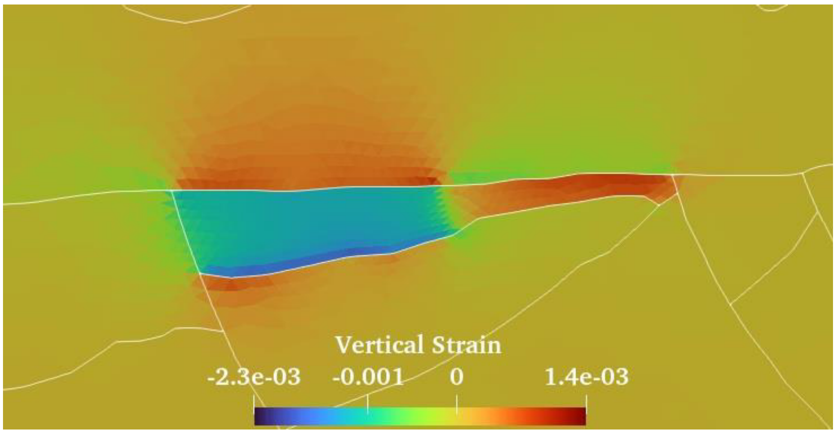

(c) Upper limit results

Figure 6.9. Vertical strain fields obtained after the injection and depletion process shown in Figure 6.6. In (a) the deterministic results are shown, in (b) the displacements referring to the lower limit of the 95% confidence interval are shown, and in (c) the displacements referring to the upper limit of the 95% confidence interval are shown (continuation).

In all analyzed situations, the maximum vertical compaction happens in the depletion reservoir region and the maximum vertical elongation occurs in the salt rock layer located above the reservoir. The maximum vertical compaction obtained from the deterministic analysis is equal to 2.02‰. However, depending on the uncertainties and correlation lengths shown in Figure 6.7 this strain can be 12.8%, 17.1%, 19.6%, or 20.7% greater or smaller than the deterministic value, respectively. For vertical elongation, the maximum deterministic value is equal to 1.21‰. However, due to uncertainties and correlation lengths shown in Figure 6.7 this value can be 19.4%, 23.1%, 26.3%, or 28.5% greater or smaller than the deterministic value.

Figure 6.10 shows the stress fields (maximum principal stresses) found from the deterministic analysis and statistical analysis considering the correlation lengths shown in Figure 6.7.d. Again, it is possible to verify that the statistical answer of the problem may differ from the deterministic answer. Through deterministic analysis, the maximum principal stress at the center of the depleted reservoir is equal to -30.7 MPa. However, depending on the uncertainties and correlation lengths this value can be up to 25.2% greater or smaller.

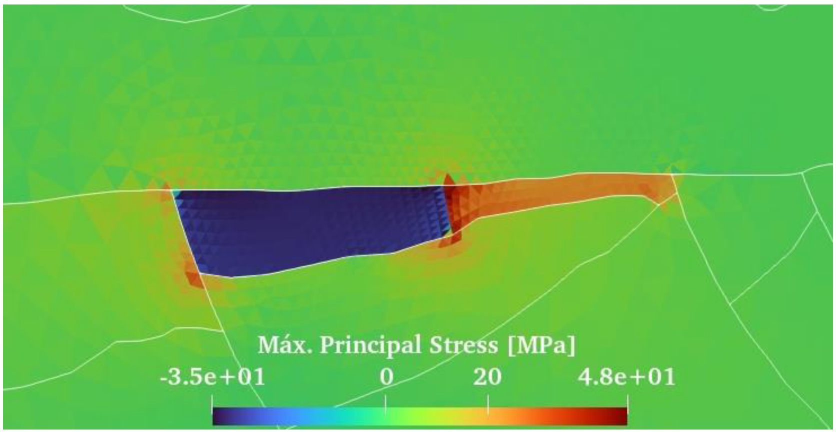

(a) Deterministic results (mean values)

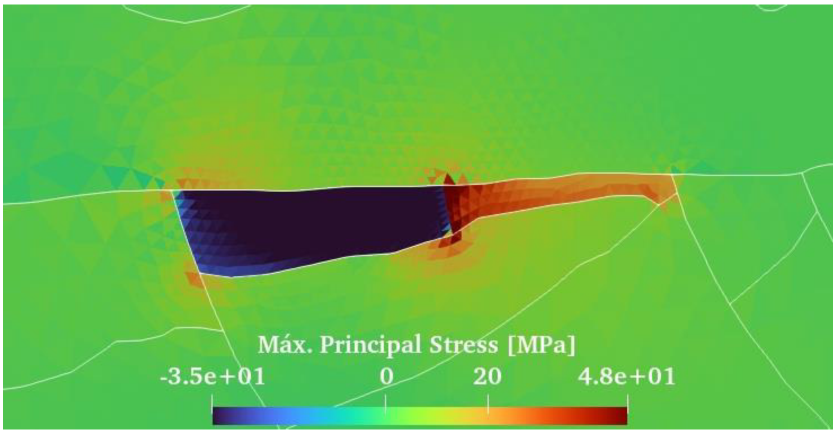

(b) Lower limit results

Figure 6.10. Stress field variations obtained after the injection and depletion process shown in Figure 6.6. In (a) the deterministic results are shown, in (b) the displacements referring to the lower limit of the 95% confidence interval are shown, and in (c) the displacements referring to the upper limit of the 95% confidence interval are shown.

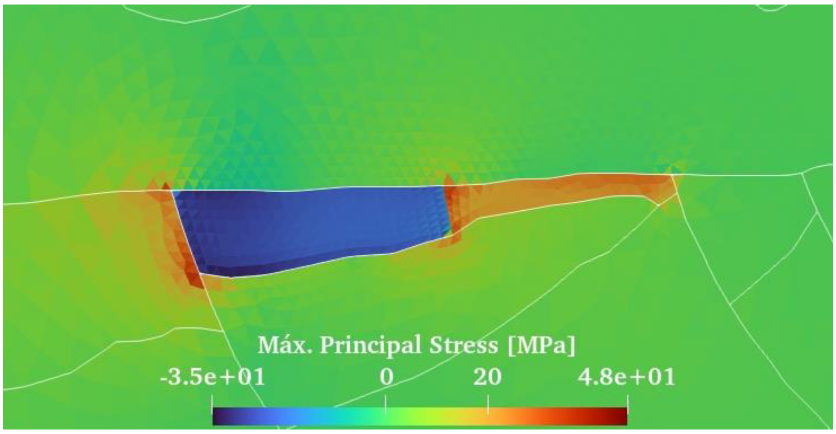

(c) Upper limit results

Figure 6.10. Stress field variations obtained after the injection and depletion process shown in Figure 6.6. In (a) the deterministic results are shown, in (b) the displacements referring to the lower limit of the 95% confidence interval are shown, and in (c) the displacements referring to the upper limit of the 95% confidence interval are shown. (continuation).

As demonstrated by other authors (JEANNE et al., 2016; PEREIRA et al., 2014a, 2014b; ZOCCARATO et al., 2019), the uncertainties associated with the fluid extraction or injection process produce variation in the stress state of geological faults, which are relevant for fault reactivation studies. Although these studies demonstrate the importance of considering uncertainties in fault reactivation analyses, they do not consider the spatial variability of input random variables. As demonstrated, the ranges of variation of the displacement, strain and stress fields are altered when the correlation lengths of the input random variables are modified, and this must be considered in the decision-making process in problems involving fluid extraction or injection process.

6.6. Conclusions and remarks

The Green-FOMS method (MESQUITA et al., 2023) is a stochastic statistical method capable of considering the uncertainties associated with the mechanical properties of materials in geomechanical problems. The novelty of the method lies in the use of the GFA, which, together with the FOSM method, is used to propagate these uncertainties to the displacement, strain, and stress fields of the geological formation. Furthermore, using the concepts of stochastic grid and autocorrelation function, the proposed method allows for the consideration of spatial variability of the random variables that represent these mechanical properties. Despite the fact that the original method presents satisfactory results when applied to hypothetical problems, when applied to real problems it has limitations. By using an iterative calculation scheme, the original Green-FOSM method presents a convergence problem when the relationship between the Young’s modulus of the rocks that make up the geological profile is greater than 100% or when the Poisson's ratio approaches 0.5. In addition, this iterative scheme jeopardizes the computational efficiency of the method and requires the storage of a large volume of data, which impede the analysis of problems with more than 3000 random variables (for the available computing resources, workstation with an Intel Core i9-10850K processor and 64 Gb of RAM).

The present work proposes a new version of the Green-FOSM method, which eliminates the iterative process and, simultaneously, solves the convergence problems related to the mechanical properties of the materials that make up the geological formation. As shown in Section 6.4.1, the present method is up to 200 times faster than the original method and, with the computational resources mentioned above, allows analyzing problems with more than 10,000 random variables.

The validity of the non-iterative Green-FOSM method is analyzed by comparing the statistical moments of the output random variables (horizontal and vertical displacements) obtained through this method with the results found via MCS (reference method). For this, a 2D model that represents a hypothetical geological formation with three layers of rocks with different mechanical properties is used. The spatial variability of the mechanical properties is incorporated into the geomechanical model using the exponential autocorrelation function shown in Eq. (6.20). In all evaluated situations, the results obtained by the proposed method present good agreement with the results found by the MCS. The CPU times of the geomechanical analyses performed using the proposed method demonstrate that, in the most unfavorable situation, this method is about 50 times faster than the MCS.

The applicability of the non-iterative Green-FOSM method and the importance of considering the uncertainties associated with the mechanical properties of materials in the geomechanical analysis are discussed using a geological section constructed from a seismic image inspired in the Tupi field, located in the Brazilian pre-salt. For the considered confidence level, the results obtained demonstrate that, due to these uncertainties, the displacement, deformation, and stress fields can assume values that differ considerably from the values found deterministically. Furthermore, it is demonstrated that, depending on the correlation lengths, the variation intervals of these fields can be up to 30.6% greater or smaller than the deterministic results. Despite the large amounts of data required, it is important to estimate correlation lengths accurately. For this, the studies of Uzielli et al. (2005) and Lloret-Cabot et al. (2014) developed in the geotechnical field can be used as references.

In general, the non-iterative Green-FOSM method achieves all the proposed objectives, since because its simplicity and efficiency it is capable of assisting reservoir engineers in decision-making process when evaluating problems related to the injection or depletion of fluids in underground reservoirs.

7
Summary, conclusions, and future work

This chapter provides an overview of the present work. The first section of this chapter presents a summary of the developed methodology, highlighting the advances obtained from the iterative version of the Green-FOSM method to the non-iterative version. Also in this section, the importance of considering uncertainties in geomechanical problems is emphasized and the main limitations of the proposed approach are presented. The second section of this chapter presents directions for future research.

7.1.
Summary and general conclusions

The present work proposes a computationally efficient statistical method, called the Green-FOSM method, to consider the inherent uncertainties associated with the mechanical properties of rocks in geomechanical analyses. Through this method it is possible to improve decision-making processes by analyzing the geomechanical problems generated by the production of oil and natural gas, water extraction or CO_2 storage. The main novelty of this method is the use of the Green's function approach, which together with the first-order second-moment statistical method, is used to propagate the uncertainties of the input random variables to the displacement, strain, and stress fields of the geological formation. Furthermore, using the concepts of stochastic grid and autocorrelation function, the proposed method allows the consideration of the spatial variability of random variables that represent these mechanical properties.

The first version of the Green-FOSM method uses the GFA formulation proposed by Peres et al. (2021). In this version the displacement field and the partial derivatives of the displacements with respect to the input random variables are calculated using an iterative calculation scheme (Figure 4.1). However, due to this iterative process, this version presents convergence problems when the relationship between the Young's modulus of the rocks that form the geological profile is greater than two or when the Poisson's ratio of one of the rocks is close to 0.5. Despite being computationally efficient, when compared to the traditional Monte Carlo simulation, this iterative calculation process compromises the CPU time of the statistical analysis.

The above limitations are eliminated using the non-iterative calculation process shown in Chapter 5. In this process, the iterative calculation scheme is replaced by the resolution of the system described in Eq. (5.13). The CPU times obtained from the validation examples (Section 5.4.2) demonstrate that, in deterministic applications, the non-iterative GFA is between 2.5 and 17.5 times faster than the iterative GFA (Figure 5.6). In the statistical case (Figure 6.5), the non-iterative Green-FOSM method is more than 200 times (model shown in Figure 6.2) faster than the iterative Green-FOSM method. Furthermore, using the non-iterative version it is possible to analyze problems with more than 10,000 random variables. Considering the same computational resources (workstation with an Intel Core i9-10850K processor and 64 Gb of RAM), in the iterative version these analyses are limited to a maximum of 3000 random variables.

In Chapter 6 the non-iterative Green-FOSM method is used to analyze a geological profile constructed from a seismic image of the Brazilian pre-salt Tupi field, located in the Santos basin. The obtained results demonstrate the capability of the non-iterative Green-FOSM method and highlight the importance of considering the inherent uncertainties associated with the mechanical properties of materials in geomechanical problems. For the confidence level considered, the results obtained demonstrate that, due to these uncertainties, the displacement, strain, and stress fields can assume values that differ considerably from the values found deterministically. Furthermore, it is demonstrated that, depending on the correlation lengths, the ranges of variation of these fields can be up to 30.6% larger or smaller than the deterministic results.

In general, it can be concluded that the methodology proposed in this work fulfills all the objectives presented in Chapter 1. Thus, the proposed method is able to assist reservoir engineers in decision making when evaluating problems related to the injection or depletion of fluids in underground reservoirs.

7.2. Future research

The set of future research proposed from the developments presented in the present work can be divided into two groups, the first related to the deterministic Green's function approach (GFA) and the second related to the probabilistic analysis of geomechanical problems using the Green-FOSM method.

Regarding the deterministic GFA, the following study ideas are proposed: (1) to develop and to implement the GFA for the treatment of 3D geomechanical problems, using Mindlin's fundamental solution as an auxiliary solution; (2) to use parallel computing techniques to improve the computational performance of the GFA in 2D and 3D problems; (3) to implement constitutive models (non-linear elastic, plastic, viscoelastic or viscoplastic) that allow simulating the non-linear behavior of materials; (4) to perform the fluid-mechanical coupling using the GFA; and (5) to modify the GFA to be applied in geotechnical problems that involve the consideration of stresses in the soil, emphasizing the calculation of initial stresses in-situ.

Regarding the probabilistic analysis of geomechanical problems, the following points are proposed: (1) to analyze the possibility of extending the GFA to the statistical case using other uncertainty propagation methods (for example, the second-order second-moment method) in order to obtain the statistical response of the analysis when the coefficients of variation of the input random variables are greater than 20%; (2) to analyze the feasibility of using an exact statistical method (such as the method presented in Section 3.1.2) to obtain the p.d.f. of the output random variables; (3) to extend the Green-FOSM method to analyze reliability problems such as fault reactivation; (4) to verify the possibility of using other methods to consider the spatial variability of the mechanical properties of materials (for example, methods based on the spectral density function or variance function); and (5) to propose a methodology to obtain the statistical parameters of random input variables (mean value, variance, and spatial variability) using data from field measurements.

References

AHAMED, T.; DUAN, J. G.; JO, H. Flood-fragility analysis of instream bridges–consideration of flow hydraulics, geotechnical uncertainties, and variable scour depth. **Structure and Infrastructure Engineering**, v. 17, n. 11, p. 1494–1507, 2021.

AICHI, M. Land subsidence modelling for decision making on groundwater abstraction under emergency situation. **Proceedings of the International Association of Hydrological Sciences**, v. 382, p. 403–408, 2020.

ANG, A. H.; TANG, W. H. **Probability Concepts in Engineering: Emphasis on Applications in Civil & Environmental Engineering**. **John Wiley & Sons, Inc**, 2015. Disponível em: <https://www.dbpia.co.kr/Journal/articleDetail?nodeId=NODE07509332>

APOSTOLOPOULOU, M. et al. Estimating permeability in shales and other heterogeneous porous media: Deterministic vs. stochastic investigations. **International Journal of Coal Geology**, v. 205, n. October 2018, p. 140–154, 2019.

ASLETT, L. J. M.; COOLEN, F. P. A. **Uncertainty in Engineering : Introduction to Methods and Applications**. [s.l: s.n.].

ATKINSON, K.; FLORES, J. The discrete collocation method for nonlinear integral equations. **IMA Journal of Numerical Analysis**, v. 13, n. 2, p. 195–213, 1993.

BACHU, S. CO2 storage in geological media: Role, means, status and barriers to deployment. **Progress in Energy and Combustion Science**, v. 34, n. 2, p. 254–273, 2008.

BAFFES, J.; NAGLE, P. Commodity markets. In: **Commodity Markets Evolution, Challenges, and Policies**. [s.l.] World Bank Group, 2022. p. 1–294.

BARKVED, O. I.; KRISTIANSEN, T.; FJÆR, E. **The 4D seismic response of a compacting reservoir—examples from the Valhall Field, Norway**. SEG Technical Program Expanded Abstracts 2005. **Anais**...Society of Exploration Geophysicists, jan. 2005. Disponível em: <https://library.seg.org/doi/10.1190/1.2148232>

BARTHOLOMEW, G. E. Numerical Integration Over the Triangle. **Mathematical Tables and Other Aids to Computation**, v. 13, n. 68, p. 295, 1959.

BATALHA, N. A. et al. Stability analysis and uncertainty modeling of vertical and inclined wellbore drilling through heterogeneous field. **Oil and Gas Science and Technology**, v. 75, 2020.

BAÙ, D. et al. Ensemble smoothing of land subsidence measurements for reservoir geomechanical characterization. **International Journal for Numerical and Analytical Methods in Geomechanics**, v. 39, n. 2, p. 207–228, 10 fev. 2015.

BAÙ, D. et al. Testing a data assimilation approach to reduce geomechanical uncertainties in modelling land subsidence. **Environmental Geotechnics**, v. 3, n. 6, p. 386–396, 2016.

BECK, A. T. **Confiabilidade e segurança das estruturas**. [s.l.] Elsevier, 2019.

BEER, G. Finite element, boundary element and coupled analysis of unbounded problems in elastostatics. **International Journal for Numerical Methods in Engineering**, v. 19, n. 4, p. 567–580, abr. 1983.

BELAYNEH, M.; GEIGER, S.; MATTHÄI, S. K. Numerical simulation of water injection into layered fractured carbonate reservoir analogs. **American Association of Petroleum Geologists Bulletin**, v. 90, n. 10, p. 1473–1493, 2006.

BENAROYA, H. et al. **Probability Models in Engineering and Science**. [s.l.] CRC Press, 2005.

BESSAR, M. A.; ANCTIL, F.; MATTE, P. Uncertainty propagation within a water level ensemble prediction system. **Journal of Hydrology**, v. 603, n. PD, p. 127193, 2021.

BIOT, M. A. General theory of three-dimensional consolidation. **Journal of Applied Physics**, v. 12, n. 2, p. 155–164, 1941.

BLONDEEL, P. et al. On the Selection of Random Field Evaluation Points in the p-MLQMC Method. In: [s.l: s.n.]. p. 185–203.

BONAZZI, A.; JHA, B.; DE BARROS, F. P. J. Transport analysis in deformable porous media through integral transforms. **International Journal for Numerical and Analytical Methods in Geomechanics**, v. 45, n. 3, p. 307–324, 2021.

BONNET, M. Boundary Integral Equation Methods for Elastic and Plastic Problems. In: **Encyclopedia of Computational Mechanics Second Edition**. Chichester, UK: John Wiley & Sons, Ltd, 2017. p. 1–33.

BOTTAZZI, F.; DELLA ROSSA, E. A Functional Data Analysis Approach to Surrogate Modeling in Reservoir and Geomechanics Uncertainty Quantification. **Mathematical Geosciences**, v. 49, n. 4, p. 517–540, 2017.

BOURNE, S. J. et al. A seismological model for earthquakes induced by fluid extraction from a subsurface reservoir. **Journal of Geophysical Research: Solid Earth**, v. 119, n. 12, p. 8991–9015, 2014.

BOURNE, S. J. et al. A monte carlo method for probabilistic hazard assessment of induced seismicity due to conventional natural gas production. **Bulletin of the Seismological Society of America**, v. 105, n. 3, p. 1721–1738, 2015.

BP. BP Statistical Review of World Energy 2022,(71st edition). **[online] London: BP Statistical Review of World Energy.**, p. 1–60, 2022.

BRZĄKAŁA, W.; PUŁA, W. A probabilistic analysis of foundation settlements. **Computers and Geotechnics**, v. 18, n. 4, p. 291–309, 1996.

BUIJZE, L. et al. Fault reactivation mechanisms and dynamic rupture modelling of depletion-induced seismic events in a Rotliegend gas reservoir. **Geologie en Mijnbouw/Netherlands Journal of Geosciences**, v. 96, n. 5, p. s131–s148, 2017.

BUNGENSTAB, F. C.; BICALHO, K. V. Settlement predictions of footings on sands using probabilistic analysis. **Journal of Rock Mechanics and Geotechnical Engineering**, v. 8, n. 2, p. 198–203, 2016.

CAI, M. Rock mass characterization and rock property variability considerations for tunnel and cavern design. **Rock Mechanics and Rock Engineering**, v. 44, n. 4, p. 379–399, 2011.

CHANG, C.; MAILMAN, E.; ZOBACK, M. Time-dependent subsidence associated with drainage-induced compaction in Gulf of Mexico shales bounding a severely depleted gas reservoir. **AAPG Bulletin**, v. 98, n. 6, p. 1145–1159, 2014.

CHEN, Q.; KONRAD, A. A review of finite element open boundary techniques for static and quasi-static electromagnetic field problems. **IEEE Transactions on Magnetics**, v. 33, n. 1 PART 2, p. 663–676, 1997.

CHENG, H. et al. Comparison of Modeling Soil Parameters Using Random Variables and Random Fields in Reliability Analysis of Tunnel Face. **International Journal of Geomechanics**, v. 19, n. 1, p. 04018184, 2019.

CHO, S. E. Probabilistic analysis of seepage that considers the spatial variability of permeability for an embankment on soil foundation. **Engineering Geology**, v. 133–134, p. 30–39, 2012.

COLAZAS, X. C.; STREHLE, R. W. Chapter 6 Subsidence in the wilmington oil field, long beach, california, USA. **Developments in Petroleum Science**, v. 41, n. C, p. 285–335, 1995.

CRIEL, P. et al. Uncertainty quantification of creep in concrete by Taylor expansion. **Engineering Structures**, v. 153, p. 334–341, 2017.

DASSAULT SYSTEMES. **Software ABAQUS 2017**. , 2017. Disponível em: <http://www.3ds.com/products-services/simulia/products/abaqus/>

DEAN, R. H. et al. A comparison of techniques for coupling porous flow and geomechanics. **SPE Journal**, v. 11, n. 1, p. 132–140, 2006.

DENG, Z. P. et al. Reliability evaluation of slope considering geological uncertainty and inherent variability of soil parameters. **Computers and Geotechnics**, v. 92, p. 121–131, 2017.

DU, J.; OLSON, J. E. A poroelastic reservoir model for predicting subsidence and mapping subsurface pressure fronts. **Journal of Petroleum Science and Engineering**, v. 30, n. 3–4, p. 181–197, 2001.

DUBOIS, D.; PRADE, H. **Possibility theory: An approach to computerized processing of uncertainty**. [s.l.] Springer New York, NY, 1998a.

DUBOIS, D.; PRADE, H. Possibility Theory: Qualitative and Quantitative Aspects. In: **Quantified Representation of Uncertainty and Imprecision**. Dordrecht: Springer Netherlands, 1998b. v. 1p. 169–226.

DUNCAN, J. M. Factors of Safety and Reliability in Geotechnical Engineering. **Journal of Geotechnical and Geoenvironmental Engineering**, v. 126, n. 4, p. 307–316, abr. 2000.

EL-RAMLY, H.; MORGENSTERN, N. R.; CRUDEN, D. M. Probabilistic slope stability analysis for practice. **Canadian Geotechnical Journal**, v. 39, n. 3, p. 665–683, 2002.

FEDON, C. et al. Application of deterministic sampling methods for uncertainty quantification in manufacturing tolerances in neutron physics. **Nuclear Engineering and Design**, v. 373, n. October 2020, p. 111023, 2021.

FENTON, G. A.; GRIFFITHS, D. V. **Risk Assessment in Geotechnical Engineering**. [s.l: s.n.].

FERRONATO, M. et al. Stochastic poromechanical modeling of anthropogenic land subsidence. **International Journal of Solids and Structures**, v. 43, n. 11–12, p. 3324–3336, 2006.

FERRONATO, M. et al. Geomechanical issues of anthropogenic CO2 sequestration in exploited gas fields. **Energy Conversion and Management**, v. 51, n. 10, p. 1918–1928, 2010.

FIGUEROA-MIRANDA, S. et al. Land subsidence by groundwater over-exploitation from aquifers in tectonic valleys of Central Mexico: A review. **Engineering Geology**, v. 246, n. September, p. 91–106, 2018.

FINOL, A. S.; SANCEVIC, Z. A. Chapter 7 Subsidence in venezuela. **Developments in Petroleum Science**, v. 41, n. C, p. 337–372, 1995.

FIORI, A. et al. Stochastic modeling of solute transport in aquifers: From heterogeneity characterization to risk analysis. **Water Resources Research**, v. 51, n. 8, p. 6622–6648, ago. 2015.

FOKKER, P. A.; ORLIC, B. Semi-analytic modelling of subsidence.

Mathematical Geology, v. 38, n. 5, p. 565–589, 2006.

FRANKE, K. W.; OLSON, S. M. Practical Considerations Regarding the Probability of Liquefaction in Engineering Design. **Journal of Geotechnical and Geoenvironmental Engineering**, v. 147, n. 8, ago. 2021.

FRIAS, D. G.; MURAD, M. A.; PEREIRA, F. Stochastic computational modelling of highly heterogeneous poroelastic media with long-range correlations. **International Journal for Numerical and Analytical Methods in Geomechanics**, v. 28, n. 1, p. 1–32, 2004.

GALLOWAY, D. L.; BURBEY, T. J. Review: Regional land subsidence accompanying groundwater extraction. **Hydrogeology Journal**, v. 19, n. 8, p. 1459–1486, 2011.

GAMAGE, K. et al. Permeability-porosity relationships of subduction zone sediments. **Marine Geology**, v. 279, n. 1–4, p. 19–36, 2011.

GAZZOLA, L. et al. Blending measurements and numerical models: a novel methodological approach for land subsidence prediction with uncertainty quantification. **Proceedings of the International Association of Hydrological Sciences**, v. 382, n. i, p. 457–462, 2020.

GEDDES, J. D. Principles of engineering geology. **Endeavour**, v. 1, n. 1, p. 39–40, jan. 1977.

GEERTSMA, J. A remark on the analogy between thermoelasticity and the elasticity of saturated porous media. **Journal of the Mechanics and Physics of Solids**, v. 6, n. 1, p. 13–16, 1957.

GEERTSMA, J. A basic theory of subsidence due to reservoir compaction: the homogeneous case. **Verhandelingen van het nederlandsch geologisch mijnbouw - Kundig genootschap**, v. 28, p. 43–62, 1973a.

GEERTSMA, J. Land Subsidence Above Compacting Oil and Gas Reservoirs. **JPT, Journal of Petroleum Technology**, v. 25, p. 734–744, 1973b.

GEERTSMA, J. A basic theory of subsidence due to reservoir compaction: The homogeneous case. **Verhandelingen van het nederlandsch geologisch mijnbouw - Kundig genootschap**, v. 28, p. 43–62, 1973c.

GEORGESCU, I. **Possibility Theory and the Risk**. Berlin, Heidelberg: Springer Berlin Heidelberg, 2012. v. 274

GOLUB, GENE H AND VAN LOAN, C. F. **Matrix computations**. [s.l.] The Johns Hopkins University Press, 2013.

GRIFFITHS, D. V.; FENTON, G. A. Three-Dimensional Seepage through Spatially Random Soil. **Journal of Geotechnical and Geoenvironmental Engineering**, v. 123, n. 2, p. 153–160, fev. 1997.

HADDAD, M.; EICHHUBL, P. Poroelastic models for fault reactivation in response to concurrent injection and production in stacked reservoirs. **Geomechanics for Energy and the Environment**, v. 24, p. 100181, 2020.

HATCHELL, P.; BOURNE, S. Rocks under strain: Strain-induced time-lapse time shifts are observed for depleting reservoirs. **Leading Edge (Tulsa, OK)**, v. 24, n. 12, p. 1222–1225, 2005.

HATCHELL, P. J. et al. **Monitoring reservoir compaction from subsidence and time-lapse time shifts in the Dan field**. SEG Technical Program Expanded Abstracts 2007. **Anais**...Society of Exploration Geophysicists, jan. 2007. Disponível em: <https://library.seg.org/doi/10.1190/1.2793062>

HERMANSEN, H. et al. Experiences after 10 years of waterflooding the Ekofisk Field, Norway. **Journal of Petroleum Science and Engineering**, v. 26, n. 1–4, p. 11–18, 2000.

HERWANGER, J. V.; HORNE, S. A. Linking reservoir geomechanics and time-lapse seismics: Predicting anisotropic velocity changes and seismic attributes. **Geophysics**, v. 74, n. 4, 2009.

HUDEC, M. R.; JACKSON, M. P. A. Terra infirma: Understanding salt tectonics. **Earth-Science Reviews**, v. 82, n. 1–2, p. 1–28, 2007.

HWANG, H.; LANSEY, K.; JUNG, D. Accuracy of First-Order Second-Moment Approximation for Uncertainty Analysis of Water Distribution Systems. **Journal of Water Resources Planning and Management**, v. 144, n. 2, p. 04017087, 2018.

JACKSON, M. P. A.; HUDEC, M. R. Salt Flow. In: **Salt Tectonics**. Cambridge: Cambridge University Press, 2021. p. 28–60.

JEANNE, P. et al. Effects of in situ stress measurement uncertainties on assessment of predicted seismic activity and risk associated with a hypothetical industrial-scale geologic CO2 sequestration operation. **Journal of Rock Mechanics and Geotechnical Engineering**, v. 8, n. 6, p. 873–885, 2016.

JHA, B. et al. Reservoir characterization in an underground gas storage field using joint inversion of flow and geodetic data. **International Journal for Numerical and Analytical Methods in Geomechanics**, v. 39, n. 14, p. 1619–1638, 10 out. 2015.

JOHNSON, R. B.; DEGRAFF, J. V. **Principles of Engineering Geology**. [s.l.] Michigan University, 1988.

KALAM, S. et al. Carbon dioxide sequestration in underground formations: review of experimental, modeling, and field studies. **Journal of Petroleum Exploration and Production Technology**, v. 11, n. 1, p. 303–325, 2020.

KOHLAS, J.; MONNEY, P. A. Theory of evidence - A survey of its mathematical foundations, applications and computational aspects. **ZOR**

Zeitschrift für Operations Research Mathematical Methods of Operations Research, v. 39, n. 1, p. 35–68, 1994.

Kolmogorov–Smirnov Test. In: **The Concise Encyclopedia of Statistics**. New York, NY, NY: Springer New York, 2008. p. 283–287.

KOMPA, B.; SNOEK, J.; BEAM, A. L. Second opinion needed: communicating uncertainty in medical machine learning. **npj Digital Medicine**, v. 4, n. 1, 2021.

KOSLOFF, D.; SCOTT, R. F.; SCRANTON, J. Finite element simulation of wilmington oil field subsidence: II. Nonlinear modelling. **Tectonophysics**, v. 70, n. 1–2, p. 159–183, 1980.

KRISTIANSEN, T.; PLISCHKE, B. History Matched Full Field Geomechanics Model of the Valhall Field Including Water Weakening and Re-Pressurisation. p. 1–21, 2010.

LEHNER, F. K.; KNOGLINGER, J. K.; D, F. F. Use of a Maysel integral representation for solving poroelastic inclusion problems. **Sixth International Congress on Thermal Stresses, 26-29 May 2005, Vienna, Austria**, p. 77–80, 2005.

LELE, S. P. et al. **Geomechanical Modeling to Evaluate Production-Induced Seismicity at Groningen Field**. Day 2 Tue, November 08, 2016. **Anais**...SPE, 7 nov. 2016. Disponível em: <https://onepetro.org/SPEADIP/proceedings/16ADIP/2-16ADIP/Abu Dhabi, UAE/186176>

LESUEUR, M.; POULET, T.; VEVEAKIS, M. Three-scale multiphysics finite element framework (FE3) modelling fault reactivation. **Computer Methods in Applied Mechanics and Engineering**, v. 365, p. 112988, 2020.

LEUNG, A. Y. T. et al. The fractal finite element method for unbounded problems. **International Journal for Numerical Methods in Engineering**, v. 61, n. 7, p. 990–1008, 2004.

LEWIS, R. W.; MORGAN, K.; WHITE, I. R. The influence of integration rule accuracy on the calculation of surface subsidence by the nucleus of strain method in conjunction with a finite element reservoir simulator. **Applied Mathematical Modelling**, v. 7, n. 6, p. 419–422, 1983.

LI, D. Q. et al. A multiple response-surface method for slope reliability analysis considering spatial variability of soil properties. **Engineering Geology**, v. 187, p. 60–72, 2015.

LI, H.; SARMA, P.; ZHANG, D. A comparative study of the probabilistic-collocation and experimental-design methods for petroleum-reservoir uncertainty quantification. **SPE Journal**, v. 16, n. 2, p. 429–439, 2011.

LIU, J. S. **Monte Carlo Strategies in Scientific Computing**. New York, NY: Springer New York, 2004. v. 26

LLORET-CABOT, M.; FENTON, G. A.; HICKS, M. A. On the estimation of scale of fluctuation in geostatistics. **Georisk**, v. 8, n. 2, p. 129–140, 2014.

LOBRY, J. A fem-green approach for magnetic field problems with open boundaries. **Mathematics**, v. 9, n. 14, 2021.

LOÈVE, M. **Probability Theory I**. New York, NY: Springer New York, 1977. v. 45

LÖFMAN, M. S.; KORKIALA-TANTTU, L. K. Reliability analysis of consolidation settlement in clay subsoil using FOSM and Monte Carlo simulation. **Transportation Geotechnics**, v. 30, n. July, 2021.

LU, M. Rock engineering problems related to underground hydrocarbon storage. **Journal of Rock Mechanics and Geotechnical Engineering**, v. 2, n. 4, p. 289–297, 2010.

MAHDI RAJABI, M. et al. Probabilistic net present value analysis for designing techno-economically optimal sequential CO2 sequestration and geothermal energy extraction. **Journal of Hydrology**, v. 612, n. PB, p. 128237, 2022.

MALLOR, C. et al. Full second-order approach for expected value and variance prediction of probabilistic fatigue crack growth life. **International Journal of Fatigue**, v. 133, n. July 2019, p. 105454, 2020.

MAZRAEHLI, M.; ZARE, S. Probabilistic Estimation of Rock Load Acting on Tunnels Considering Uncertainty in Peak and Post-peak Strength Parameters. **Geotechnical and Geological Engineering**, v. 40, n. 5, p. 2719–2736, 2022.

MEDINA, F.; TAYLOR, R. L. Finite element techniques for problems of unbounded domains. **International Journal for Numerical Methods in Engineering**, v. 19, n. 8, p. 1209–1226, ago. 1983.

MEGLIN, R.; KYTZIA, S.; HABERT, G. Uncertainty, variability, price changes and their implications on a regional building materials industry: The case of Swiss canton Argovia. **Journal of Cleaner Production**, v. 330, p. 129944, 2022.

MEHRABIAN, A.; ABOUSLEIMAN, Y. N. Geertsma's subsidence solution extended to layered stratigraphy. **Journal of Petroleum Science and Engineering**, v. 130, p. 68–76, 2015.

MELAN, E. Der Spannungszustand der durch eine Einzelkraft im Innern beanspruchten Halbscheibe. **ZAMM - Zeitschrift für Angewandte Mathematik und Mechanik**, v. 12, n. 6, p. 343–346, 1932.

MESQUITA, L. C.; SOTELINO, E. D.; PERES, M. L. Uncertainties consideration in elastically heterogeneous fluid-saturated media using first-order second moment stochastic method and Green's function approach. **Applied Mathematical Modelling**, v. 115, p. 819–852, 2023.

MINDLIN, R. D.; CHENG, D. H. Thermoelastic stress in the semi-infinite solid. **Journal of Applied Physics**, v. 21, n. 9, p. 931–933, 1950.

MINKOFF, S. E.; KRIDLER, N. M. A comparison of adaptive time stepping methods for coupled flow and deformation modeling. **Applied Mathematical Modelling**, v. 30, n. 9, p. 993–1009, 2006.

MIRDAR HARIJANI, A.; MANSOUR, S. Municipal solid waste recycling network with sustainability and supply uncertainty considerations. **Sustainable Cities and Society**, v. 81, n. September 2021, p. 103857, 2022.

MISHRA, S. **Alternatives to Monte-Carlo simulation for probabilistic reserves estimation and production forecasting**. Proceedings - SPE Annual Technical Conference and Exhibition. **Anais**...SPE, 27 set. 1998. Disponível em: <https://onepetro.org/SPEATCE/proceedings/98SPE/All-98SPE/New Orleans, Louisiana/190804>

MOHRIAK, W. U.; SZATMARI, P.; ANJOS, S. Salt: Geology and tectonics of selected Brazilian basins in their global context. **Geological Society Special Publication**, v. 363, n. 1, p. 131–158, 2012.

MOLINA-VILLEGAS, J. C.; BALLESTEROS ORTEGA, J. E.; RUIZ CARDONA, D. Formulation of the Green's functions stiffness method for Euler–Bernoulli beams on elastic Winkler foundation with semi-rigid connections. **Engineering Structures**, v. 266, n. March, p. 114616, 2022.

MORGAN, K.; LEWIS, R. W.; WHITE, I. R. The mechanisms of ground surface subsidence above compacting multiphase reservoirs and their analysis by the finite element method. **Applied Mathematical Modelling**, v. 4, n. 3, p. 217–224, 1980.

MOUSAVI, S. E.; SUKUMAR, N. Generalized Duffy transformation for integrating vertex singularities. **Computational Mechanics**, v. 45, n. 2–3, p. 127–140, 2010.

MULLER, A. L. et al. Three-dimensional analysis of boreholes considering spatial variability of properties and poroelastoplasticity. **Journal of Petroleum Science and Engineering**, v. 68, n. 3–4, p. 268–276, 2009a.

MULLER, A. L. et al. Borehole stability analysis considering spatial variability and poroelastoplasticity. **International Journal of Rock Mechanics and Mining Sciences**, v. 46, n. 1, p. 90–96, 2009b.

NAGELHOUT, A. C. G.; ROEST, J. P. A. Investigating fault slip in a model of an underground gas storage facility. **International journal of rock mechanics and mining sciences & geomechanics abstracts**, v. 34, n. 3–4, p. 645, 1997.

NIU, Z.; LI, Q.; WEI, X. Estimation of the surface uplift due to fluid injection into a reservoir with a clayey interbed. **Computers and Geotechnics**, v. 87, p. 198–211, 2017.

ORIKASA, T. et al. Finite element method for unbounded field problems and application to two-dimensional taper. **International Journal for Numerical Methods in Engineering**, v. 19, n. 2, p. 157–168, 1983.

OSTENSEN, R. W. Effect of Stress-Dependent Permeability on Gas Production and Well Testing. **SPE Formation Evaluation**, v. 1, n. 3, p. 227–235, 1986.

OUELLET, A. et al. Reservoir geomechanics for assessing containment in CO2 storage: A case study at Ketzin, Germany. **Energy Procedia**, v. 4, p. 3298–3305, 2011.

PAN, P. et al. Geomechanical modeling of CO2 geological storage: A review. **Journal of Rock Mechanics and Geotechnical Engineering**, v. 8, n. 6, p. 936–947, 2016.

PANDEY, P.; DONGRE, S.; GUPTA, R. Probabilistic and fuzzy approaches for uncertainty consideration in water distribution networks – a review. **Water Science and Technology: Water Supply**, v. 20, n. 1, p. 13–27, 2020.

PANG, R. et al. Seismic time-history response and system reliability analysis of slopes considering uncertainty of multi-parameters and earthquake excitations. **Computers and Geotechnics**, v. 136, n. September 2020, p. 104245, 2021.

PAULLO MUÑOZ, L. F.; ROEHL, D. An analytical solution for displacements due to reservoir compaction under arbitrary pressure changes. **Applied Mathematical Modelling**, v. 52, p. 145–159, 2017.

PEREIRA, F. L. G. et al. Fault reactivation case study for probabilistic assessment of carbon dioxide sequestration. **International Journal of Rock Mechanics and Mining Sciences**, v. 71, p. 310–319, 2014a.

PEREIRA, L. C. et al. Coupled hydro-mechanical fault reactivation analysis incorporating evidence theory for uncertainty quantification. **Computers and Geotechnics**, v. 56, p. 202–215, 2014b.

PEREIRA, L. C. Quantificação de Incertezas Aplicada à Geomecânica de Reservatórios. p. 1–195, 2015.

PEREIRA, L. C.; SÁNCHEZ, M.; GUIMARÃES, L. J. DO N. Uncertainty quantification for reservoir geomechanics. **Geomechanics for Energy and the Environment**, v. 8, p. 76–84, 2016.

PERES, M. L. et al. Stress evolution in elastically heterogeneous and non-linear fluid-saturated media with a Green's function approach. **International Journal for Numerical and Analytical Methods in Geomechanics**, v. 45, n. 10, p. 1323–1346, 2021.

PLÚA, C. et al. Effects of inherent spatial variability of rock properties on the thermo-hydro-mechanical responses of a high-level radioactive waste repository. **International Journal of Rock Mechanics and Mining Sciences**, v. 145, n. February, p. 104682, 2021a.

PLÚA, C. et al. A reliable numerical analysis for large-scale modelling of a high-level radioactive waste repository in the Callovo-Oxfordian claystone. **International Journal of Rock Mechanics and Mining Sciences**, v. 140, n. February, 2021b.

QI, Z. et al. Contact stress reliability analysis based on first order second moment for variable hyperbolic circular arc gear. **Advances in Mechanical Engineering**, v. 14, n. 7, p. 1–13, 2022.

QIUSHI CHEN; KONRAD, A.; BIRINGER, P. P. A finite element-Green's function method for the solution of unbounded three-dimensional eddy current problems. **IEEE Transactions on Magnetics**, v. 30, n. 5, p. 3048–3051, set. 1994.

ROSSI, D.; SCOTTI, A.; VADACCA, L. Quantifying the uncertainties in a fault stability analysis of the Val d'Agri oilfield. **GEM - International Journal on Geomathematics**, v. 11, n. 1, p. 1–20, 2020.

RØSTE, T.; STOVAS, A.; LANDRØ, M. Estimation of layer thickness and velocity changes using 4D prestack seismic data. **Geophysics**, v. 71, n. 6, 2006.

RUTQVIST, J. Status of the TOUGH-FLAC simulator and recent applications related to coupled fluid flow and crustal deformations. **Computers and Geosciences**, v. 37, n. 6, p. 739–750, 2011.

RUTQVIST, J. et al. Fault activation and induced seismicity in geological carbon storage – Lessons learned from recent modeling studies. **Journal of Rock Mechanics and Geotechnical Engineering**, v. 8, n. 6, p. 789–804, 2016.

SEGALL, P. Induced stresses due to fluid extraction from axisymmetric reservoirs. **Pure and Applied Geophysics PAGEOPH**, v. 139, n. 3–4, p. 535–560, 1992.

SEITHEL, R. et al. Probability of fault reactivation in the Bavarian Molasse Basin. **Geothermics**, v. 82, n. May, p. 81–90, 2019.

SETTARI, A.; WALTERS, D. A. Advances in coupled geomechanical and reservoir modeling with applications to reservoir compaction. **SPE Journal**, v. 6, n. 3, p. 334–342, 2001.

SHAFER, G. **A Mathematical Theory of Evidence**. Princeton: Princeton University Press, 1976.

SHAN, J. et al. Intensity-modulated proton therapy (IMPT) interplay effect evaluation of asymmetric breathing with simultaneous uncertainty considerations in patients with non-small cell lung cancer. **Medical Physics**, v. 47, n. 11, p. 5428–5440, 2020.

SHEN, S. L.; XU, Y. S. Numerical evaluation of land subsidence induced by groundwater pumping in Shanghai. **Canadian Geotechnical Journal**, v. 48, n. 9, p. 1378–1392, 2011.

SHEWCHUK, J. R. Triangle: Engineering a 2D quality mesh generator and Delaunay triangulator. In: **Lecture Notes in Computer Science (including subseries Lecture Notes in Artificial Intelligence and Lecture Notes in Bioinformatics)**. [s.l: s.n.]. v. 1148p. 203–222.

SILVESTER, P.; HSIEH, M.-S. Finite-element solution of 2-dimensional exterior-field problems. **Proceedings of the Institution of Electrical Engineers**, v. 118, n. 12, p. 1743, 1971.

SILVESTER, P. P. et al. Exterior Finite Elements for 2-Dimensional Field Problems With Open Boundaries. **Proceedings of the Institution of Electrical Engineers**, v. 124, n. 12, p. 1267–1270, 1977.

SIRIWARDANE, H. J. et al. Geomechanical response of overburden caused by CO2 injection into a depleted oil reservoir. **Journal of Rock Mechanics and Geotechnical Engineering**, v. 8, n. 6, p. 860–872, 2016.

SOHN, M. D.; SMALL, M. J.; PANTAZIDOU, M. Reducing Uncertainty in Site Characterization Using Bayes Monte Carlo Methods. **Journal of Environmental Engineering**, v. 126, n. 10, p. 893–902, out. 2000.

SRIVASTAVA, A.; BABU, G. L. S. Effect of soil variability on the bearing capacity of clay and in slope stability problems. **Engineering Geology**, v. 108, n. 1–2, p. 142–152, 2009.

SUCHOMEL, R.; MAŠÍN, D. Comparison of different probabilistic methods for predicting stability of a slope in spatially variable c-φ soil. **Computers and Geotechnics**, v. 37, n. 1–2, p. 132–140, 2010.

SUN, H. et al. Monitoring land subsidence in the southern part of the lower Liaohe plain, China with a multi-track PS-InSAR technique. **Remote Sensing of Environment**, v. 188, p. 73–84, 2017.

TEATINI, P. et al. Groundwater pumping and land subsidence in the Emilia-Romagna coastland, Italy: Modeling the past occurrence and the future trend. **Water Resources Research**, v. 42, n. 1, p. 1–19, 2006.

TEATINI, P. et al. Geomechanical response to seasonal gas storage in depleted reservoirs: A case study in the Po River basin, Italy. **Journal of Geophysical Research: Earth Surface**, v. 116, n. 2, p. 1–21, 2011.

TEBYANIAN, N. et al. Uncertainty Considerations in Green Infrastructure Optimization: A Review. **Journal of Digital Landscape Architecture**, v. 2022, n. 7, p. 549–560, 2022.

TELLES, J. C. F.; BREBBIA, C. A. Boundary element solution for half-plane problems. **International Journal of Solids and Structures**, v. 17, n. 12, p. 1149–1158, 1981.

TEMPONE, P.; FJÆR, E.; LANDRØ, M. Improved solution of displacements due to a compacting reservoir over a rigid basement. **Applied Mathematical Modelling**, v. 34, n. 11, p. 3352–3362, 2010.

TEMPONE, P.; LANDRØ, M.; FJÆR, E. 4D gravity response of compacting reservoirs: Analytical approach. **Geophysics**, v. 77, n. 3, p. 45–54, 2012.

THOMSON, W. NOTE ON THE INTEGRATION OF THE EQUATIONS OF EQUILIBRIUM OF AN ELASTIC SOLID. In: **Mathematical and Physical Papers**. [s.l: s.n.]. p. 97–99.

UDEGBUNAM, J. E.; AADNØY, B. S.; FJELDE, K. K. Uncertainty evaluation of wellbore stability model predictions. **Journal of Petroleum Science and Engineering**, v. 124, p. 254–263, 2014.

UZIELLI, M.; VANNUCCHI, G.; PHOON, K. K. Random field characterisation of stress-nomalised cone penetration testing parameters. **Géotechnique**, v. 55, n. 1, p. 3–20, fev. 2005.

VAN OPSTAL, G. H. C. The effect of base-rock rigidity on subsidence due to reservoir compaction. **International Journal of Rock Mechanics and Mining Sciences & Geomechanics Abstracts**, v. 12, n. 12, p. 173, dez. 1975.

VAN THIENEN-VISSER, K.; FOKKER, P. A. The future of subsidence modelling: Compaction and subsidence due to gas depletion of the Groningen gas field in the Netherlands. **Geologie en Mijnbouw/Netherlands Journal of Geosciences**, v. 96, n. 5, p. s105–s116, 2017.

VANMARCKE, E. **Random Fields**. [s.l.] WORLD SCIENTIFIC, 2010.

VERDON, J. P. et al. Subsurface fluid injection and induced seismicity in southeast Saskatchewan. **International Journal of Greenhouse Gas Control**, v. 54, p. 429–440, 2016.

VILARRASA, V. et al. Induced seismicity in geologic carbon storage. **Solid Earth**, v. 10, n. 3, p. 871–892, 2019.

VOYIADJIS, G. Z.; ZHOU, Y. Time-dependent modeling of subsidence due to drainage in bounding shales: Application to a depleted gas field in Louisiana. **Journal of Petroleum Science and Engineering**, v. 166, n. January, p. 175–187, 2018.

WANG, B. et al. Reliability analysis of slopes considering spatial variability of soil properties based on efficiently identified representative slip surfaces. **Journal of Rock Mechanics and Geotechnical Engineering**, v. 12, n. 3, p. 642–655, 2020.

WANG, J. P.; YUN, X.; WU, Y. M. A first-order second-moment calculation for seismic hazard assessment with the consideration of uncertain magnitude conversion. **Natural Hazards and Earth System Sciences**, v. 13, n. 10, p. 2649–2657, 2013.

WANG, S. et al. Propagation of uncertainty and sensitivity analysis in an integral oil-gas plume model. **Journal of Geophysical Research: Oceans**, v. 121, n. 5, p. 3488–3501, 27 maio 2016.

WANG, S. et al. Sensitivity analysis and stationary probability distributions of a stochastic two-prey one-predator model. **Applied Mathematics Letters**, v. 116, p. 106996, 2021.

WANGEN, M. Finite element modeling of hydraulic fracturing in 3D. **Computational Geosciences**, v. 17, n. 4, p. 647–659, 2013.

WATANABE, N. et al. Uncertainty analysis of thermo-hydro-mechanical coupled processes in heterogeneous porous media. **Computational Mechanics**, v. 45, n. 4, p. 263–280, 2010.

WENXIN, Z.; ZHENZHOU, L. An inequality unscented transformation for estimating the statistical moments. **Applied Mathematical Modelling**, v. 62, p. 21–37, 2018.

WILLSON, S. M.; FOSSUM, A. F.; FREDRICH, J. T. Assessment of Salt Loading on Well Casings. **Proceedings of the Drilling Conference**, p. 711–720, 2002.

WU, F. et al. A generalized probabilistic edge-based smoothed finite element method for elastostatic analysis of Reissner–Mindlin plates. **Applied Mathematical Modelling**, v. 53, p. 333–352, 2018.

WU, Z. et al. Reliability analysis of slope with cross-correlated spatially variable soil properties using AFOSM. **Environmental Earth Sciences**, v. 80, n. 19, p. 1–12, 2021.

XIONG, Y. et al. Fluid flow with compaction and sand production in unconsolidated sandstone reservoir. **Petroleum**, v. 4, n. 3, p. 358–363, 2018.

YANG, C. et al. Feasibility analysis of using abandoned salt caverns for large-scale underground energy storage in China. **Applied Energy**, v. 137, p. 467–481, 2015.

YANG, Y.; WANG, P.; BRANDENBERG, S. J. An algorithm for generating spatially correlated random fields using Cholesky decomposition and ordinary kriging. **Computers and Geotechnics**, v. 147, n. April, p. 104783, 2022.

YANG, Z.; CHING, J. A novel simplified geotechnical reliability analysis method. **Applied Mathematical Modelling**, v. 74, p. 337–349, 2019.

YANG, Z.; CHING, J. A novel reliability-based design method based on quantile-based first-order second-moment. **Applied Mathematical Modelling**, v. 88, p. 461–473, 2020.

YU, Y. et al. A robust and efficient method of designing piles for landslide stabilization. **Environmental and Engineering Geoscience**, v. 26, n. 4, p. 481–492, 2020.

YUAN, Z. F.; YIN, H. M. Elastic Green's functions for a specific graded material with a quadratic variation of elasticity. **Journal of Applied**

Mechanics, Transactions ASME, v. 78, n. 2, p. 1–6, 2011.

ZARRIN, M.; MOSTAFA GHARABAGHI, A. R.; POURSHA, M. FOSM-based updated consecutive modal pushover procedure (FUCMP) for seismic uncertainty quantification of jacket offshore platforms. **Applied Ocean Research**, v. 128, n. August, p. 103334, 2022.

ZIENKIEWICZ, O. C.; KELLY, D. W.; BETTESS, P. The coupling of the finite element method and boundary solution procedures. **International Journal for Numerical Methods in Engineering**, v. 11, n. 2, p. 355–375, 1977.

ZOCCARATO, C. et al. Modeling fault activation due to fluid production: Bayesian update by seismic data. **Computational Geosciences**, v. 23, n. 4, p. 705–722, 2019.

ZOCCARATO, C. et al. Generalized polynomial chaos expansion for fast and accurate uncertainty quantification in geomechanical modelling. **Algorithms**, v. 13, n. 7, p. 1–23, 2020.

Appendix A
Melan fundamental solution as an auxiliary solution

According to Telles and Brebbia (1981), Melan's solution can be decomposed into the sum of two parts, the first referring to the 2D Kelvin's solution, represented by $(\quad)^k$, and the second formed by complementary terms, represented by $(\quad)^c$.

A.1.
2D Kelvin's fundamental solution

Using the Cartesian coordinate system shown in Figure A.1, the strains at position x_i generated by a horizontal unit point load applied at point X_i are given by:

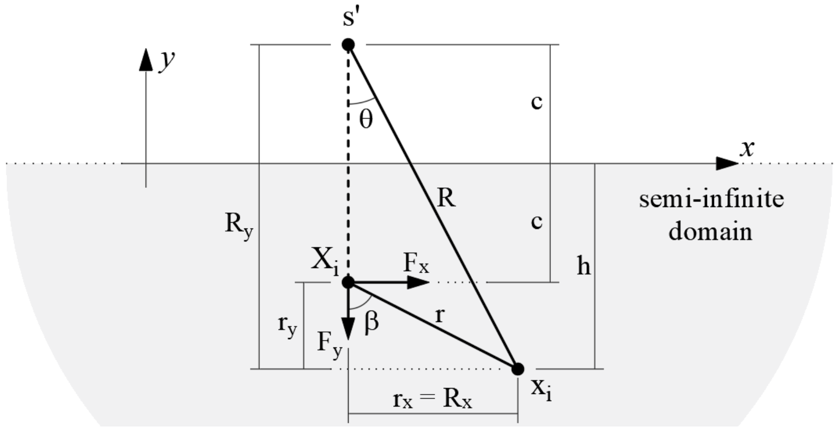

Figure A.1. The coordinate system for Melan's fundamental solution.

$$\varepsilon_{xx}^{(k)} = \frac{A \sin\beta}{r}\{2(1-\sin^2\beta) + (4\nu - 3)\}, \tag{A.1}$$

$$\varepsilon_{yy}^{(k)} = \frac{A \sin\beta}{r}(1 - 2\cos^2\beta), \quad \text{and} \tag{A.2}$$

$$\varepsilon_{xy}^{(k)} = \frac{A \cos\beta}{r}\{2\nu - 1 - 2\sin^2\beta\}. \tag{A.3}$$

Where:

$$A = \frac{1}{8\pi G(1-\nu)} . \tag{A.4}$$

The strains at position x_i generated by a vertical unit point load applied at point X_i are given by:

$$\varepsilon_{xx}^{(k)} = \frac{A\cos\beta}{r}(1 - 2\sin^2\beta)\,, \tag{A.5}$$

$$\varepsilon_{yy}^{(k)} = \frac{A\cos\beta}{r}\{2(1-\cos^2\beta) + (4\nu - 3)\}\,, \qquad \text{and} \tag{A.6}$$

$$\varepsilon_{xy}^{(k)} = \frac{A\sin\beta}{r}\{2\nu - 1 - 2\cos^2\beta\}\,. \tag{A.7}$$

A.2. Complementary part

The complementary strains at position x_i generated by a horizontal unit point load applied at point X_i are given by:

$$\varepsilon_{xx}^{(c)} = A\frac{\sin\theta}{R}\Big\{-8(1-\nu)^2 + (3-4\nu)(3-2\sin^2\theta) - \frac{4ch}{R^2}(3-4\sin^2\theta)\Big\}\,, \tag{A.8}$$

$$\varepsilon_{yy}^{(c)} = A\frac{\sin\theta}{R}\Big\{-4(1-2\nu)(1-\nu) - \frac{4c\cos\theta}{R} + (3-4\nu)\left(1 - \frac{2r_y\cos\theta}{R}\right) - \frac{4ch}{R^2}(1-4\cos^2\theta)\Big\}\,, \tag{A.9}$$

and

$$\varepsilon_{xy}^{(c)} = \frac{A\cos\theta}{2R}\left\{\left(\frac{2c + (3-4\nu)r_y}{R_y}\right)(1-2\sin^2\theta) + \frac{8ch}{R^2}(4\sin^2\theta - 1) - 2(3-4\nu)\sin^2\theta - 1\right\}. \tag{A.10}$$

The strains at position x_i generated by a vertical unit point load applied at point X_i are given by:

$$\varepsilon_{xx}^{(c)} = \frac{A\cos\theta}{R}\left\{-4(1-\nu)(1-2\nu) - \frac{(3-4\nu)r_y}{R_y} + \frac{2(3-4\nu)r_y\cos\theta}{R} + \frac{4ch}{R^2}(4\cos^2\theta - 3)\right\}, \tag{A.11}$$

$$\varepsilon_{yy}^{(c)} = \frac{A\cos\theta}{R}\left\{[3(3-4\nu) - 8(1-\nu)^2] - \frac{2c}{R_y} + \frac{4c}{R}\left(\cos\theta + \frac{3h}{R}\right) - \left[2(3-4\nu) + \frac{16ch}{R^2}\right]\cos^2\theta\right\}, \qquad \text{and} \tag{A.12}$$

$$\varepsilon_{xy}^{(c)} = \frac{A\sin(\theta)}{2R}\left\{2(1+2\nu) + \frac{\cos(\theta)}{R}\Big(4c - 2r_y(3-4\nu)\Big) \right.$$
$$\left. + \frac{8ch}{R^2}\left(1 - 4\ \cos^2(\theta)\right)\ - 2(3-4\nu)\cos^2(\theta)\right\}. \tag{A.13}$$

Appendix B
Numerical strategies for the treatment of singular points

To solve the auxiliary problem, when it is singular, the use of the Bartholomew quadrature (BARTHOLOMEW, 1959) with the Duffy transformation (BONNET, 2017; MOUSAVI; SUKUMAR, 2010) is proposed.

B.1.
Bartholomew quadrature

The numerical integration using the Bartholomew quadrature (BARTHOLOMEW, 1959) is performed using the mapping from the physical domain (Ω_t) to the computational domain (Ω_ξ) shown in Figure B.1.

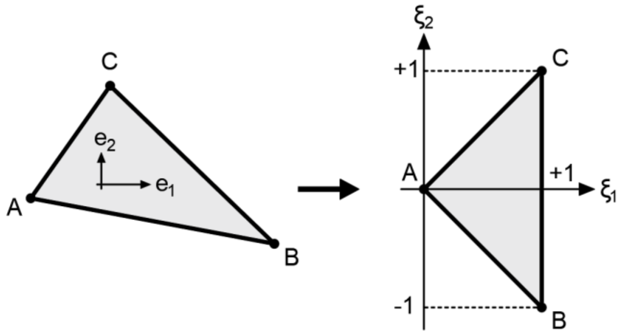

Figure B.1. Mapping from the physical domain (Ω_t) to the computational domain (Ω_ξ).

This mapping is mathematically expressed by

$$x_i = F_{ij}\xi_j + x_i^{(A)}\,, \tag{B.1}$$

with

$$\begin{aligned} F_{ij} &= \frac{1}{2}\left(x_i^{(C)} + x_i^{(B)} - 2x_i^{(A)}\right)e_j \quad \text{if} \quad i = j \ \text{ or} \\ F_{ij} &= \frac{1}{2}\left(x_i^{(C)} - x_i^{(B)}\right)e_j \quad \text{if} \quad i \neq j\,, \end{aligned} \tag{B.2}$$

where e_j and ξ_j are the orthonormal bases of the physical (Ω_t) and computational (Ω_ξ) domains, respectively.

Bartholomew quadrature can be used considering different levels of integration, as shown in Figure B.2. Level n corresponds to 2^{n-1} divisions on each side of the triangular reference element (domain Ω_ξ in Figure B.1), which results in

4^{n-1} sub-triangles of the same area. The integration points are in the middle positions of the sides of the sub-triangles and have weights equal to $1/3 \cdot 1/4^{n-1}$, when the integration point is on the boundary of the reference triangle, or $2/3 \cdot 1/4^{n-1}$, when the integration point is inside the triangular reference element.

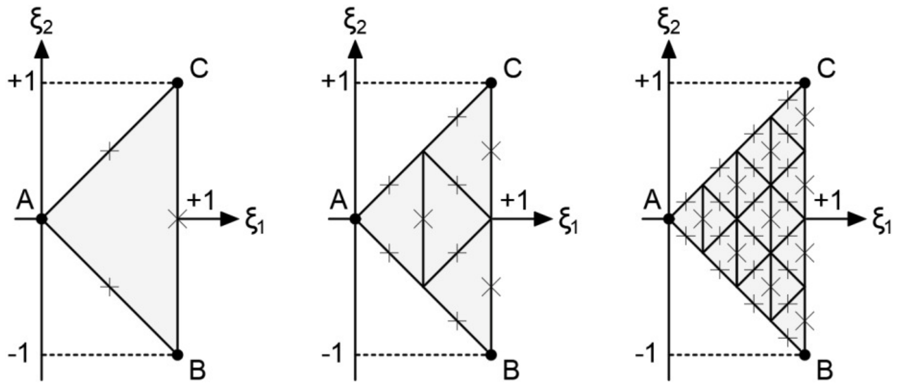

Figure B.2. Position of integration points in the computational domain for three levels of integration.

B.2.
Duffy's transformation

Duffy's transformation maps the triangular element to a quadrilateral element in which the function to be calculated is not singular (BONNET, 2017; MOUSAVI; SUKUMAR, 2010). For this mapping, consider the unit point load applied at node A and the first sub-triangle defined by Bartholomew quadrature with level n, as shown in Figure B.3. Applying Duffy's transformation, this sub-triangle is transformed into a quadrilateral element (with sides equal to two) using the following equations

$$2^n \xi_1 - 1 = \eta_1 , \qquad \text{and} \qquad \xi_2 = \xi_1 \, \eta_2 , \tag{B.3}$$

where the Jacobian of the transformation is $\xi_1/2^n$.

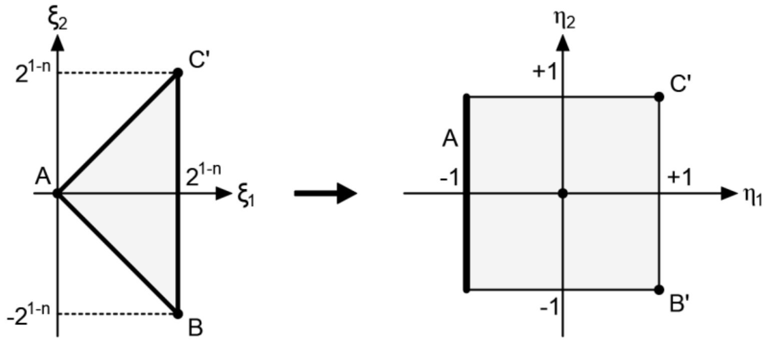

Figure B.3. Duffy's transformation applied to the first sub-triangle of the Bartholomew quadrature with integration level n.

As discussed in Appendix A, the Melan solution can be decomposed into two parts, the first referring to the 2D Kevin's solution and the second formed by complementary terms. The first part will be singular when the distance r tends to zero, which can occur in any position of the semi-infinite domain Ω_t. The second part will be singular when R tends to zero, which will only occur when the unit point load and the evaluated point are on the surface of the semi-infinite domain. Regardless of the situation, singularities can be treated in isolation using Duffy's transformation. In this way, the integral of the strains found from the auxiliary problem in the physical domain (Ω_t) can be written as

$$\int_{\Omega_t} \frac{f(\alpha)}{d_t}\, dV_t\,, \tag{B.4}$$

this integral is transformed into the computational domain (Ω_ξ)

$$\int_{\Omega_\xi} \frac{f(\alpha)}{d_\xi}\, J_1 dV_\xi \tag{B.5}$$

using the mapping Eq. (B.1) and the Jacobian J_1. Eq. (B.5) becomes singular When the unit point load is applied to one of the nodes of the triangular elements (Figure B.1). Assuming that this force is applied at node A, the first sub-triangle of the Bartholomew quadrature (Figure B.3) can be transformed into a quadrilateral element through Eq.(B.3). Thus, Eq. (B.5) is rewritten as

$$\int_{\Omega_\eta} \frac{f(\alpha)}{C_{\xi\xi}^{1/2}(1+\eta_2^2)^{1/2}} \frac{J_1}{2^n}\, dV_\eta\,, \tag{B.6}$$

eliminating the singularity problem in the integrand, where $C_{\xi\xi} = F_{ij}F_{ji}$. In this work, the integral Eq. (B.6) is calculated using the Gaussian quadrature.

Appendix C
Frequency histograms and probability density function for other reference points

This appendix presents the frequency histograms and p.d.f. of the random variables that represent the horizontal and vertical displacements of the reference points shown in Figure 4.3 and Figure 4.10.a.

C.1.
Random variables representing the horizontal and vertical displacements of the problem with uniform depletion (Section 4.4.1)

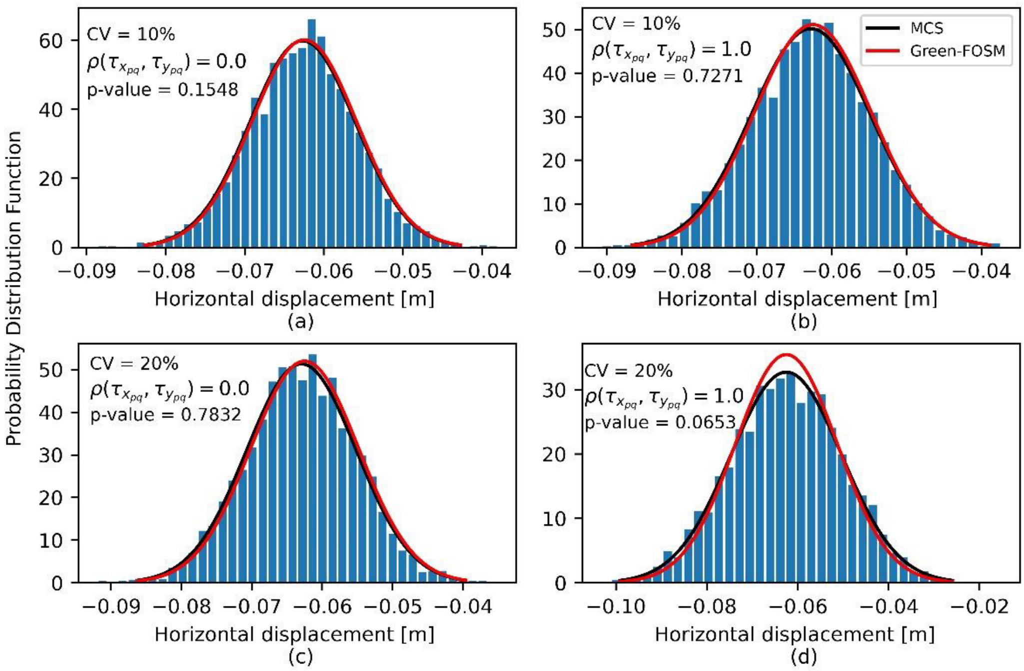

Figure C.1. Frequency histograms and probability density function of the random variable representing the horizontal (a-d) and vertical displacement (e-h) of the reference point 1 (RF1) showed Figure 4.3.

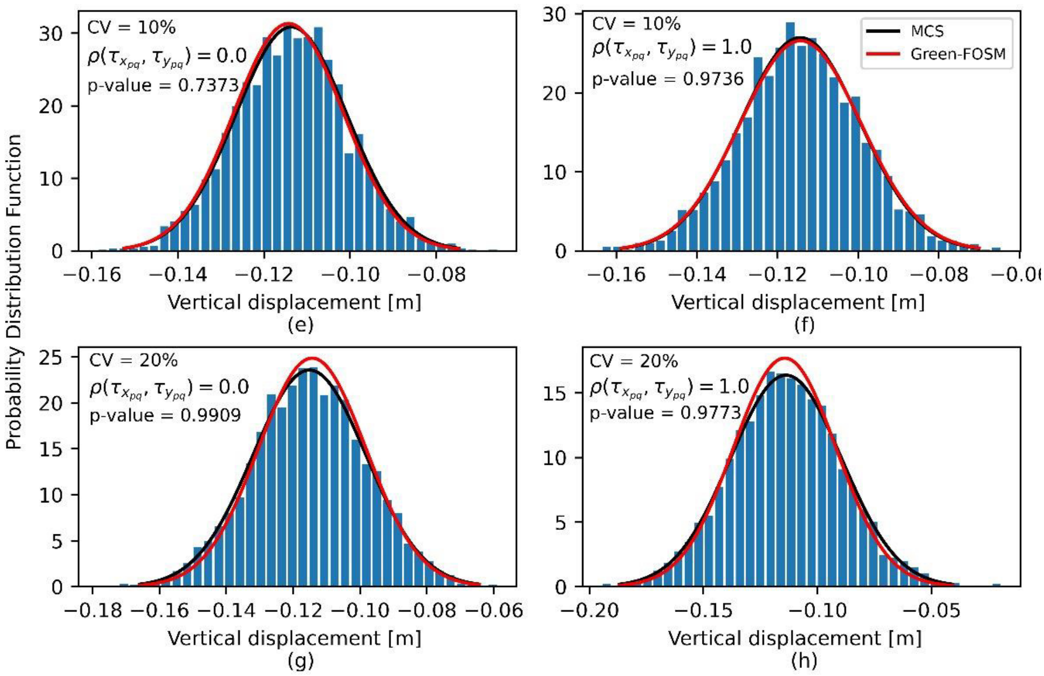

Figure C.1. Frequency histograms and probability density function of the random variable representing the horizontal (a-d) and vertical displacement (e-h) of the reference point 1 (RF1) showed Figure 4.3 (continuation).

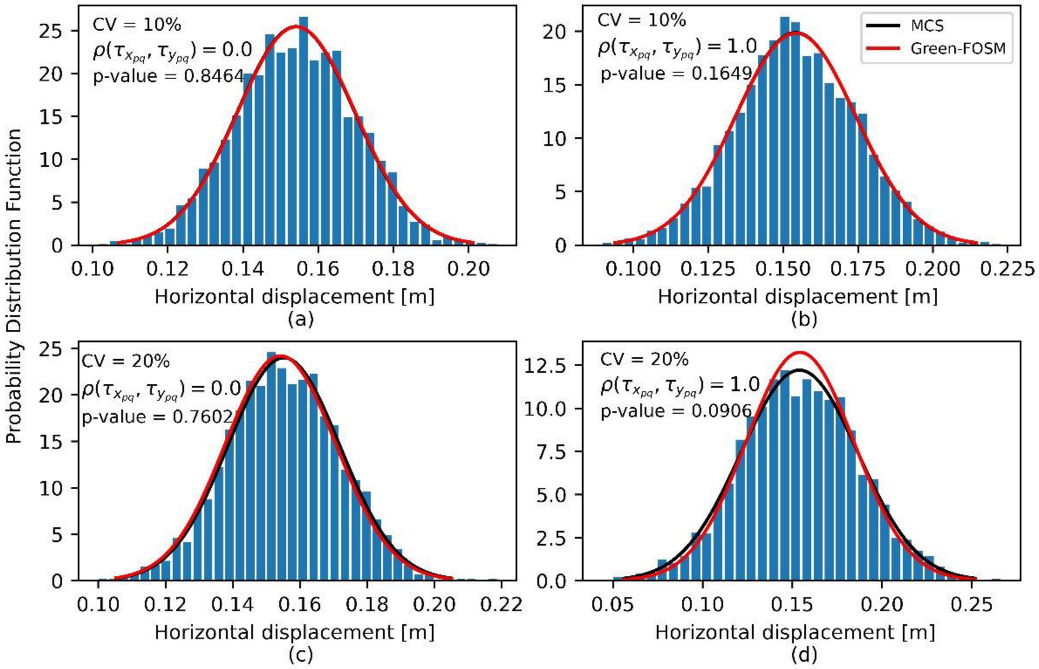

Figure C.2. Frequency histograms and probability density function of the random variable representing the horizontal (a-d) and vertical displacement (e-h) of the reference point 2 (RF2) showed Figure 4.3.

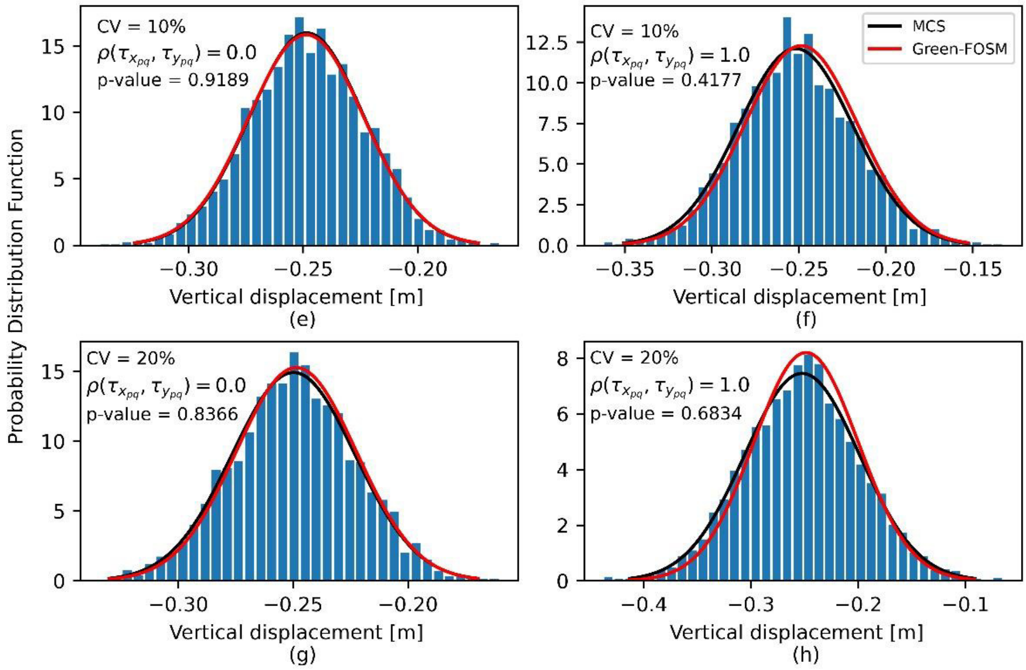

Figure C.2. Frequency histograms and probability density function of the random variable representing the horizontal (a-d) and vertical displacement (e-h) of the reference point 2 (RF2) showed Figure 4.3 (continuation).

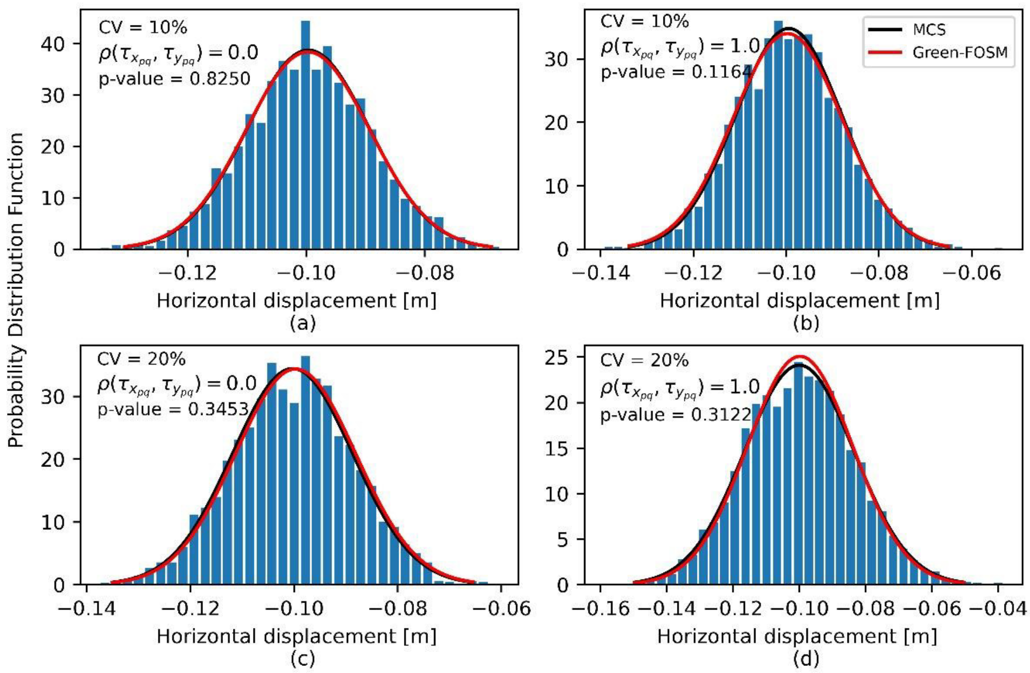

Figure C.3. Frequency histograms and probability density function of the random variable representing the horizontal (a-d) and vertical displacement (e-h) of the reference point 3 (RF3) showed Figure 4.3.

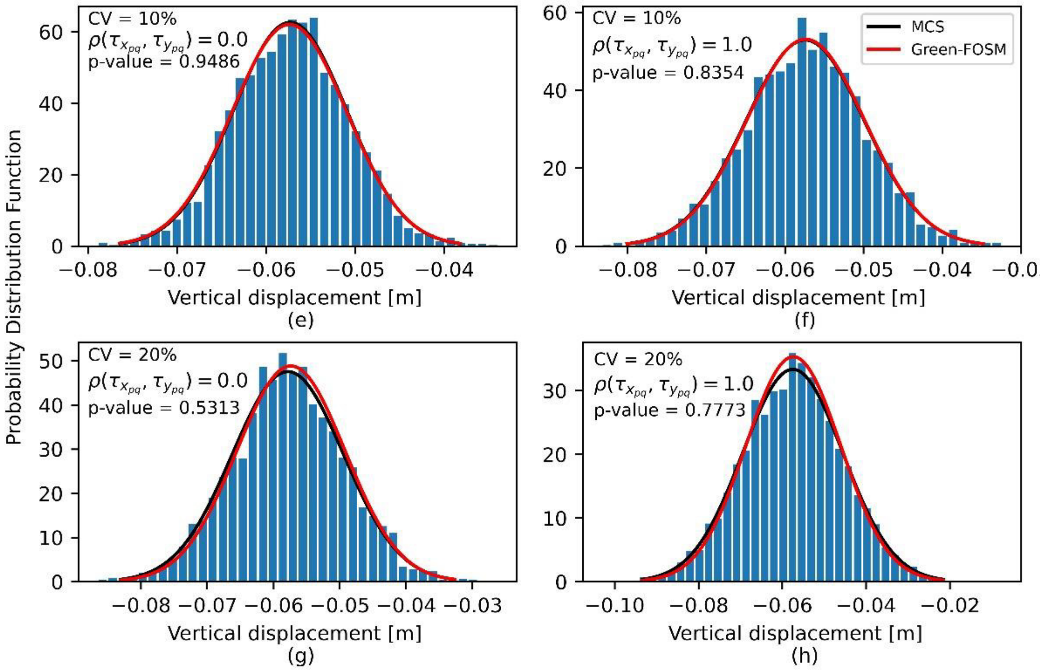

Figure C.3. Frequency histograms and probability density function of the random variable representing the horizontal (a-d) and vertical displacement (e-h) of the reference point 3 (RF3) showed Figure 4.3 (continuation).

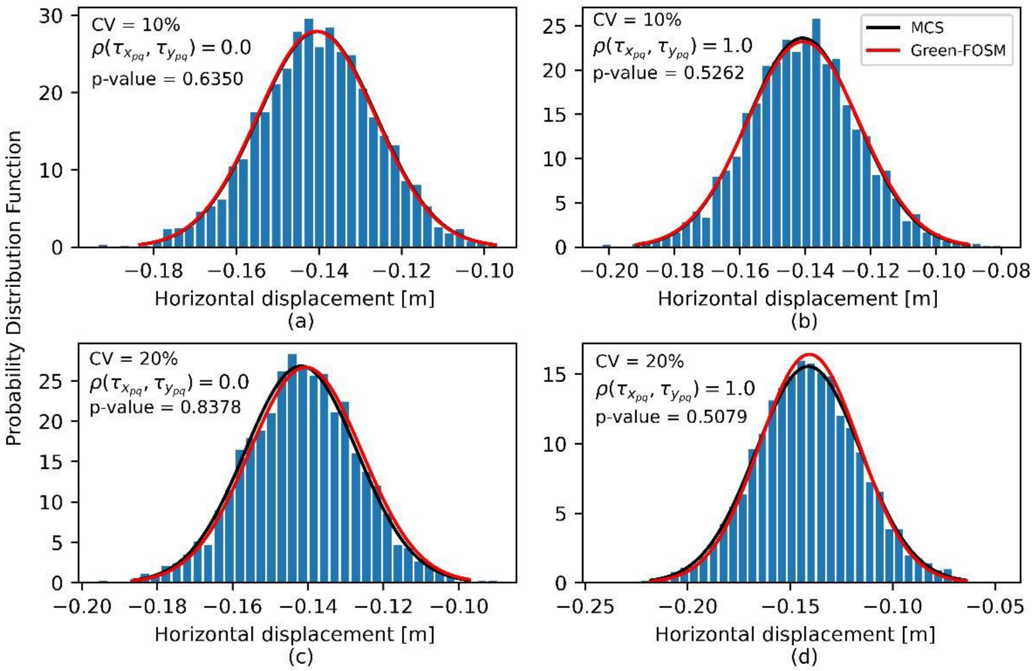

Figure C.4. Frequency histograms and probability density function of the random variable representing the horizontal (a-d) and vertical displacement (e-h) of the reference point 4 (RF4) showed Figure 4.3.

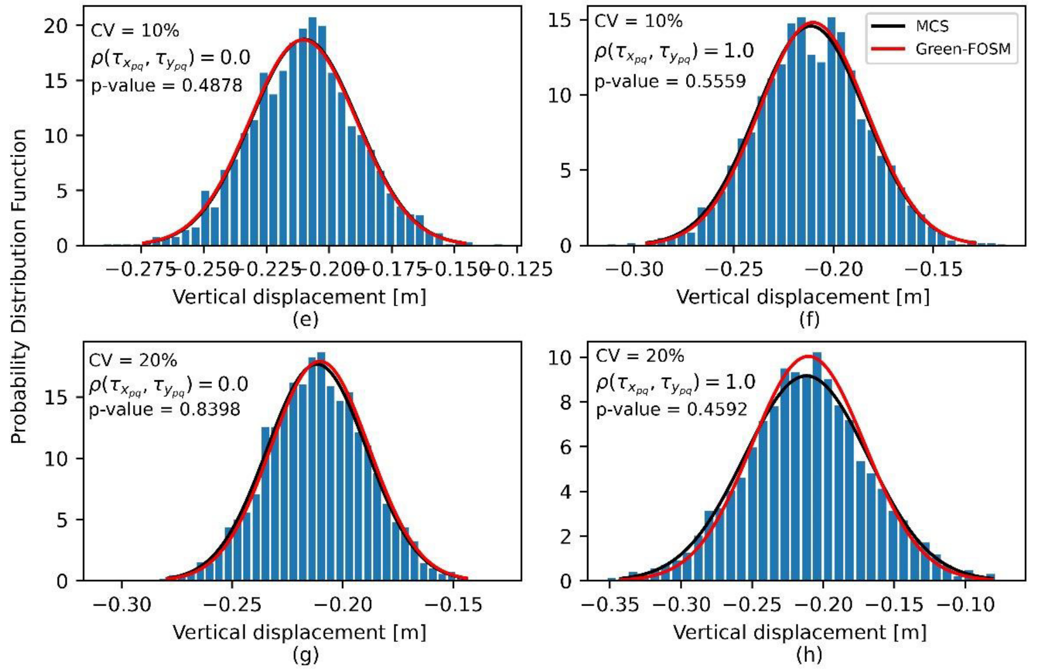

Figure C.4. Frequency histograms and probability density function of the random variable representing the horizontal (a-d) and vertical displacement (e-h) of the reference point 4 (RF4) showed Figure 4.3 (continuation).

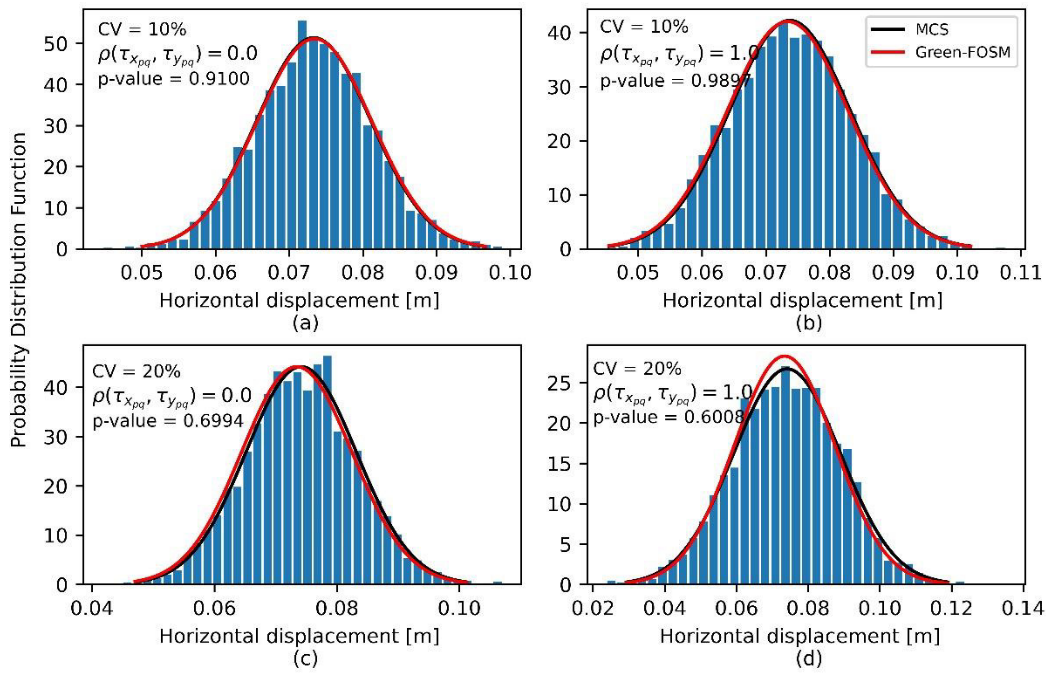

Figure C.5. Frequency histograms and probability density function of the random variable representing the horizontal (a-d) and vertical displacement (e-h) of the reference point 5 (RF5) showed Figure 4.3.

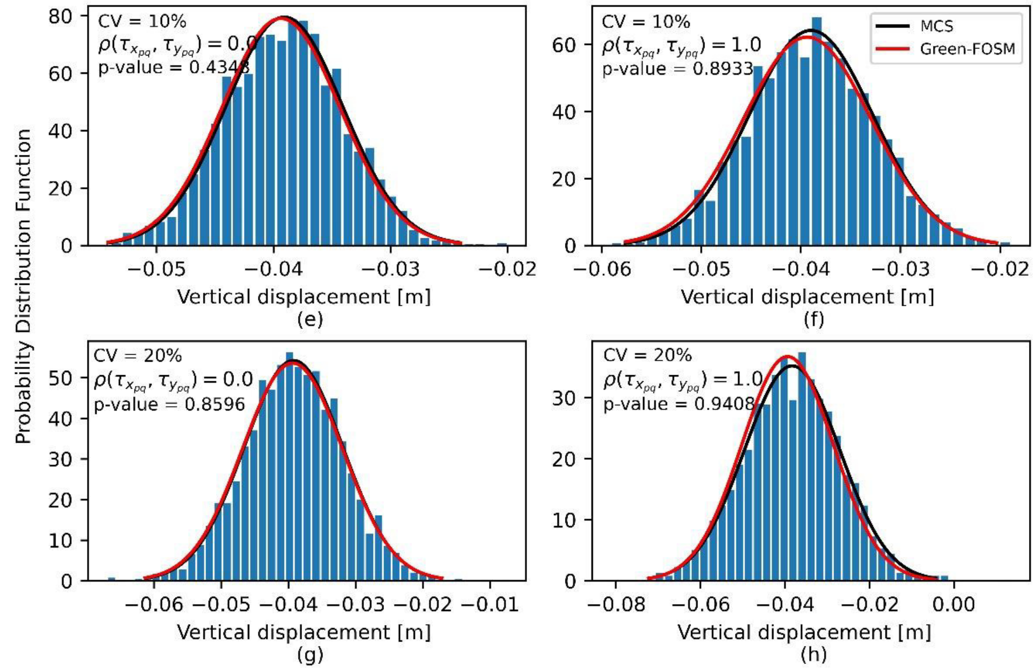

Figure C.5. Frequency histograms and probability density function of the random variable representing the horizontal (a-d) and vertical displacement (e-h) of the reference point 5 (RF5) showed Figure 4.3 (continuation).

C.2. Random variables representing the horizontal and vertical displacements of the problem with non-uniform depletion (Section 4.4.2)

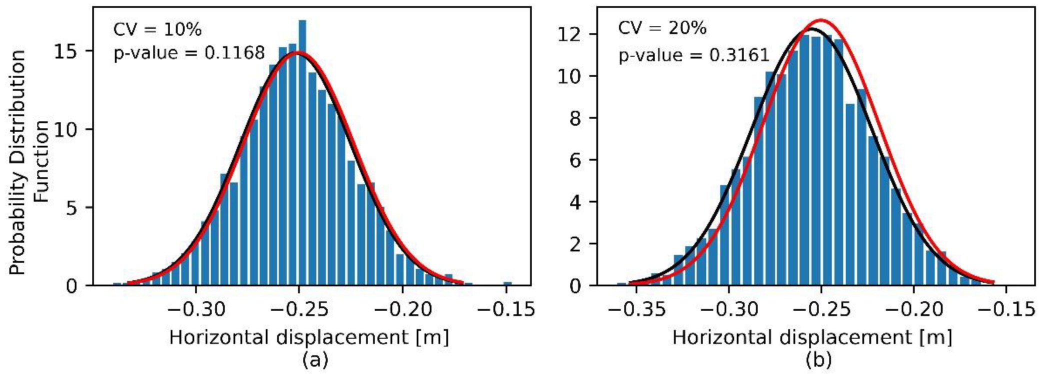

Figure C.6. Frequency histograms and probability density function of the random variable representing the horizontal (a-b) and vertical displacement (c-d) of the reference point 1 (RF1) showed Figure 4.10.

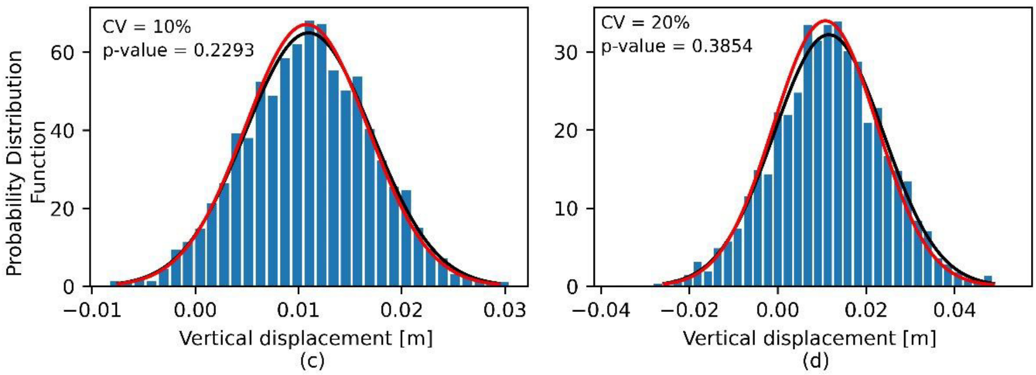

Figure C.6. Frequency histograms and probability density function of the random variable representing the horizontal (a-b) and vertical displacement (c-d) of the reference point 1 (RF1) showed Figure 4.10 (continuation).

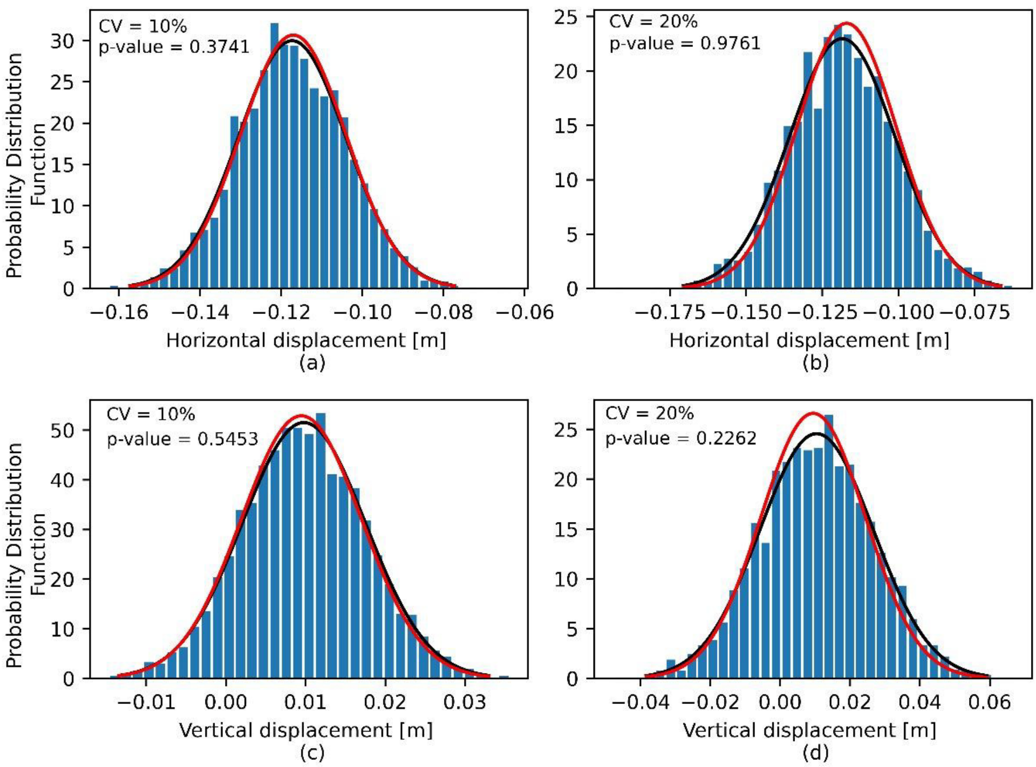

Figure C.7. Frequency histograms and probability density function of the random variable representing the horizontal (a-b) and vertical displacement (c-d) of the reference point 2 (RF2) showed Figure 4.10.

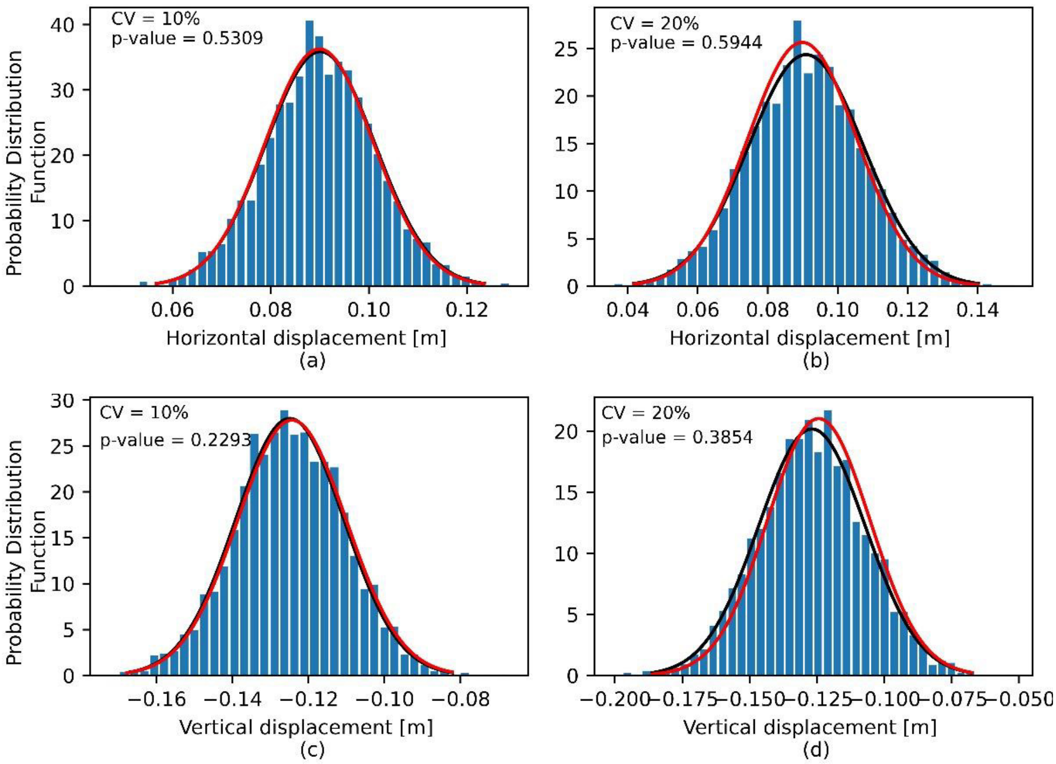

Figure C.8. Frequency histograms and probability density function of the random variable representing the horizontal (a-b) and vertical displacement (c-d) of the reference point 3 (RF3) showed Figure 4.10.

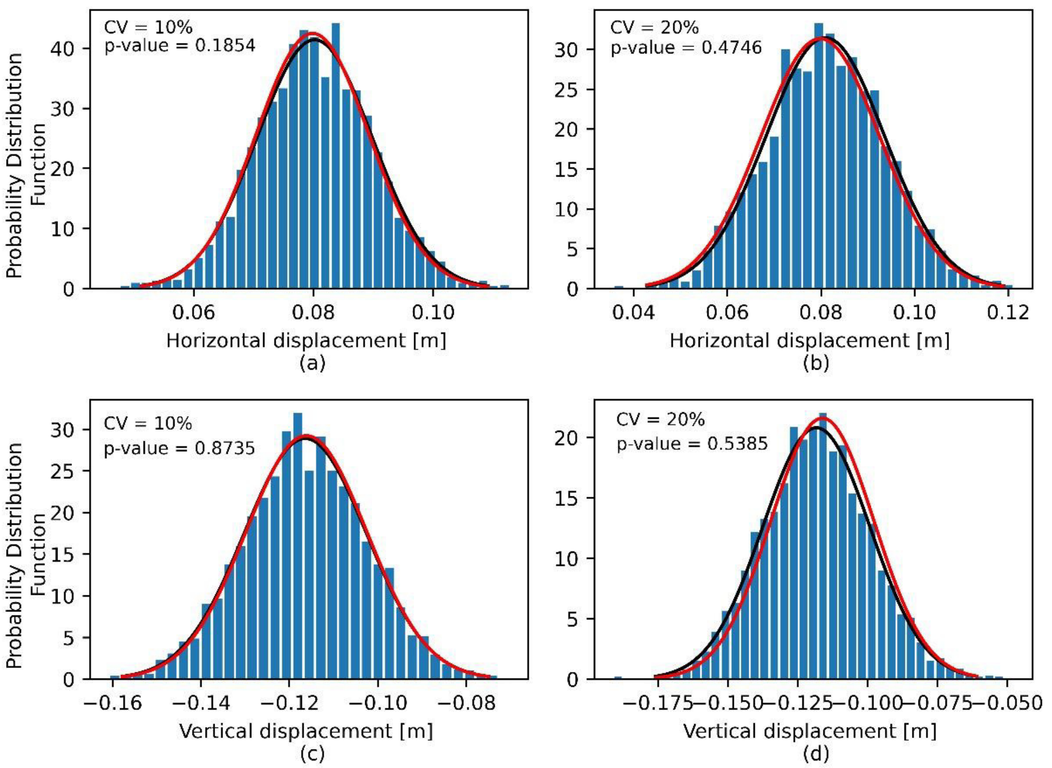

Figure C.9. Frequency histograms and probability density function of the random variable representing the horizontal (a-b) and vertical displacement (c-d) of the reference point 4 (RF4) showed Figure 4.10.

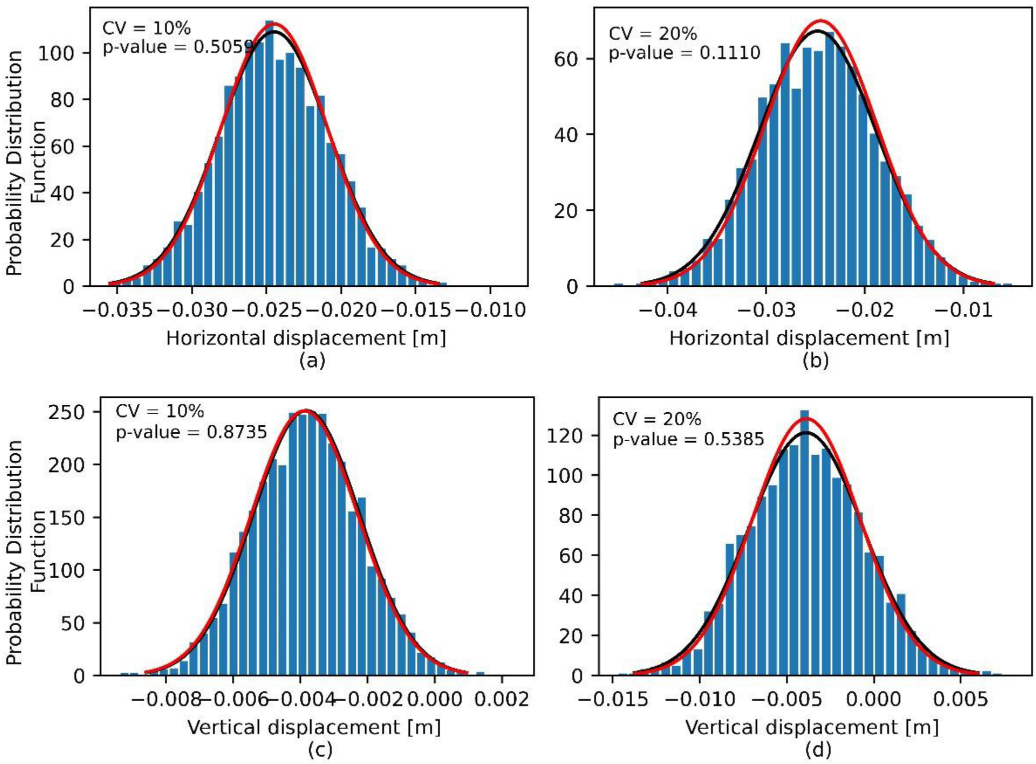

Figure C.10. Frequency histograms and probability density function of the random variable representing the horizontal (a-b) and vertical displacement (c-d) of the reference point 5 (RF5) showed Figure 4.10.